

Dissertation zur Erlangung des Doktorgrades der  
Fakultät für Chemie und Pharmazie der Ludwig-  
Maximilians-Universität München

***In situ* study of ribosome biogenesis, non-stop  
mRNA decay, and liquid-liquid phase  
separation by cryo-electron tomography**

**Zhen Hou**

**Bijie, Guizhou, China**

**2022**



## **Erklärung**

Diese Dissertation wurde im Sinne von § 7 der Promotionsordnung vom 28. November 2011 von Hon.-Prof. Dr. Elena Conti betreut.

## **Eidesstattliche Versicherung**

Diese Dissertation wurde eigenständig und ohne unerlaubte Hilfe erarbeitet.

München, 24.05.2022

---

Zhen Hou

Dissertation eingereicht am 25.05.2022

1. Gutachterin: Hon.-Prof. Dr. Elena Conti
2. Gutachter: Prof. Dr. Karl-Peter Hopfner

Mündliche Prüfung am 04.07.2022



# Acknowledgment

I want to express my gratitude to those who helped me during my Ph.D. study. First of all, my deepest appreciation goes foremost to Dr. Philipp Erdmann, my mentor, for his constant encouragement and guidance. He taught me all the techniques applied in the projects and instructed me with the background knowledge, without which, this dissertation could not have been completed in its current form.

Second, I would like to express my sincere gratitude to Prof. Dr. Elena Conti and Prof. Dr. Jürgen Plitzko, my supervisors, for leading me into the world of structural biology and cryo-ET. They've been very supportive during my Ph.D. and provided valuable advice to my projects and thesis writing.

Third, I owe a particular debt of gratitude to Prof. Dr. Baumeister Wolfgang for allowing me to perform experiments using the state-of-the-art instruments in his department and also for his suggestions for my projects. In addition, I also want to thank my TAC member Prof. Dr. Franz-Ulrich Hartl and Prof. Dr. Heinrich Leonhardt for their instructions in my TAC meetings.

Moreover, I would like to say “thank you” to my lab mates and collaborators Achim Keidel, Dr. Nicole Eisele, Chuan Liu, Jonathan Schneider, Sagar Khavnekar, Prof. Dr. Christian Griesinger, Dr. Michael Engelke, Joachim Maier and those who are not mentioned here for the wonderful collaborations and their kind help in experiments.

At last but not least, my thanks would go to my mom, my dad, and my beloved one Qin for their confidence in me and loving consideration through the past years.

Thank you!

Danke!

谢谢!

---

# Content Table

<b>1. Methodological Background</b> .....	1
1.1 Cryo-electron Microscopy.....	1
1.2 Cryo-electron Tomography .....	2
1.3 Sample Preparation and Focused Ion Beam Milling.....	5
1.4 Tomogram Reconstruction.....	9
1.5 Template Matching .....	10
1.6 Subtomogram Averaging .....	11
<b>2. Ribosome Biogenesis Project</b> .....	14
2.1 Introduction and Aims.....	14
2.1.1 Liquid-liquid Phase Separation .....	14
2.1.2 Ribosome Biogenesis .....	16
2.1.3 The Nucleolar Organization .....	21
2.1.4 Aims of the Ribosome Biogenesis Project.....	25
2.2 Results .....	25
2.2.1 Lamellae Containing Nuclei.....	25
2.2.2 Preribosome-like Particles in <i>S. cerevisiae</i> .....	27
2.2.3 Initial Subtomogram Averaging of Preribosome-like Particles in <i>S. cerevisiae</i> .....	29
2.2.4 Further Subtomogram Averaging of Preribosome-like Particles in <i>S. cerevisiae</i> .....	29
2.2.5 The Typical Tripartite Nucleolar Organization in <i>C. reinhardtii</i> .....	33
2.2.6 Subtomogram Averaging of Preribosome-like Particles in <i>C. reinhardtii</i> .....	35
2.2.7 Classification of SSU Processome and LSU Precursors in <i>C. reinhardtii</i> .....	37
2.2.8 Maturation of SSU Processome and LSU Precursor in <i>C. reinhardtii</i> .....	41
2.3 Discussion .....	46
<b>3. Non-stop mRNA Decay Project</b> .....	50
3.1 Introduction and Aims.....	50
3.1.1 mRNA Surveillance .....	50
3.1.2 Nonstop mRNA Decay in <i>S. cerevisiae</i> .....	51
3.1.3 The Exosome Complex and Ski7 of <i>S. cerevisiae</i> .....	54
3.1.4 The Ski2-Ski3-Ski8 Complex of <i>S. cerevisiae</i> .....	58
3.1.5 Aims of the NSD Project.....	61
3.2 Results .....	61

---

3.2.1 Impairment of NSD .....	61
3.2.2 Tomograms of NSD-defective Yeast Cells.....	64
3.2.3 Subtomogram Averaging of Ribosomes in NSD-defective Yeasts .....	67
3.2.4 Assessment of NSD Induction for Correlative FIB Milling .....	69
3.2.5 Granule Aggregates in NSD-defective Yeast Cells .....	73
3.2.6 Subtomogram Averaging of Ribosomes in Granule-aggregates-containing Yeast Cells.....	75
3.2.7 Subcellular Localization of Ski7 with GEMs and GPA1N9.....	77
3.3 Discussion .....	82
<b>4. SLP65-CIN85 LLPS Project .....</b>	<b>86</b>
4.1 Introduction and Aims.....	86
4.1.1 The B Lymphocyte and BCR Activation .....	86
4.1.2 SLP65 and CIN85 .....	88
4.1.3 Aims of the SLP65-CIN85 LLPS Project .....	92
4.2 Results .....	93
4.2.1 <i>In Vitro</i> Analysis of SLP65-CIN85 LLPS.....	93
4.2.2 Correlative FIB Milling of SLP65-CIN85 LLPS .....	95
4.2.3 <i>In Situ</i> Visualization of SLP65-CIN85 LLPS .....	100
4.2.4 Characterization of LLPS-related Vesicles .....	102
4.3 Discussion .....	104
<b>5. Methods and Materials .....</b>	<b>107</b>
5.1 Yeast Culture and Strains .....	107
5.2 DT40 B Lymphocytes Cell Culture .....	109
5.3 Chlamydomonas Culture and Strains.....	109
5.4 Western Blot.....	110
5.5 Pull-down Assay .....	111
5.6 Plunge Freezing.....	112
5.7 FLM.....	113
5.8 Cryo-CLEM and 3D Correlation.....	113
5.9 FIB Milling (Standard and Correlative).....	113
5.10 Cryo-EM and Cryo-ET.....	114
5.11 Tomogram Reconstruction.....	115
5.12 Template Matching .....	115
5.13 STA .....	116

---

5.14 Sphere Fitting .....	117
5.15 Density Measurements .....	118
5.16 Classification Reproducibility .....	118
5.17 Data Visualization .....	119
5.18 Software .....	120
<b>6. Appendix</b> .....	<b>121</b>
6.1 Abbreviations .....	121
6.2 References .....	123

---

## List of Figures

Figure 1. Overview of a cryo-electron microscope and the schematic of cryo-ET image collection .....	5
Figure 2. Schematic illustration of a FIB machine setup and stepwise FIB milling procedures. ....	8
Figure 3. Schematic illustration of data processing.....	12
Figure 4. Simplified illustration of the formation of LLPS.. ....	16
Figure 5. Schematic show of ribosome biogenesis.....	19
Figure 6. Schematic illustration of of the transition from pre-90S to pre-40S .....	20
Figure 7. Schematic illustration of the maturation of pre-60S.....	20
Figure 8. Nucleolar organization of eukaryotes.....	24
Figure 9. Overview of yeast lamellae. ....	26
Figure 10. Reconstructed tomograms of yeast nuclei.....	28
Figure 11. The initial STA of 90S preribosomes.....	31
Figure 12. Further STA of preribosome-like particles.....	32
Figure 13. The illustration of nuclei and tripartite nucleolar organization in <i>C. reinhardtii</i> . ....	34
Figure 14. Characterization of SSU processome and LSU precursor.....	36
Figure 15. Image-based analysis of nuclear particles .....	38
Figure 16. Further classification of SSU processome and LSU precursor. ....	39
Figure 17. Cross-effect analysis of SSU processome classes and LSU precursor classes .....	40
Figure 18. Analysis on the distance of SSU processome classes and LSU precursor classes to the nucleolar center.....	43
Figure 19. Assessment on the abundance of SSU processome classes and LSU precursor classes in different conditions.....	44
Figure 20. Structural alignment of <i>in situ</i> SSU processome and LSU precursor structures with published PDB molecular models and EM density maps. ....	45

---

Figure 21. Summary of the <i>in situ</i> study of ribosome biogenesis in <i>C. reinhardtii</i> .....	49
Figure 22. Schematic overview of nonstop mRNA decay in yeasts.....	54
Figure 23. Overview of yeast exosome complex and Ski7.....	57
Figure 24. Structural overview of the yeast Ski complex and project hypotheses.. .....	60
Figure 25. Schematic illustration of NSD-induction by galactose in yeasts.....	62
Figure 26. Assessment of impairment of NSD. ....	63
Figure 27. Lamellae of yeasts. ....	65
Figure 28. Reconstructed tomograms of wild type and NSD-defective yeasts.. ..	66
Figure 29. Subtomogram averaging of ribosomes in NSD-defective yeasts. ....	68
Figure 30. Time-course FLM of wild type and Ski7 <sup>ExoMut</sup> - yeasts detecting mApple-PGK1-nonstop under galactose induction. ....	71
Figure 31. Time-course FLM of wild type and Ski7 <sup>ExoMut</sup> - yeasts detecting Ski3- eGFP under galactose induction. ....	72
Figure 32. Correlative FIB milling and tomograms of Ski7 <sup>ExoMut</sup> - yeasts under 6-hour galactose induction. ....	74
Figure 33. Subtomogram averaging of ribosomes in granule-aggregates- containing Ski7 <sup>ExoMut</sup> - yeasts.. ....	76
Figure 34. Schematic illustration of generating yeast strains for subcellular localization.....	79
Figure 35. Verification of GEM40 and GEM40/20-Ski7 constructs.....	80
Figure 36. FLM of GEM40 and GEM40/20-Ski7 strains.....	81
Figure 37. Verification of GPA1N9 and GPA1N9-Rpn5 constructs.....	82
Figure 38. The structural comparison between the published eEF3-80S ribosome structure and the ribosome structure containing an eEF3-likedensity. ....	85
Figure 39. Schematic illustration of BCR-mediated activation of B lymphocytes.. .....	88
Figure 40. Overview of SLP65 and CIN85.. ....	92
Figure 41. <i>In vitro</i> analysis of SLP65-CIN85 LLPS.....	94

---

Figure 42. Cryo-ET analysis of <i>in vitro</i> prepared SLP65-CIN85 LLPS.....	95
Figure 43. FLM of SLP65-CIN85 LLPS in DT40 cells .....	97
Figure 44. Cryo-CLEM of SLP65-CIN85 LLPS.....	98
Figure 45. Images for correlative FIB milling and TEM overview of SLP65- CIN85 LLPS.. .....	99
Figure 46. Reconstructed and segmented tomograms of SLP65-CIN85 LLPS..	101
Figure 47. Characterization of LLPS-related vesicles and vesicle-associated densities.....	103
Figure 48. SLP65-CIN85 LLPS models. ....	106

---

## Summary

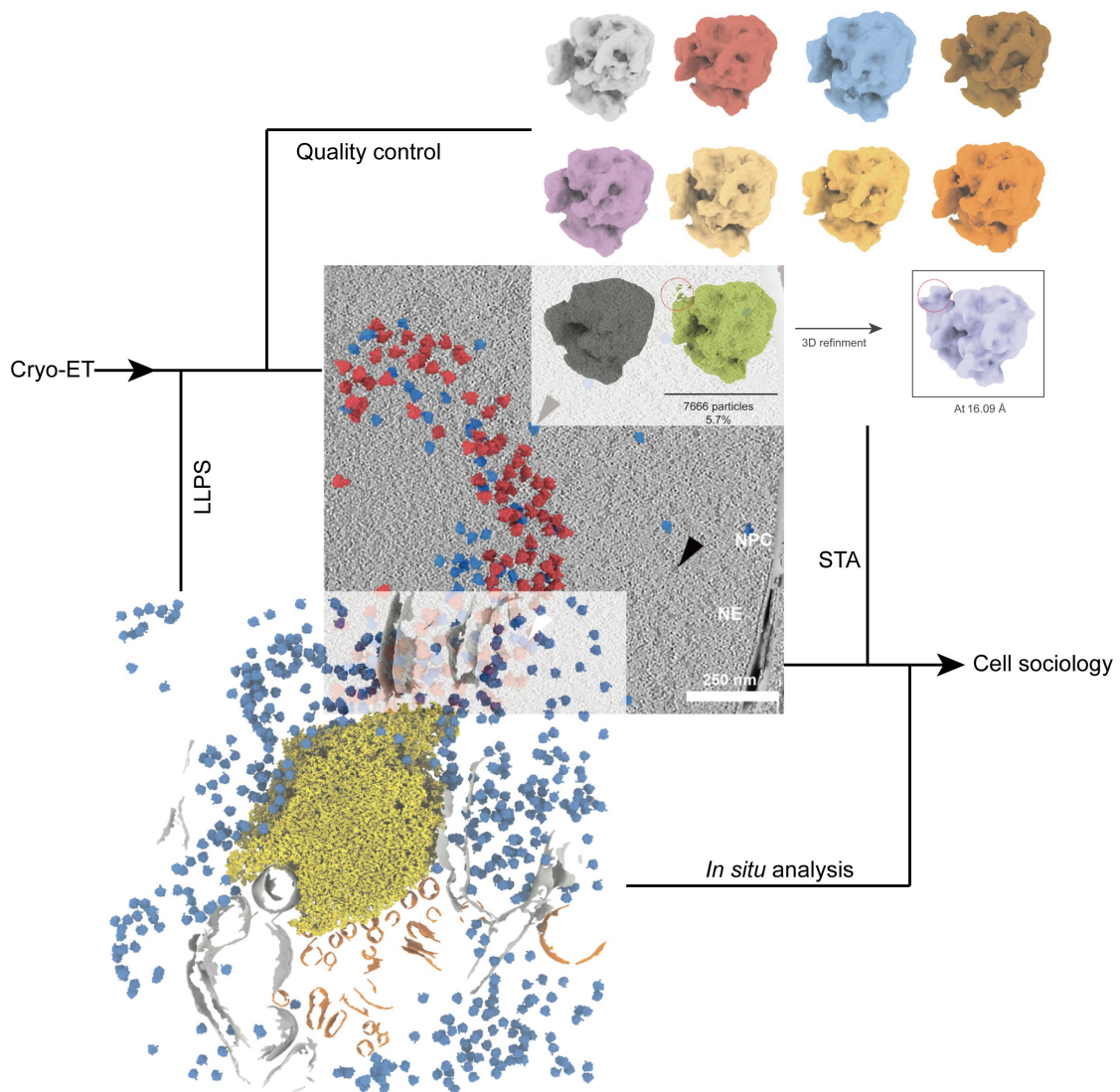
The development of new methods in biochemistry and the advancement in microscopes have enabled scientists to disentangle complicated molecular mechanisms and decipher more protein complexes at an atomic level. However, detailed structural studies of proteins and macromolecular machineries require targeted extraction and purification, through which an information gap between the molecular architecture and its cellular context is created. Over the past years, cryo-electron tomography (cryo-ET), by which one can directly inspect and analyze macromolecules in the cell, has become a powerful tool to bridge the gap. In this dissertation, cryo-ET was applied in studying challenging biological questions that could not be comprehensively addressed by conventional biochemical analyses either due to the indispensability of their native environment or their low occurrence in cells.

My first project examined ribosome biogenesis, which occurs in the nucleolus, a structure that is formed through liquid-liquid phase separation (LLPS) of various liquid-phase nucleolar compartments, but it has not been sufficiently substantiated in previous studies. In my study, distinct *in situ* pre-ribosomal structures were resolved and the spatiotemporal organization of ribosome biogenesis was revealed with liquid-phase nucleolar compartments for the first time, showing how this process is orchestrated through the surveillance of the nucleolar LLPS. Following an interesting discovery of a nuclear-exosome-associated preribosome class in my first project, I set out to explore non-stop mRNA decay (NSD), a mRNA surveillance mechanism in the cytoplasm, in my second project to gain more understanding of ribosome-associated quality control of mRNA. My study demonstrated it to be challenging to obtain *in situ* structures of NSD-related complexes together with ribosomes by cryo-ET. To improve this, I developed new strategies for *in situ* enrichment of NSD-related complexes at specific subcellular structures. The third project, again applied cryo-ET to analyze a special LLPS phenomenon generated by two intrinsically disordered proteins: SLP65 and CIN85, which are involved in B cell activation and protein translocation. Coupled with *in vitro* and *in situ* analyses, I provided a more comprehensive interpretation of SLP65-

CIN85 LLPS to underpin the mechanism by which LLPS effectively regulates protein surveillance and translocation.

In conclusion, this dissertation not only demonstrates the successful application of cryo-ET in studying intricate biological questions, but also provides valuable insights to future comprehensive cryo-ET studies integrated with conventional biochemistry

**Keywords:** cryo-ET, *in situ* analysis, subtomogram averaging (STA), LLPS, ribosome biogenesis, surveillance, NSD, SLP65-CIN85



**Summary figure.** Illustration of key findings and biological connections of projects in this dissertation.

# 1. Methodological Background

## 1.1 Cryo-electron Microscopy

Cryo-electron microscopy (cryo-EM) is an advanced imaging method for acquiring high-resolution information with a transmission electron microscope (TEM) in a cryogenic condition. Cryo-EM has become a major method for structural biologists to decipher the structures of protein complexes since it requires no staining and fixation of the sample, which largely reduces the artifacts and simplifies the workflow.

Similar to light microscopy, the mechanism, by which the TEM produces an image, is affected by two aspects: phase contrast and amplitude contrast ([Dubochet, Adrian et al. 1988](#)). The phase contrast results from the interferences of electron waves at the image plane, it is the major contributor to the image formation in TEM. However, the phase contrast is normally low due to the dominance of unscattered electrons. Thus, defocusing is usually used to increase the phase contrast. Amplitude contrast is generated by backscattered and inelastically scattered electrons, it contributes to low resolution and noises.

A typical TEM composes of: an electron gun, condenser lenses, a condenser aperture, specimen stage, an objective lens, an intermediate lens, a projector lens, an energy filter, and an electron detector (**Figure 1**). The column of a cryo-electron microscope is kept at a high vacuum to avoid the interaction between air and electrons, and constantly cooled by liquid nitrogen to keep the sample vitrified.

The electron gun is used to generate electrons that are the illumination source in a TEM. In a modern TEM, a field emission gun (FEG) is installed, which produces electrons with a much smaller wavelength ranging from 0.020 Å to 0.037 Å under an accelerating voltage (100 kV~300 kV) ([Frank 2006](#)). As is known for light microscopy, the imaging resolution is related to the wavelength of the illumination source, the smaller the wavelength is, the higher the imaging resolution will be. Thus, the imaging resolution of a TEM can theoretically reach the atomic level.

Condense lenses are made of electromagnetic coils, which generate magnetic fields, to condense the emitted electrons into a small and coherent beam. This process does not change the energy of electrons but their direction. High-angle electrons are excluded by the condenser aperture to reduce the noise([Frank 2006](#)).

The specimen stage is computationally controlled to hold the sample grid in a high precise way. The stage can be moved in the range of nanometers and rotated from  $-70^{\circ}$  to  $+70^{\circ}$ ([Erdmann, Plitzko et al. 2018](#), [Turk and Baumeister 2020](#)).

Once the electron beam hits the specimen, parts of it will be transmitted and the objective lens is designed to generate the first intermediate image from the transmitted electrons at the back focal plane. After that, the intermediate image is further magnified by the intermediate lens and eventually projected to the detector by the projector lens ([Frank 2006](#)).

On the way to the electron detector, electrons will go through an energy filter that is set to eliminate the inelastically scattered electrons. Inelastically scattered electrons are produced when the electrons are transmitted through the thick part of the specimen, and they contribute to the low contrast and blurring of the final image. The energy filter is a magnetic prism that disperses electrons based on their energy, allowing electrons carrying a certain range of energy to pass the slit ([Krivanek, Friedman et al. 1995](#)). Therefore, most inelastically scattered electrons will be removed due to the significant loss of energy.

The destination of filtered electrons is the electron detector where electron signals are transformed into images. Nowadays, advanced cryo-EMs are equipped with direct detection detectors that can detect electrons directly, which much enhances the final image quality of final images, allowing much needed resolution advancement in the field. ([Erdmann, Plitzko et al. 2018](#), [Turk and Baumeister 2020](#)).

## 1.2 Cryo-electron Tomography

In the field of structural biology, traditional X-ray crystallography, nuclear magnetic resonance spectroscopy (NMR), and Cryo-EM have been successfully applied in

deciphering structures of various macromolecules including the single protein and protein complexes with DNA/RNA in atomic detail ([van Heel, Gowen et al. 2000](#)). Those unprecedented structures largely broaden our knowledge of protein structures and mechanisms, and play critical roles in developing new drugs that profoundly impact human beings. However, by those methods, cellular components have to be isolated and purified from the cell where different molecules interact with each other in a more and complex way, and studied individually. This is an intelligent but reductionist way ([Gierasch and Gershenson 2009](#), [Cheng 2015](#)). During cell lysis and protein purification, the essential cellular context is lost, and protein conformational dynamics can be altered, and artifacts can be introduced even under well-adjusted protocols. A prime example for the loss of cellular context is liquid-liquid phase separation (LLPS) ([Banani, Lee et al. 2017](#)) studied by conventional biochemistry. Moreover, the authentic illustration of cellular events is not a simple sum of various molecules but a more comprehensive depiction of how molecules are presented in their native environment interacting with different cellular components in a concerted way. Therefore, cryo-electron tomography (Cryo-ET) combined with focused ion beam (FIB) milling is then developed to allow visualizing molecules in unperturbed cellular environments (*in sit* \_

Cryo-ET is a special application of cryo-EM, in which picture frames of the sample are taken over a range of angles (normally  $\pm 60^\circ$ ) as the sample is tilted in a stepwise manner ([Robinson, Sali et al. 2007](#), [Turk and Baumeister 2020](#)) (**Figure 1**).

In cryo-EM single particle analysis (SPA), all electron dose is applied on a single image yielding a high signal-to-noise ratio (SNR) ([van Heel, Gowen et al. 2000](#)), while in cryo-ET, the electron dose applied on each projection is much limited ranging from 2-3  $e^-$ , therefore the SNR of each projection is much lower ([Lucić, Förster et al. 2005](#)). But based on the dose-fraction theorem, the obtainable information is the same if the total electron dose applied in a single projection or a series of projection is the same ([McEwen, Downing et al. 1995](#)). After the acquisition of a series of projected 2D images, the 3D volume of the sample can then be reconstructed, from which the genuine structural information is obtained. Conventionally, various continuous mono- and bidirectional tilt strategies have been used to distribute the electron dose to the best of

different projects, but currently, the dose-symmetric tilt scheme (Hagen scheme) is being widely adopted since it has been reported to significantly improve the tilt alignment for successive reconstruction and reduce the electron radiation damage on the sample at lower tilts where vital high-resolution structural information is obtained ([Hagen, Wan et al. 2017](#)).

However, as most biological samples are thicker than 500 nm through which electrons can hardly penetrate. Thus, extra preparation steps for the thinning of the sample are usually required for cryo-ET ([Marko, Hsieh et al. 2007](#), [Rigort, Bäuerlein et al. 2012](#)). Under the development over the past decades, cryo-ET has been well adopted in a number of studies, including visualizing the native nuclear pore complex, C9orf72 poly-GA aggregates recruiting proteasomes, thylakoid membranes, ribosome biogenesis, etc. Furthermore, the advancement in direct electron detectors significantly improves SNR and the optimization of sample preparation enlarges the range of biological materials that can be studied by cryo-ET ([Faruqi and Henderson 2007](#)).

Cryo-ET is a powerful method in structural biology, but it alone cannot grant us a complete vision of the biological question we are interested in. Multiple interdisciplinary methods including cryo-fluorescence microscopy, scanning EM, and cryo-FIB milling are usually applied together with cryo-ET ([Erdmann, Plitzko et al. 2018](#), [Turk and Baumeister 2020](#)). In addition, the resolution of most *in-situ* asymmetric structures is limited at the subnanometer scale. This limitation is rooted in several aspects, including the electron accumulation that potentially destructs certain structures, the limited pixel size for acquisition, the contamination during sample transferring, the crowded biological context, and the missing wedge problem after the reconstruction ([Davison 1983](#), [Penczek, Marko et al. 1995](#), [Lucić, Förster et al. 2005](#), [Lučić, Rigort et al. 2013](#), [Erdmann, Plitzko et al. 2018](#)). To overcome those challenges, cleaner and faster sample preparation and data acquisition methods are being developed and continuously improved.

In summary, cryo-ET is a state-of-the-art technique that is still under a fast development. It can be applied not only in structural studies to decipher *in situ* protein structures, but also in cellular biological studies to obtain exclusive and native cellular information

that is critical for us to understand the functions of proteins, organelles, and various cellular responses phenomena. e.g., LLPS.

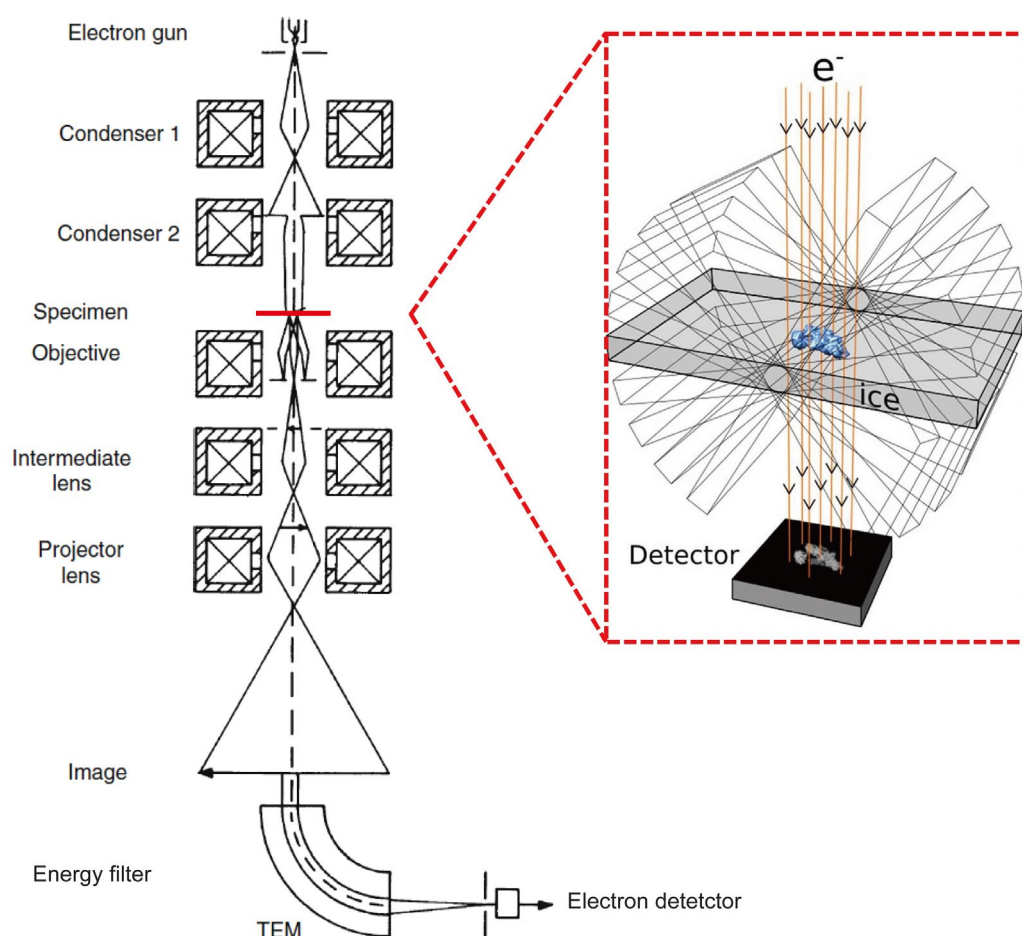


**Figure 1. Overview of a cryo-electron microscope and the schematic of cryo-ET image collection.** On the left panel, a simplified overview of a cryo-electron microscope is shown with an electron gun, two condensers, a specimen stage, an objective lens, an intermediate lens, a projector lens, an energy filter, and a direct electron detector. The specimen holder is colored in red, and on the right panel is the scheme of how cryo-ET is performed in the TEM with a rotating specimen holder. Adapted from Reimer, L. & Kohl, H, 2008 and Koning, Koster, & Sharp, 2018.

### 1.3 Sample Preparation and Focused Ion Beam Milling

The biological sample must be fixed before it is subjected to the electron microscope, and the traditional way to perform that is by chemical fixation in which the dehydration and staining are required. Whereas the dehydration and staining severely damage cellular structures, thus prevent scientists from obtaining high-resolution structures

from classical EM ([Chiu 1986](#), [Dubochet, Adrian et al. 1988](#)). In contrast to this, cryo-EM and cryo-ET, the biological sample is fixed in a more preservative way known as vitrification, by which proteins or cells are instantly frozen in amorphous ice devoid of crystalline ice ([Dubochet, Adrian et al. 1988](#)). The most commonly used vitrification method is plunge freezing. In some studies, high-pressure freezing (HPF) is used when the sample is too thick, for instance, the embryo of *D. melanogaster* ([Studer, Humbel et al. 2008](#)).

To perform plunge freezing, the sample is first applied to or grown on an EM grid and the grid is then rapidly submerged in liquid ethane to achieve an extremely fast temperature drop at a rate of  $10^4$  K/s, which avoids the formation of harmful crystalline ice that damages the biological sample ([Dubochet, Adrian et al. 1988](#), [Iancu, Tivol et al. 2006](#)). For single particle analysis, plunged proteins can be directly examined under the EM. But plunged cells for cryo-ET require further modifications, including cryo-sectioning and FIB milling to thin the sample down to a thickness below 200 nm for a better electron transparency ([Marko, Hsieh et al. 2007](#), [Rigort, Bäuerlein et al. 2012](#)). If the target of interest possesses a particular subcellular localization, cryogenic correlative light and electron microscopy (cryo-CLEM) is applied to localize the target of interest by fluorescence before the thinning process ([Chang, Chen et al. 2014](#), [Liu, Xue et al. 2015](#), [Allegretti, Zimmerli et al. 2020](#)).

Nowadays, the most commonly thinning approach for cryo-ET is FIB milling which originated from material science ([Marko, Hsieh et al. 2007](#)). The FIB instrument is a dual-beam microscope installed with a scanning electron beam and a gallium ion beam. The scanning electron beam is mainly for the imaging on the XY plane and checking the shape and size of lamellae. While the gallium ion beam is for the positioning and sample thinning. FIB milling is performed in a cryogenic condition where the sample stage is constantly cooled (below  $-180^{\circ}\text{C}$ ) with liquid nitrogen. The stage is pre-set to a specific angle for the efficient targeting of the sample by the FIB.

The milling is a stepwise process using two parallel rectangular patterns above and below the target area with a tilting range of  $10^{\circ}$ - $30^{\circ}$  ([Engel, Schaffer et al. 2015](#), [Schaffer, Engel et al. 2015](#), [Schaffer, Mahamid et al. 2017](#)) (**Figure 2**). Prior to the cell

milling, two parallel trenches can be made flanking the cell to release the compressing pressure from the grid. Moreover, to protect the biological sample from the scattering gallium ion, a platinum layer is deposited on the sample through the gas injection system (GIS) ([Rigort, Villa et al. 2012](#)). FIB milling usually commences with a higher ion beam current (0.3-0.5 nA) to clean up the front and back areas, which may otherwise intervene in the subsequent cryo-ET data acquisition, and ends with refining the lamellae with a lower ion beam current (10-30 pA) (**Figure 2 A-F**). An ideal lamella possesses a thickness below 200 nm, and its front side is completely protected with a platinum layer without severe bending ([Schaffer, Engel et al. 2015](#), [Schaffer, Mahamid et al. 2017](#)). Besides, thicker biological samples such as *C. elegans* tissue can also be subjected to FIB milling by applying the lift-out technique ([Schaffer, Pfeffer et al. 2019](#)). However, the production of good lamellae is not high even by a highly experienced FIB user, and the reason lies in several aspects, including the property of the sample itself, artificial bias, the breaching of vacuum, and the redeposition after long-time milling. Promisingly, those issues are being addressed with the advancement in both hardware and software, for instance, the plasma FIB that is cleaner and faster, and the fully automated FIB milling procedure ([Mayr, Finizio et al. 2021](#), [Tacke, Erdmann et al. 2021](#)).

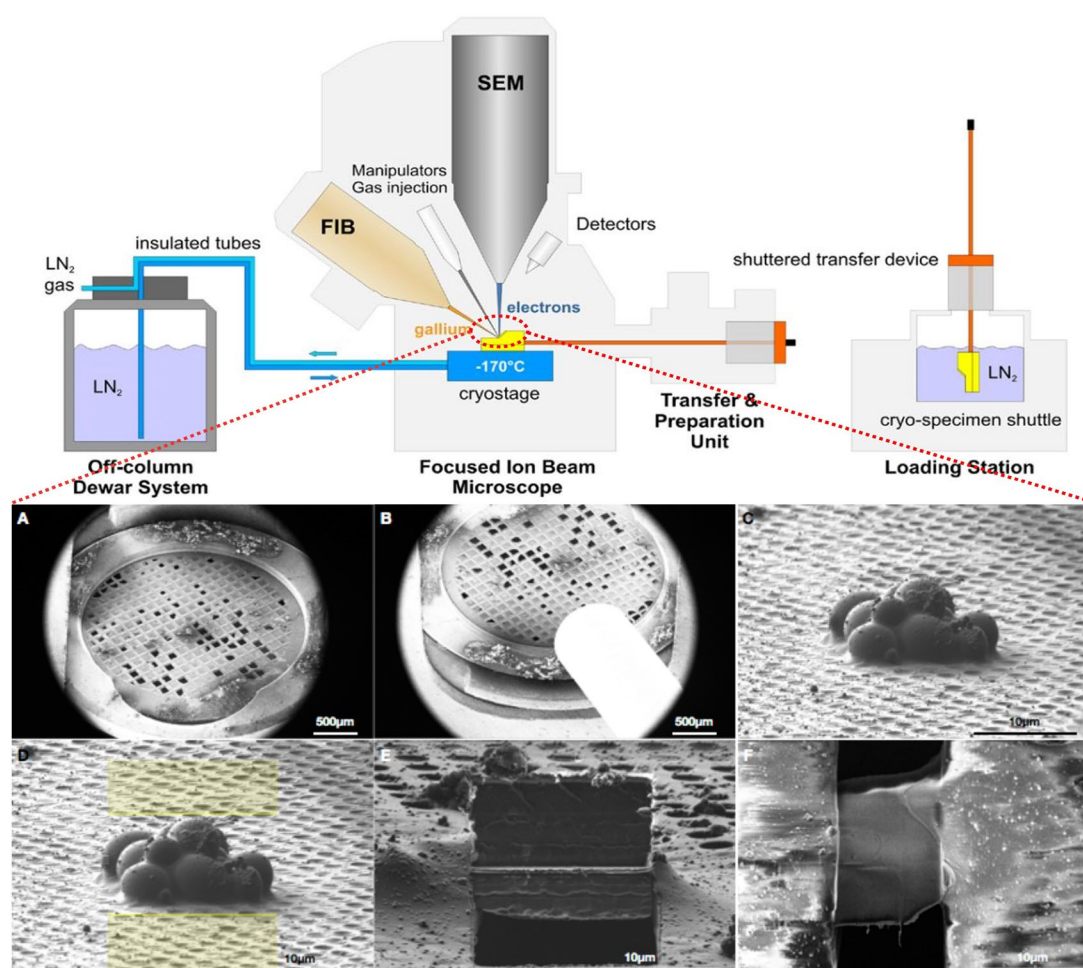


**Figure 2. Schematic illustration of a FIB machine setup and stepwise FIB milling procedures.** In the upper panel is the depiction of the setup of a FIB machine, including an electron gun (SEM), a gallium ion beam gun (FIB), a set of detectors, a cryostage cooled with the liquid nitrogen (LN<sub>2</sub>) gas pumped from an LN<sub>2</sub> tank through insulated tubes, a gas injection system (GIS), and a transfer & preparation unit for docking the specimen shuttle. Adapted from Rigort, Villa, Bäuerlein, Engel, & Plitzko, 2012. On the cryostage in the dotted red circle is the lamella made stepwise, which is further illustrated in the lower panel (A-F) with a yeast sample. (A) The overview of a plunge frozen EM grid with yeasts. (B) The grid is computationally rotated 180° for GIS deposition. (C) A FIB image of the yeasts at 10 pA. (D) The milling pattern is shown with two parallel yellow boxes aimed to mill the back and front of the sample. (E) The FIB image of the milled lamella with a width of ~10 µm and a thickness of ~150 nm. (F) The SEM image of the milled lamella indicates the extent of electron charging, which reflects the thickness of the lamella (the thicker, the more charging and vice versa).

### 1.4 Tomogram Reconstruction

Tomogram reconstruction is a data processing procedure to obtain the 3D volume from a series of 2D projection images. Before the reconstruction, projection images must be correctly aligned and pre-processed. The first step is to correct the electron-induced specimen movement during the data acquisition, known as motion correction ([Henderson and Glaeser 1985](#), [Brilot, Chen et al. 2012](#), [Li, Mooney et al. 2013](#)), and this benefits from the invention of direct electron detectors. The next step is to align the tilt series for a more accurate shift correction and structure determination. In principle, it is performed by bringing all projection images to a common coordinate system. This is usually done by tracking and aligning electron-dense substances, such as gold beads that serve as fiducial markers ([Amat, Moussavi et al. 2008](#)). But for lamellae, it is not practical to induce extra fiducial markers since that can cause unexpected contaminations and damage the integrity of lamellae. Therefore, alignment of tilts from lamellae can be performed by either tracking manually chosen high-contrast cellular features or semi-automated patch tracking. In patch tracking, bad patch points on unstable features (e.g., floating ice particles) need to be removed beforehand. This can be done with functions implemented in the widely used software IMOD ([Harapin, Börmel et al. 2015](#), [Noble and Stagg 2015](#), [Mastronarde and Held 2017](#)). Following that, the defocus value of each tilt shall be determined for the subsequent CTF correction and this can be carried out with different software (e.g., Tomoman) ([Kunz and Frangakis 2017](#)).

After the pre-processing and alignment of tilts, tomograms can be reconstructed based on the projection-slice theorem with different methods, including Fourier synthesis, weighted back-projection, and algebraic reconstruction technique ([Ramachandran and Lakshminarayanan 1971](#), [Marabini, Herman et al. 1998](#), [Radermacher 2007](#)). In Fourier synthesis, a Fourier transform of each projection image is calculated and placed into a plane of a 3D Fourier space, and then a real-space 3D reconstruction is done by the inverse transformation. While in weighted back-projection, the densities from the tilt images are projected into a real-space volume, and there is no need to perform intensive Fourier calculation. In algebraic reconstruction, linear equations corresponding to rays

projecting into tomograms are iteratively calculated, and discrepancies between projections are minimized. Whereas high-resolution information is lost by algebraic reconstruction ([Chen and Förster 2014](#), [Kunz and Frangakis 2014](#), [Turoňová, Marsalek et al. 2015](#)). The most commonly adopted reconstruction method in cryo-ET is weighted back-projection because it is computationally-efficient and high-resolution information is preserved ([Radermacher 2007](#), [Chen and Förster 2014](#)).

However, there is still an obstacle affecting the quality of reconstructed tomograms. That is the missing wedge problem originating from the missing angular tilts during the acquisition. It imposes a major challenge for obtaining higher-resolution information in cryo-ET since it brings distortions and artifacts to the reconstruction ([Natterer 2001](#), [Lučić, Rigort et al. 2013](#)). In previous studies, the double-tilt axis acquisition can mitigate this problem but cannot completely solve it ([Penczek, Marko et al. 1995](#)).

### 1.5 Template Matching

Template matching is a method to find components resembling the given template in an image/volume. In cryo-ET, macromolecules such as protein complexes are the targets ([Nicastro, Schwartz et al. 2006](#), [Förster, Han et al. 2010](#)). In principle, template matching is a filter used to detect and localize patterns corrupted by noise ([Turin 1960](#)). In cryo-ET, a template can be generated with either a low-pass filtered published structure or a primary structure aligned from manually picked particles in the same data set, and the latter one is believed to induce less bias ([Yu and Frangakis 2014](#), [Schaffer, Pfeffer et al. 2019](#), [Martinez-Sanchez, Kochovski et al. 2020](#), [Erdmann, Hou et al. 2021](#)). To perform template matching on tomograms, the 3D volume of reconstructed tomograms is divided evenly based on the given searching box, and all possible same-sized subregions in the tomogram are compared to the template for similarity check. In order to take the local imaging variations e.g., the voxel intensity difference and gray value offset into consideration, a normalization is employed ([Chen, Hrabe et al. 2012](#))(**Figure 3 A, B**).

However, macromolecules in the tomogram are randomly orientated and cannot be matched in only one direction. Thus, they must be searched explicitly. In general, the orientation space is scanned using Euler angles with a specific angular increment, and

the increment is based on the Crowther criterion, typically oversampled by a factor of at least two ([Chen 2015](#)). A common choice for the angular increment is in the range of 7°-15°. During the searching and matching process, a scoring function that yields the information on the similarity between the template and the subregions in the tomogram is computed for each position and orientation. Based on the scores, peaks with a high cross-correlation are picked for the subsequent analysis. To avoid false positives, the threshold for cross-correlation can be adjusted accordingly ([Chen, Hrabe et al. 2012](#), [Hrabe, Chen et al. 2012](#), [Chen 2015](#)).

### 1.6 Subtomogram Averaging

To determine the high-resolution *in situ* structures of macromolecules, subtomogram averaging (STA) is applied (**Figure 3 A**). The general principles involved in STA are similar to those in SPA, extracted subtomograms are iteratively aligned and averaged, in which the relative rotations and shifts between subtomograms and the reference, which is refreshed after each iteration round, are calculated in terms of the cross-correlation ([Frangakis, Böhm et al. 2002](#), [Förster, Pruggnaller et al. 2008](#), [Wan and Briggs 2016](#)). The major difference between STA and SPA is that STA is conducted with 3D data, which limits the particle number in STA since the particles that can be extracted from the tomograms are very limited in a confined biological sample ([Lučić, Rigort et al. 2013](#), [Chen 2015](#)) (**Figure 3 A, C**).

To obtain a better structure, the 3D classification and refinement are performed in STA. The 3D classification is applied to deal the heterogeneity in matched subtomograms, dividing the subtomograms into different groups with distinct features. It can be carried out with different methods, including Principal Component Analysis (PCA), maximum likelihood approaches, and multi-reference alignment and classification ([Frank 2002](#), [Förster, Pruggnaller et al. 2008](#), [Scheres, Melero et al. 2009](#)). The 3D classification is useful not only for inspecting various conformations of the macromolecule and but also to eliminate false positives that affect the final resolution ([Frangakis, Böhm et al. 2002](#), [Hrabe, Chen et al. 2012](#)). Moreover, the focused 3D classification can be performed to distinguish minor differences among classes by applying a mask covering the area of interest ([Yu and Frangakis 2011](#), [Turk and Baumeister 2020](#)). After obtaining clean

classes of subtomograms, the 3D refinement is usually performed. The 3D refinement is a process where the data set is divided into two sets, and the Fourier Shell Correlation (FSC) of each is calculated until convergence is reached ([Förster, Pruggnaller et al. 2008](#), [Chen 2015](#)).

Theoretically, the SNR of the average increases with the iteration number and particle number. The more subtomograms are averaged, the higher resolution is achieved. But it shall not go higher than the Nyquist limit ([Shannon 1949](#), [Saxton and Baumeister 1982](#), [Lučić, Rigort et al. 2013](#)). However, in STA, the final resolution is usually lower than what is expected. That is due to several reasons: the missing wedge, which is normally considered by performing constrained cross-correlations, the irreversible structure damage by electrons, suboptimal lamella thickness, and the limited particle number ([Lučić, Rigort et al. 2013](#), [Erdmann, Plitzko et al. 2018](#), [Turk and Baumeister 2020](#)). To address those problems, better sample preparations and optimization of the computational process are needed.

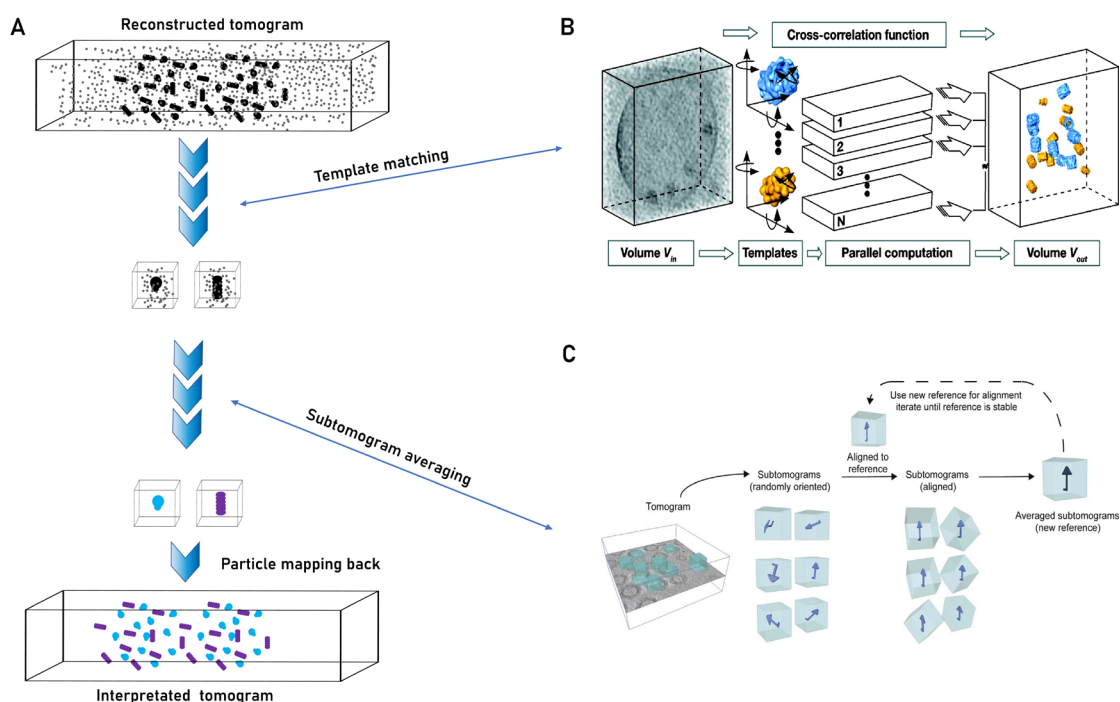


**Figure 3. Schematic illustration of data processing.** (A) Major steps involved in the tomogram interpretation where the tomogram is reconstructed followed by the template matching searching for particular macromolecules of interest, and the matched subtomogram volumes are extracted for the subtomogram averaging, producing a refined structure of the corresponding macromolecules. Ultimately, the averaged particles are mapped back into the

## **Methodological Background**

---

tomogram for a final interpretation with other cellular components. The noise is annotated as gray dots, and targeted subtomograms are colored in black, blue, and purple. (B) Detailed procedures of the template matching, a defined structure is used as an initial template to search the entire volume of the tomogram for matching patterns, and this process is parallelized with a cross-correlation approach. Adapted from Lučić et al., 2005. (C) Overview of STA. Extracted subtomograms are iteratively aligned to a given reference by continuous rotations and shifts, each round will produce a new averaged subtomogram which is used as a new reference for the next iteration until the reference is stabilized. Adapted from Briggs, J. A. 2013.

## 2. Ribosome Biogenesis Project

### 2.1 Introduction and Aims

This section describes the LLPS phenomenon and its pivotal role in multiple essential processes including ribosome biogenesis and B cell activation. Following that, the molecular basis of ribosome biogenesis is introduced based on the latest structural studies. As well, previous studies on the nucleolar organization and its liquid-phase compartments are presented in terms of its relevance with ribosome biogenesis. As various knowledge gaps still exist in our understanding of this intricate processes, aims are set accordingly.

#### 2.1.1 Liquid-liquid Phase Separation

Apart from the well-known membraned organelles in the cell, there exists numerous liquid-phase compartments including the nucleolus, ribonucleoprotein (RNP) granules, centrosome and etc. ([Hyman, Weber et al. 2014](#), [Feng, Jia et al. 2021](#)). They play pivotal roles in in multiple cellular processes, for instance, the liquid-phase compartments in nucleolus are essential for ribosome biogenesis, and the disruption of the the nucleolar LLPS impedes the production of ribosomes and then compromises the growth and proliferation of cells ([Girke and Seufert 2019](#)).

LLPS are known to be composed of distinct classes of proteins that have propensity to interact with each other to form a specialized compartment. Each compartment contains some molecules with a higher concentration than others, and this is normally caused by the nucleation of molecules (**Figure 4**). However, compartments are not entirely separated from each other, they selectively allow certain molecules to pass in between ([Hyman, Weber et al. 2014](#), [Feng, Jia et al. 2021](#)).

In the recent decade, LLPS has been vastly investigated by *in vitro* experiments. In those experiments, liquid-phase compartments are seen as separate liquid droplets and molecules in those droplets remain highly dynamic. Many previous *in vitro* experiments demonstrated that there is a concentration threshold for molecules to undergo nucleation and the minimal concentration is usually higher than the physiological

concentration. Proteins with various binding sites for other molecules are more likely to induce LLPS by mediating multiple intermolecular interactions. Moreover, previous studies also reported that intrinsically disordered proteins are frequently involved in LLPS ([Li, Banjade et al. 2012](#)).

LLPS in cells is known to be dynamic and reversible, which is often related to their functions in intricate molecular processes and in response to environmental stimuli. From previous *in vitro* experiments, it was shown that different compartments in the nucleolus are responsible for the transcription of preribosomal RNAs, synthesis and maturation of preribosomes ([Chen and Huang 2001](#), [Gupta and Santoro 2020](#)) Recent structural studies also reveal various preribosome structures reflecting different stages of ribosome biogenesis ([Baßler and Hurt 2019](#)). However, how those preribosomes are spatiotemporally regulated in those liquid-phase compartments and how those liquid-phase compartments contribute to the transition between preribosomes remain unclear.

Another example is the RNP granules formed in the cytoplasm when cells are under stresses. There are numerous RNPs found in RNP granules and the granules can dynamically transit from liquid phase to solid phase ([Hubstenberger, Noble et al. 2013](#)).

Moreover, cellular LLPS can grow and disperse quickly in response to environmental stimuli, exemplified by a LLPS phenomenon initiated by two proteins SLP65 and CIN8 in B lymphocytes in response to the presence of antigens. This LLPS is stable when B lymphocytes are in a resting mode and disperses quickly once B lymphocytes are activated ([Wong, Maier et al. 2018](#)). The dispersion is believed to be related to the translocation of those proteins, but how that is accomplished in such short time remains unclear through conventional biochemical analysis.

In summary, LLPS in cells is strictly regulated and it interacts with various cellular compartments. Concentrations of molecules in LLPS are precisely controlled by cells to fulfill different purposes such as protein surveillance and translocation. Disruptions of LLPS in cells can negatively affect multiple essential life processes, including emergence of aberrant aggregates, which leads to the development of diseases ([Hyman, Weber et al. 2014](#), [Feng, Jia et al. 2021](#)). However, the property of LLPS makes it

difficult to be comprehensively interpreted without its native cellular environment, which is lacked in most of *in vitro* studies.

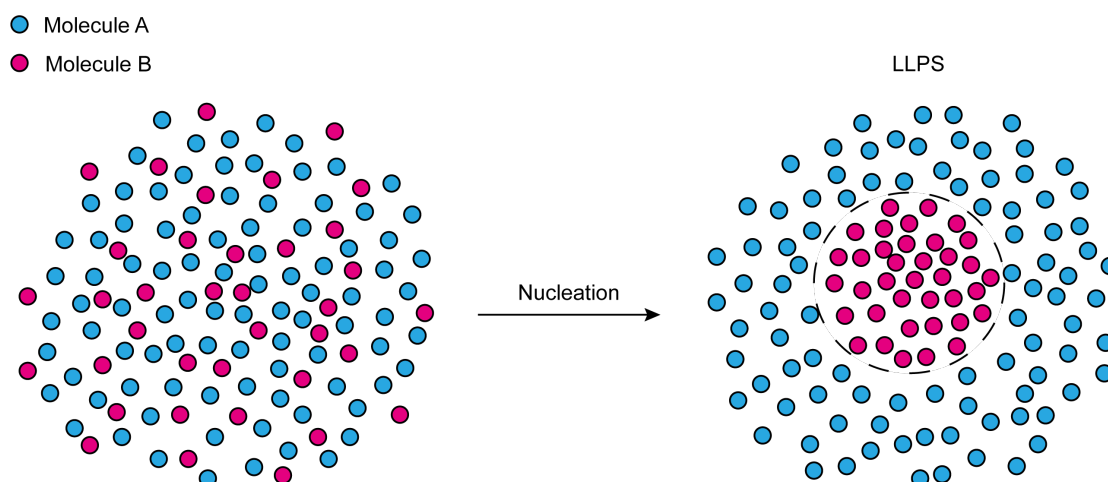


**Figure 4. Simplified illustration of the formation of LLPS.** Two molecules A and B are colored in blue and red, respectively. Molecule B undergoes the nucleation. After that, an invisible boundary (dotted circle) is formed between molecule A and B, indicating the formation of LLPS.

### 2.1.2 Ribosome Biogenesis

Ribosome biogenesis is an intricate and dynamic cellular process where mature ribosomes are assembled in the cytoplasm following the production and export of two subunits, namely the large subunit (LSU) and small subunit (SSU), from the nucleus ([Schäfer, Strauss et al. 2003](#), [Woolford and Baserga 2013](#), [Kater, Thoms et al. 2017](#)) (**Figure 5**). Abnormal ribosome biogenesis is related to human congenital diseases such as Treacher Collins syndrome and Diamond-Blackfan anemia ([Nakhoul, Ke et al. 2014](#)). In eukaryotes, this process is highly conserved across species. A complete functional ribosome is known as the 80S ribosome, based on the sedimentation coefficients in Svedberg units. Its large subunit is defined as 60S subunit, while its small subunit is known as 40S subunit ([Slavov, Semrau et al. 2015](#)). 80S ribosomes are composed of four distinct ribosomal RNAs (rRNAs) and around 80 ribosomal proteins. The large 60S subunit comprises the 25S, 5.8S, and 5S rRNA and ~ 47 ribosomal proteins, while the small 40S subunit is composed of 18S rRNA and 33 ribosomal proteins ([Jenner,](#)

[Melnikov et al. 2012](#), [Klinge, Voigts-Hoffmann et al. 2012](#), [Melnikov, Ben-Shem et al. 2012](#)).

In *Saccharomyces cerevisiae*, ribosome biogenesis is continuous through the entire cell cycle producing ~2000 ribosomes per minute in the log phase ([Shore, Zencir et al. 2021](#)). As a highly energy-consuming and essential process, ribosome biogenesis is initiated with the co-transcription of ribosomal genes in the nucleolus, followed by the assembly and maturation of the 40S and 60S preribosome particles, and ended with the formation of 80S ribosomes in the cytoplasm ([Woolford and Baserga 2013](#), [de la Cruz, Karbstein et al. 2015](#)). This process was first discovered in HeLa cells decades ago by observing the two ribosomal subunits coming from a common large rRNA named 45S preribosomal RNA (pre-rRNA) ([Scherrer, Latham et al. 1963](#), [Warner and Soeiro 1967](#)). In yeast, this large transcript from the ribosomal DNA is identified as 35S pre-rRNA. Successive studies have shown that the 35S pre-rRNA is synthesized by RNA polymerase I (Pol I) in the nucleolus and further processed into 18S, 5.8S, and 25S rRNA in yeast. And the 5S rRNA is synthesized by RNA polymerase III (Pol III) in the nucleolus as well, while snoRNPs that are critical for the early ribosomes assembly are synthesized by polymerase II (Pol II) in the nucleoplasm ([Kressler, Hurt et al. 2010](#), [Fernández-Pevida, Kressler et al. 2015](#), [Turowski and Tollervey 2015](#)) (**Figure 5**). Further processing of the larger rRNA precursor gives rise to preribosomal particles initially uncovered as the 90S, 43S, and 66S preribosomal particles. Still, those particles were not visualized until an electron microscopy technique known as Miller spreads was firstly applied in 1969, which provided unprecedented structural insights to those ribosome assembly intermediates ([Miller and Beatty 1969](#), [Kressler, Linder et al. 1999](#)). Over five decades, numerous assembly factors (AFs) and small nucleolar ribonucleoproteins (snoRNPs) were identified and attributed to the process ([Woolford and Baserga 2013](#)). Recently, structures of various preribosomal particles were resolved at the atomic level with the advancement of cryo-electron microscopy (cryo-EM), vastly enriching our knowledge of the whole process and the function of the relevant proteins ([Kornprobst, Turk et al. 2016](#), [Ma, Wu et al. 2017](#), [Malyutin, Musalgaonkar et al. 2017](#), [Schuller, Falk et al. 2018](#)).

In more detail, ribosome biogenesis starts with the synthesis of a common pre-rRNA noted as 35S pre-rRNA, then different assembly factors and ribosomal proteins associate with it in a co-transcriptional manner to form the processome (90S preribosome) followed by a series of nucleolytic cleavages of the pre-rRNA and dissociation of major complex (U3 snoRNP, UTP-A, UTP-B, and UTP-C) yielding the first 40S preribosome ([Pérez-Fernández, Román et al. 2007](#), [Phipps, Charette et al. 2011](#), [Woolford and Baserga 2013](#), [Hunziker, Barandun et al. 2016](#)) (**Figure 6**). Subsequently, the 40S preribosome is exported to the cytoplasm through nuclear pore complexes (NPC) ([Karbstein 2013](#)), aided by export factors.

In parallel, the early 60S preribosome is formed by assembling assembly factors and ribosomal proteins on the nascent pre-rRNA after the cleavage of internal transcribed spacer 1 (ITS1) ([Baßler and Hurt 2019](#)). Shortly after that, the 5S ribonucleoprotein (RNP) binds the 60S preribosome, and the ITS2 is further processed by continuous endo- and exonucleolytic cleavages by Las1 complex yielding the 7S and 25S pre-rRNAs ([Konikkat and Woolford 2017](#)). The Rix1-lpi3-lpi1 complex and the AAA-ATPase Real come to associate with the 60S preribosome forming a Real-Rix1 complex, which results in the dissociation of the Rpf2-Rrs1 and the rotation of the 5S RNP followed by the dissociation of Nog2 and Rsa1. The foot structure has been reported missing in those corresponding cryo-EM structures ([Baßler, Paternoga et al. 2014](#), [Matsuo, Granneman et al. 2014](#), [Wu, Tutuncuoglu et al. 2016](#)), indicating that the removal of ITS2 is necessary for the successive conformational change (**Figure 7**). Then, the nuclear exosome complex is recruited by Mtr4 to the 60S preribosome to modify the 7S pre-rRNA to 5.8S pre-rRNA, followed by the binding of the export adaptor Nmd3 ([Ma, Wu et al. 2017](#), [Schuller, Falk et al. 2018](#)). Ultimately, the 60S preribosome is translocated into the cytoplasm by the nuclear pore complex ([Karbstein 2013](#)). Upon the release from the nucleus, the 60S and 40S preribosomes undergo the final maturation and quality control steps to form mature 60S subunits and 40S subunits with various ribosomal proteins. The complete 80S ribosome is formed when these two subunits assemble on the request of protein synthesis ([Woolford and Baserga 2013](#)).

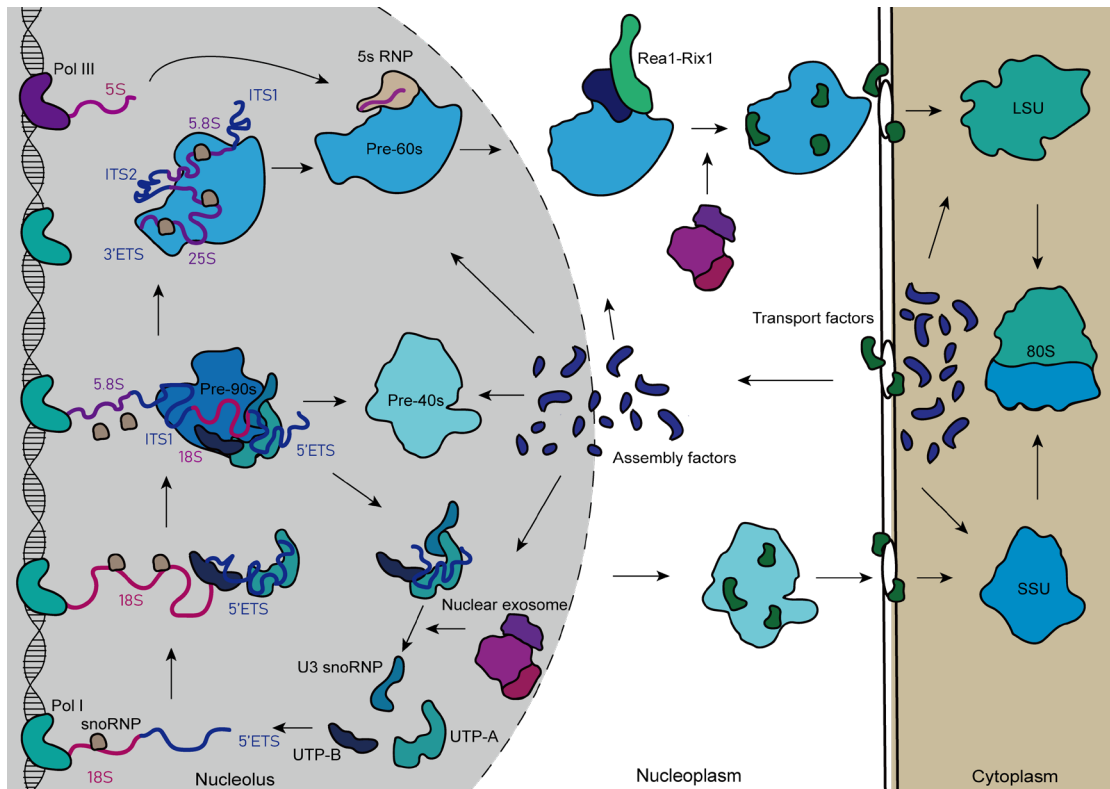


**Figure 5. Schematic show of ribosome biogenesis.** On the upper panel of the graph, the pre-60S particle is formed after the cleavage at ITS1, the pre-formed 5S RNP comes to associate with it, followed by the Rea1-Rix1-dependent remodeling. Subsequently, transport factors are recruited to the pre-60S particle, and the NPC-assisted export takes place; On the lower panel of the graph is the biogenesis of SSU depicted; this process starts with the transcription of the 18S rRNA, and the pre-40S particle is formed after the dissociation of 5'-ETS complex from the pre-90S particle. And then, pre-40S undergoes a series of nuclear maturation processes in the nucleus ended with being exported by transport factors through the NPC; After being exported to the cytoplasm, both pre-60S and pre-40S ribosomes are further processed and finally assembled into the mature 80S.

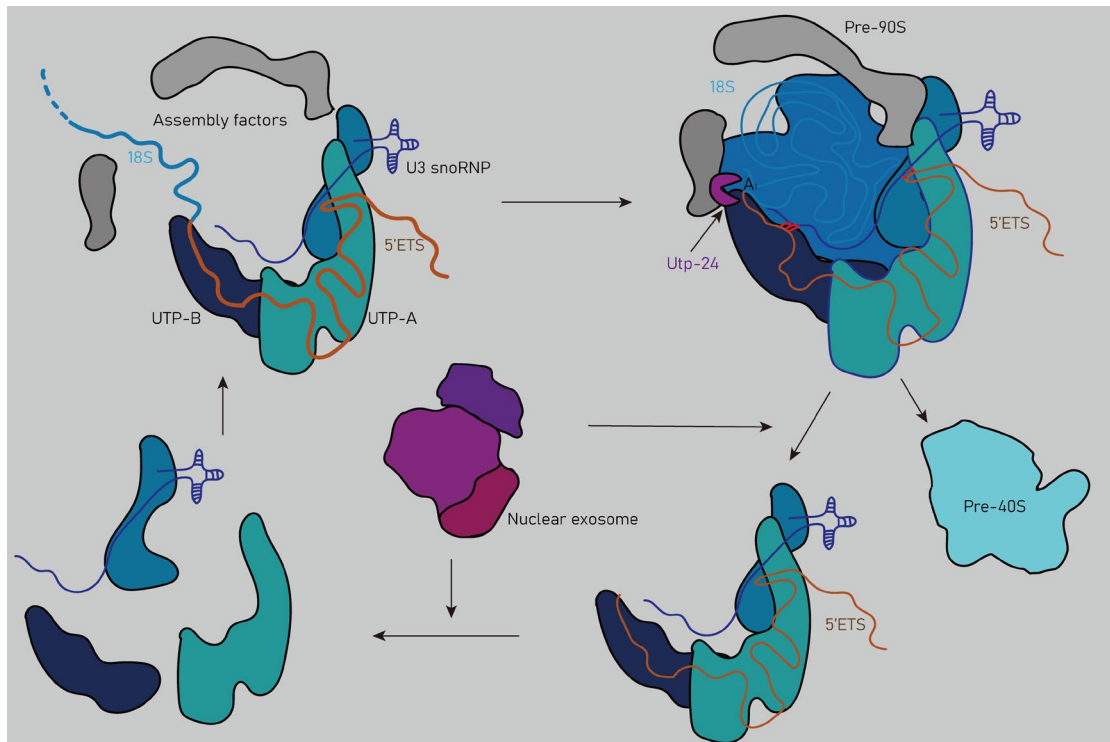


**Figure 6. Schematic illustration of the transition from pre-90S to pre-40S.** Upon the cleavage at the A<sub>1</sub> site by the endonuclease Utp24, the 5'ETS complex is released from the 18S-containing pre-ribosome particle, followed by the maturation of pre-40S. Next, the 5'ETS complex is further disassembled into UTP-A, UTP-B, and U3 snoRNP after being processed by the nuclear exosome on the rRNA, this process can take place on the pre-90S as well. At last, a new pre-90S will form when the 5'ETS complex assembles on the 5'ETS of the nascent rRNA.

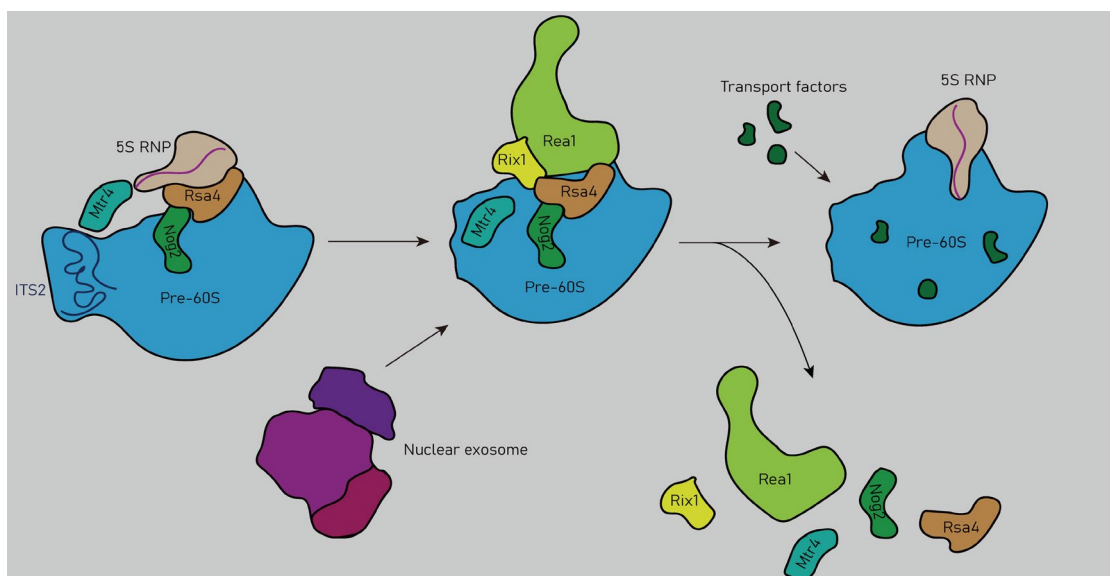


**Figure 7. Schematic illustration of the maturation of pre-60S.** This diagram shows the representative processes happening during the development of pre-60S in the nucleus, in

which the foot structure formed by ITS2 is removed firstly, followed by the recruitment of the Rea1-Rix1 complex to the 5S RNP resulting in a remodeling of the 5S RNP through the rearrangement of the rRNA. The rearrangement of rRNA is induced by Rsa4 which is mechanically affected by the Rea1-Rix1. In the meantime, the nuclear exosome is recruited by Mtr4 to the foot site and further processes the 7S rRNA to 5.8s rRNA. After that, Nog2 which functions a proofreading unit, is released from the pre-60S along with the Rea1-Rix1 and Rsa4, which in turn recruits transport factors including Nmd3, and the pre-60S is sequentially exported to the cytoplasm.

### 2.1.3 The Nucleolar Organization

In eukaryotes, the nucleus is an essential organelle responsible for storing genetic information, the transcription of most mRNAs, and the synthesis of preribosome particles. It is featured with a double membrane and can be explicitly stained with certain dyes such as DAPI and Hoechst ([Hernandez-Verdun 2011](#)). The nucleus composes of three distinct compartments: the nucleolus, the nucleoplasm, and the nuclear envelope, each playing a pivotal role ([Fuchs and Loidl 2004](#), [Montanaro, Treré et al. 2008](#)). The ribosome biogenesis starts within the nucleolus that functions as a factory for synthesizing and processing rRNAs ([Woolford and Baserga 2013](#)). Unlike most organelles, nucleoli are membrane-less structures composed of proteins, DNA, and RNA ([Girke and Seufert 2019](#)). Distinct components can be observed in nucleolus and they are believed to be LLPS since no membrane structures are found. The nucleolus is assembled at the end of mitosis and disassembled at the beginning of the next round of mitosis, and its size increases during the whole interphase, especially between the G1 and G2 phases when it is activated to fulfill the demand of an intensive production of ribosomes which in turn synthesize a large number of proteins for the coming mitosis ([Montanaro, Treré et al. 2008](#), [Hernandez-Verdun 2011](#)). Numerous studies have been carried out to decipher the variability of nucleoli across different species, although most basic structures are highly conserved, there still exist distinct features in different organisms.

In higher eukaryotes, including animals and plants, the nucleolus is usually found in the center of the nucleus and three distinct components have been reported within it by conventional EM: the fibrillar center (FC), the dense fibrillar component (DFC), and the granular component (GC) ([Shaw and Jordan 1995](#), [Lamond and Sleeman 2003](#), [Hernandez-Verdun, Roussel et al. 2010](#))(**Figure 8 A**). Usually, several FCs are present in one nucleolus while only one GC can be seen, DFC is found surrounding the FCs. The FC is an area full of loose fibril-like densities, and the DFC is the dense substance in the vicinity of FCs with a very high contrast by classical EM ([Trumtel, Léger-Silvestre et al. 2000](#), [Feric, Vaidya et al. 2016](#)). The GC can be easily distinguished from the other two components since it consists of a mass of sparsely distributed granules. Over 60 years of studies, different functions have been designated to these three components. The DFC is believed to be the site for the early processing of pre-rRNAs, and the GC is responsible for the late processing. The initial transcription of pre-rRNAs is localized between the FCs and DFC ([Ochs 1998](#), [Hernandez-Verdun, Roussel et al. 2010](#), [Lam and Trinkle-Mulcahy 2015](#)). FCs are also shown to be necessary for the reorganization of nucleoli around the nucleolar organization regions (NORs), and their number increases with elevated transcriptional activity([Derenzini, Farabegoli et al. 1993](#), [Roussel, André et al. 1996](#)).

On the other hand, in lower eukaryotes such as yeast, only a bipartite organization, including the granules (G) and fibrillar stands (F), is observed in the nucleolus ([Trumtel, Léger-Silvestre et al. 2000](#), [Thiry and Lafontaine 2005](#)). Additionally, the nucleolus of yeast is localized on one side of the nucleus and presents a crescent shape ([Matos-Perdomo and Machín 2019](#)) (**Figure 8 B**). Moreover, another difference in yeast nucleolar organization is the absence of condensed chromatin on the periphery of the nucleolus, which is due to closed mitosis without the disassembly of the nucleolus ([Léger-Silvestre, Trumtel et al. 1999](#), [Hernandez-Verdun, Roussel et al. 2010](#)). Under normal conditions, the F can be seen as a homogenous area of fibril-like densities with the granules adjacent to it. However, they cannot be clearly differentiated from each other in classic EM images of the wild type ([Thiry and Lafontaine 2005](#)). Only by conducting mutagenesis of specific genes, such as *srp40* that plays a critical role in

preribosome assembly, can one obtain a clear segregation of G from F ([Ikonomova, Sommer et al. 1997](#), [Hernandez-Verdun, Roussel et al. 2010](#)) (**Figure 8 C,D**).

Despite the absence of DFCs in the nucleolus, yeasts have been shown with more subtle nucleolar structures, such as the nucleolar body and the no body ([Verheggen, Mouaikel et al. 2001](#)). The nucleolar body is a spherical area extending from the F area, and it is believed to be the place where most snoRNAs are modified and matured ([Hernandez-Verdun, Roussel et al. 2010](#)). U3 snoRNA has been used as a probe to detect the nucleolar body, and mutations affecting the accumulation can cause a significant morphological change to the nucleolar body([Qiu, Eifert et al. 2008](#)). No bodies can be detected as condensed puncta containing a mass of pre-rRNAs and RNA surveillance machines ([Andersen, Jensen et al. 2008](#), [Houseley and Tollervey 2009](#)).

Despite considerable research was carried out to characterize the nucleolus and its components in ribosome biogenesis, the relationships between the nucleolar compartments and their putative functions in ribosome biogenesis were based on conventional biochemical and classic EM studies, in which particles were isolated from their native environment, destroying the integrity of LLPS and inducing subtle irreversible artifacts. Moreover, the dynamic transition between various conformations of preribosomal particles was barely illustrated in previous individual studies, our current knowledge of the maturation order of preribosomal particles is largely based on predictions from various structures. Therefore, there is still a need to directly visualize the nucleolar compartments under various bias-free conditions to gain insight for the native processes in ribosome biogenesis and the genuine function of the nucleolar LLPS in regulating those processes.

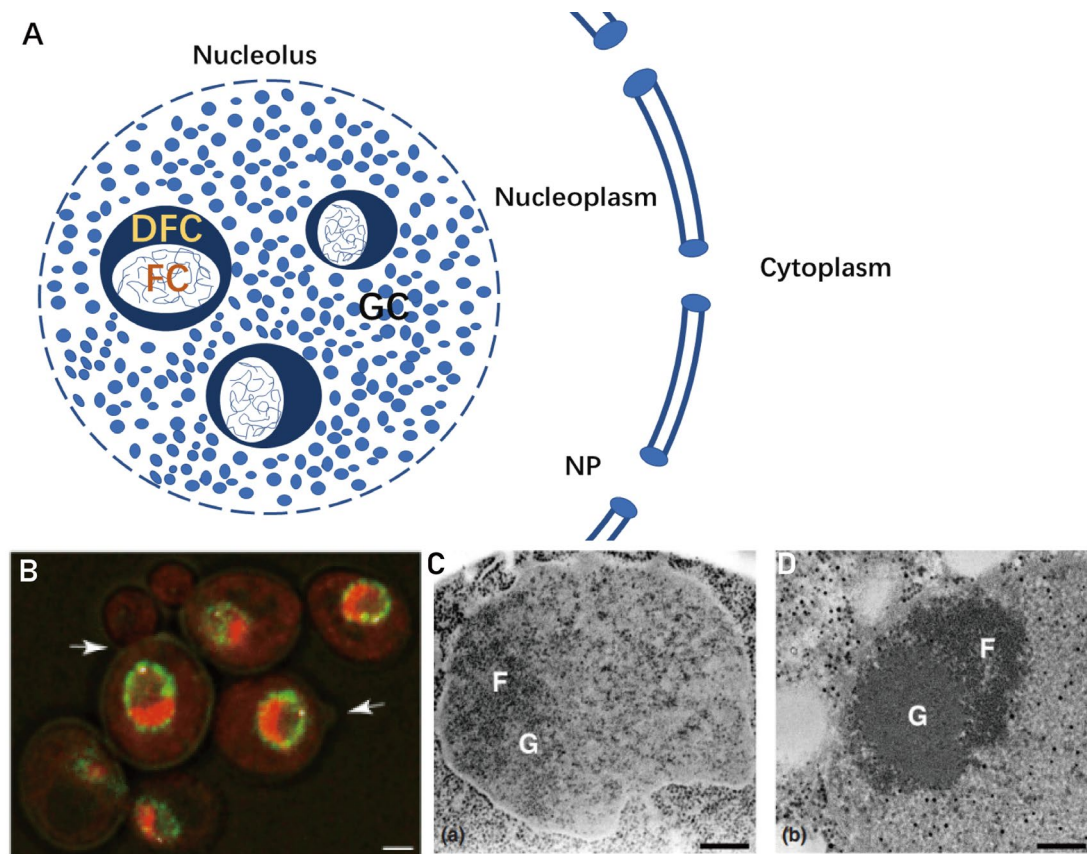


**Figure 8. Nucleolar organization of eukaryotes.** (A) Depiction of the typical tripartite nucleolar organization of higher eukaryotes, in the nucleolus, there exist several fibrillar centers (FCs) surrounded by dense fibrillar components (DFCs). At the same time, the rest is occupied by the granular component (GC). NP: nuclear pore. (B) A fluorescent image of yeast nuclei where the nucleolus is marked by RFP-Nop1 and the nuclear envelope is marked by GFP-Nup4, and the red fluorescence presents a unique crescent shape of the yeast nucleoli. Adapted from Bystricky, K.G., 2005. (C) and (D) conventional EM images of yeast nucleoli show a bipartite nucleolar organization different from higher eukaryotes, F stands for fibrillar stands while G stands for granules. (C) Wild-type yeast, and (D) the *srp40*<sup>-/-</sup> mutant that is defective in ribosome biogenesis. Adapted from Hernandez - Verdun, D., 2010.

### 2.1.4 Aims of the Ribosome Biogenesis Project

To address the abovementioned questions and to conduct an efficient *in situ* study, here are five aims set up in this project:

1. To establish a reproducible cryo-ET workflow for *in situ* analysis of ribosome biogenesis in both *S. cerevisiae* and *C. reinhardtii*.
2. To obtain *in situ* structures of preribosome particles through template matching and STA.
3. To discriminate various classes of preribosomes and analyze the conformational transition between classes.
4. To obtain the spatiotemporal distribution of different preribosomes in the nucleus.
5. To characterize the relationship between preribosomes and liquid-phase nucleolar compartments.

## 2.2 Results

The *in situ* analysis of ribosome biogenesis was carried out in *S. cerevisiae* and *C. reinhardtii*, including deciphering the structure of preribosomal particles and image-based analysis of the nucleolar LLPS. Comparisons were made in terms of the structure and the distribution of preribosome particles. Results from *S. cerevisiae* are covered in the first four sections, and the following sections are focused on *C. reinhardtii*. The work in *C. reinhardtii* has been published in Erdmann et al., 2021.

### 2.2.1 Lamellae Containing Nuclei

*S. cerevisiae* is a robust genetic tool for the study of ribosome biogenesis, thus I first carried out *in situ* cryo-ET studies on ribosome biogenesis in *S. cerevisiae*. To obtain the tomograms of yeast nuclei, I utilized the standard sample preparation workflow for cryo-ET in my project. Since yeasts contain relatively big nuclei, I set up the FIB milling without any correlation at the beginning, and I successfully observed yeast nuclei the lamella. The thickness of lamellae ranges from 100-200 nm. (**Figure 9 A, B**)

Based on the morphology of nuclear pores, nuclei were easily identified with an emblematic double-membrane structure and an elliptical shape. Besides, the inner part of yeast nucleus could be seen as an electron-light region from the TEM overview (Figure 9 C-F). Interestingly, microtubules could be observed in some nuclei, and their orientation was stochastic (Figure 9 E). No obvious segregation of nucleolar compartments was observed in the nuclei at this magnification.

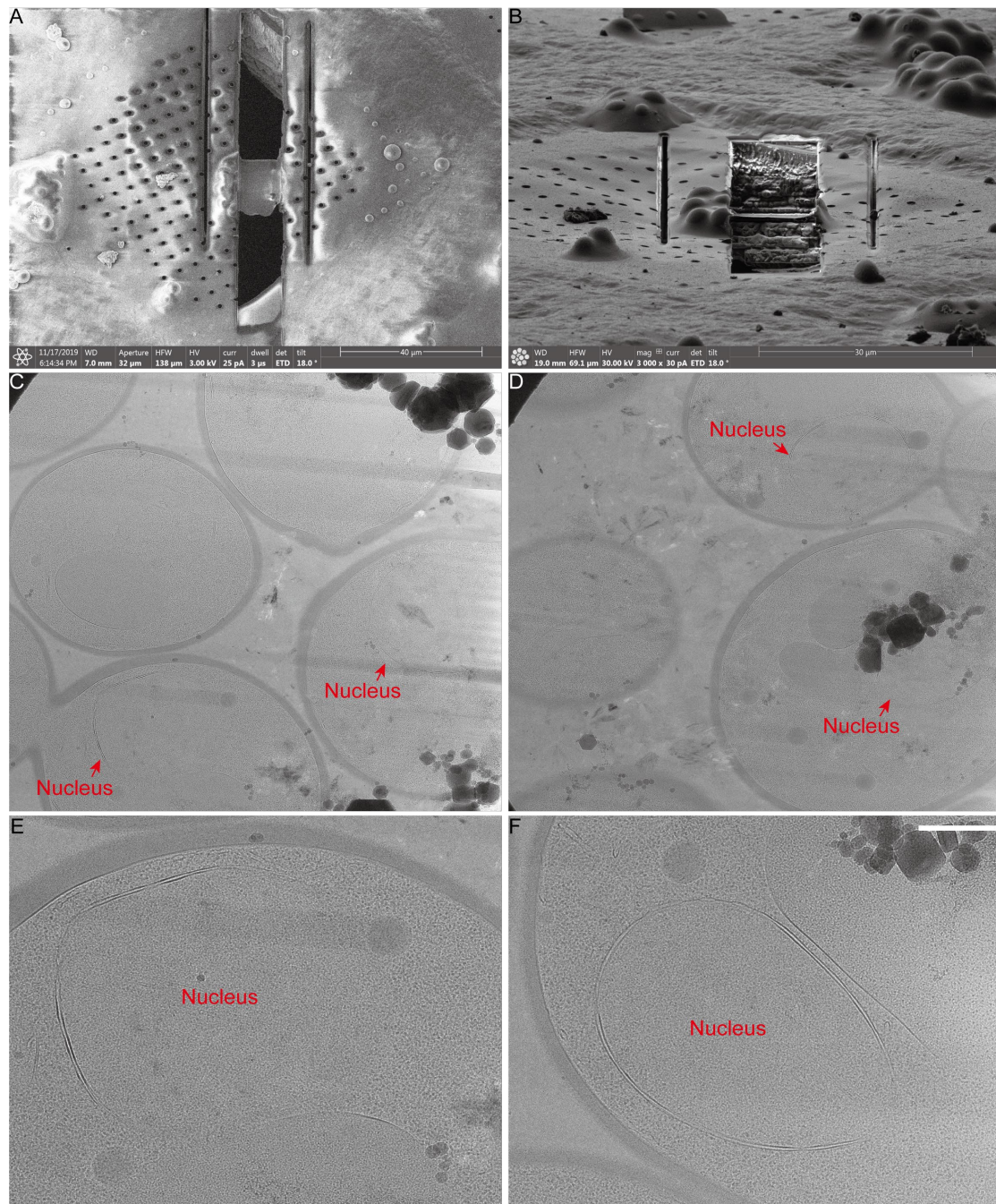


**Figure 9. The overview of yeast lamella.** (A) SEM image of a thin yeast lamella. Imaging conditions are depicted in the lower bar. (B) FIB image of a thin yeast lamella. Parallel trenches

were made flanking the lamella to ease the compressing pressure from the contraction of EM grids. Imaging conditions are noted in the lower bar. (C), (D) TEM overviews of yeast lamellae, nuclei are indicated with red arrowheads. (E), (F) Zoom-in views of yeast nuclei, microtubules are annotated. Scale bar = 1  $\mu\text{m}$ , magnification = 6500x

### 2.2.2 Preribosome-like Particles in *S. cerevisiae*

Tomograms were reconstructed based on the standard in-house workflow and further denoised by CryoCare ([Buchholz, Jordan et al. 2019](#)) for better visualization. From the denoised tomograms, the nuclear envelope, nuclear pore complexes (NPCs), and numerous preribosome-like particles were identified (**Figure 10**). In addition, preribosome-like particles were observed in most parts of the nuclei but more often found along the nuclear envelope, indicating that they were about to be exported by NPCs (**Figure 10**). The sizes of those particles were heterogeneous, implying the existence of different preribosome species.

According to the literature, nucleoli of *S. cerevisiae* are in a crescent shape and are located along the nuclear envelope instead of in the center of the nuclei. However, nucleoli that are identified as electron-dense regions as known from classic EM, were not clearly identified in my tomograms. The distribution of preribosome-like particles did not show a specific directivity and a clustering pattern in the nuclei. Therefore, I decided to perform STA on those particles aiming to differentiate different preribosome species and as well resolve their *in situ* structures.

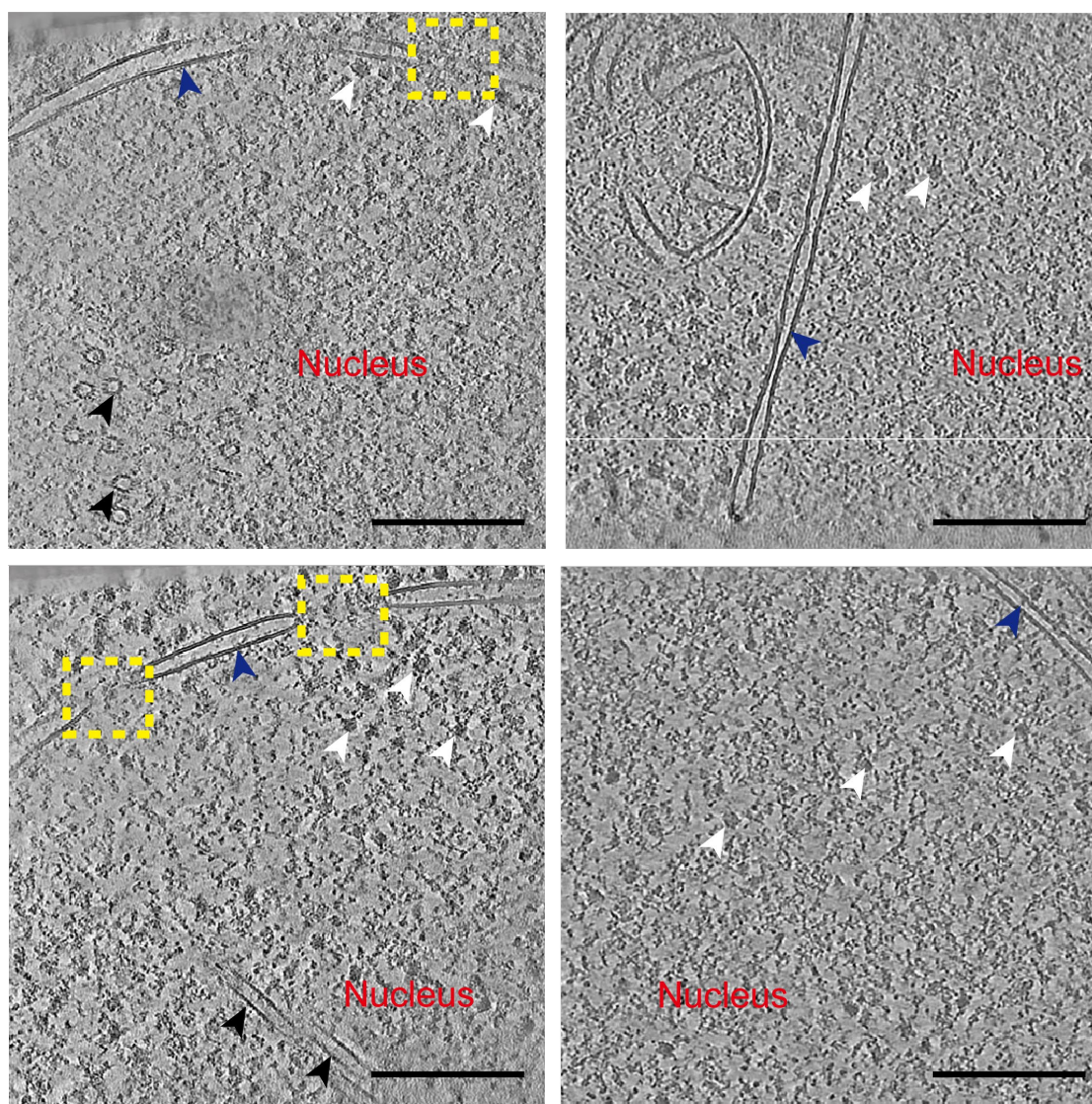


**Figure 10. Reconstructed tomograms of yeast nuclei.** Four representative slices from four tomograms of yeast nuclei are presented. The nuclear envelope is indicated with blue arrowheads, and nuclear pores are indicated with yellow frames. Black arrowheads point to the microtubules, while white arrowheads indicate the preribosome-like particles. Scale bar = 250 nm. Pixel size = 14.08 Å/pixel. Tomograms were denoised with CryoCare.

### 2.2.3 Initial Subtomogram Averaging of Preribosome-like Particles in *S. cerevisiae*

To obtain an initial structure of preribosomes from my tomograms, I deployed a filtered 90S preribosome structure as the template for template matching. In total, 610 particles were extracted from 11 tomograms, and a 90S preribosome structure was resolved at 35 Å. Next, 3D classification was performed and 10 distinct classes were identified (**Figure 11 A**).

Based on the overall conformation of those classes, the ear parts on the top of the 90S preribosome exhibited high flexibility while the core part and UTPA-UTPB-U3 RNP module stayed stable. To verify this structure, structural alignment was performed with two published SPA structures. The alignment showed an overall good fit and the *in situ* 90S preribosome structure appeared to contain extra densities at the periphery areas, which are believed to be crucial for the cleavage on the A<sub>2</sub> site (**Figure 11 B-E**). The resolution of this initial *in situ* 90S preribosome was not high enough to identify more subunits, thus more particles were needed to push the resolution.

### 2.2.4 Further Subtomogram Averaging of Preribosome-like Particles in *S. cerevisiae*

To improve the resolution of this *in situ* structure and mitigate potential template-orientated bias in template matching. I collected more particles and used a featureless template. New tomograms were collected on another cryo-electron microscope with a slightly different pixel size. Then up to 500 preribosome-like particles were manually picked from 10 tomograms and a fast alignment was performed with them to generate an initial bias-free template. In parallel, as a control, I also manually picked up 500 80S ribosomes from the same tomograms and generated an averaged ribosome structure (**Figure 12**). Unexpectedly, the averaged preribosome-like structure did not possess a solid stable structure as the 80S ribosome from the same data set. The size of the averaged structure approximated that of the 80S ribosome, but its morphology was highly flexible, which might be caused by the heterogeneity of preribosomes in the

nuclei. Then I used a featureless sphere structure as an initial model and conducted template matching on 22 tomograms. The extraction number of particles from the score map was also increased for oversampling, and 8455 particles were extracted in total (**Figure 12**).

STA was first performed at bin4 for faster processing, which was intended to clean up heterogenous particles and then proceeded with unbinned data for high-resolution structural analysis. However, after 3D classification, particles were either grouped into 80S ribosomes (in total 17.3%) or presented as uncharacterized particles (**Figure 12**). Nevertheless, unbinned data were subjected to 3D classification, but outputted structures after the classification still remained undefined as what was seen with bin4 data.

Since 80s ribosomes were as well classified out from the STA using the bias-free preribosome template (**Figure 12**), implying that the heterogeneity of preribosomes in yeast largely impeded the accuracy of template matching and interfered with the classification in my STA. Therefore, to identify different preribosome species in yeasts by in situ analysis might require a feasible synchronization of preribosomes to stabilize certain classes.

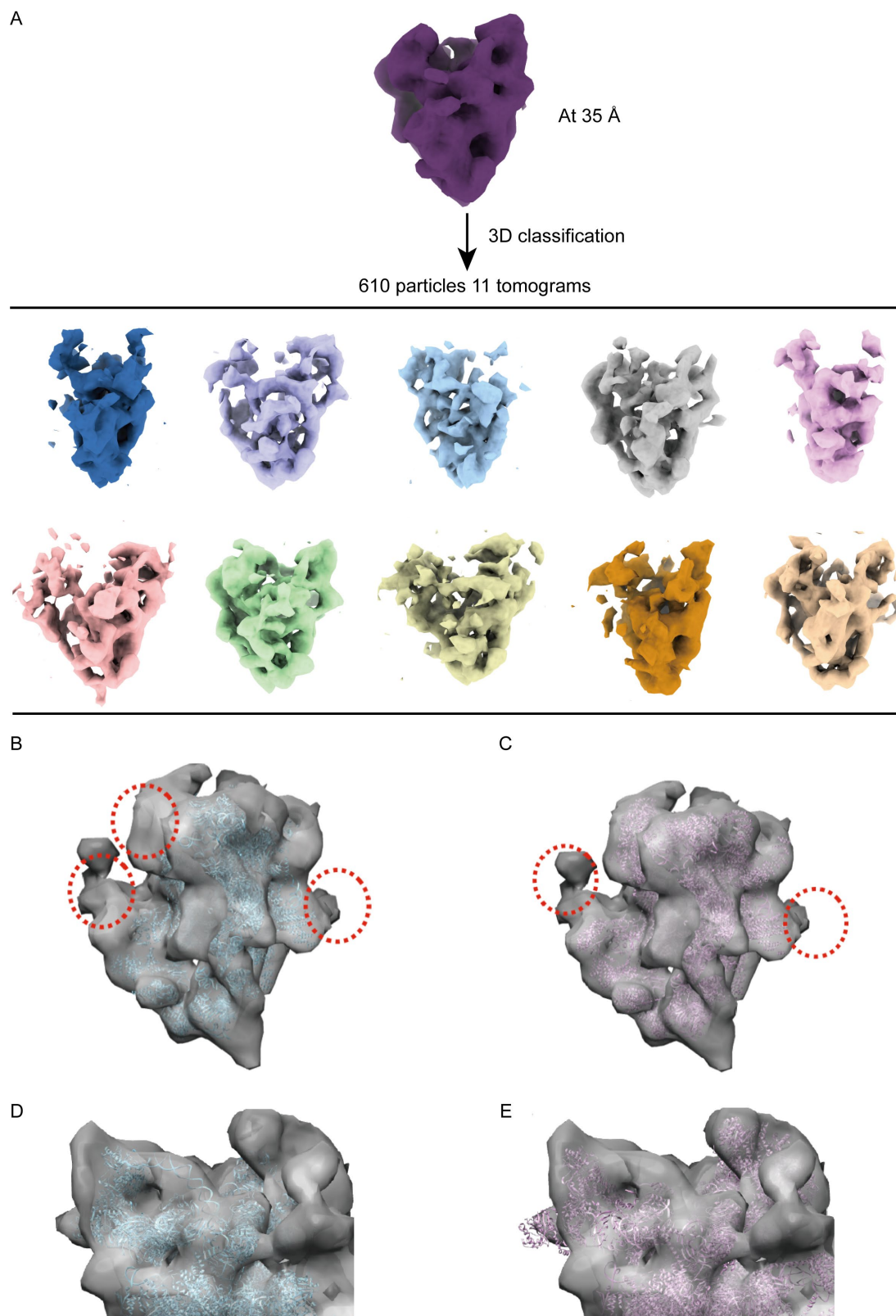


**Figure 11. The initial STA of 90S preribosomes.** (A) Structural overview of *in situ* 90S preribosomes. The averaged structure is displayed in dark purple and 10 classes are colored differently. Pixel size = 13.68 Å/pixel. (B)-(E) Structural alignment of the *in situ* 90S preribosome with published SPA 90S preribosome structures. (B) Structural alignment with EMD-8143.

EMD-8143 is colored in blue, extra densities are indicated with red dotted circles. (C) Structural alignment with EMD-6695. EMD-6695 is colored in light purple, extra densities are indicated with red dotted circles. (D), (E) Zoom-in views of (B) and (C).

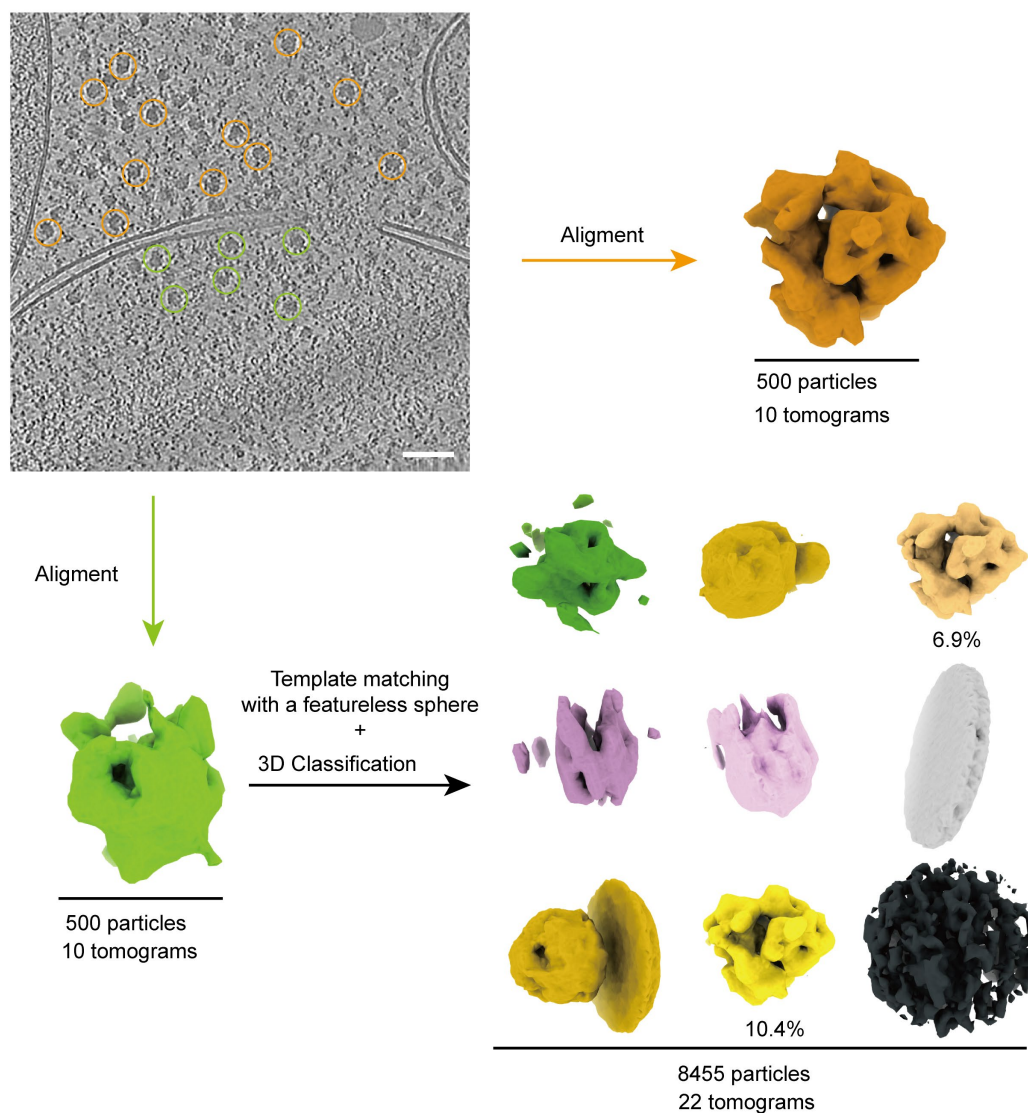


**Figure 12. Further STA of pre-ribosome-like particles.** Manually picked ribosomes are indicated with brown circles, and manually picked pre-ribosome-like particles are indicated with green circles. Initial aligned structures are colored accordingly. Further template matching with a featureless sphere generated by randomizing the orientation of manually picked pre-ribosome-like particles was applied, followed by 3D classification. Ribosome structures from 3D classification are colored in light yellow and pastel brown with corresponding percentages annotated beneath. Pixel size = 14.08 Å/pixel. Scale bar = 100 nm.

### 2.2.5 The Typical Tripartite Nucleolar Organization in *C. reinhardtii*

As an alternative to *S. cerevisiae*, *C. reinhardtii* was also utilized in this project for the same *in situ* cryo-ET study on ribosome biogenesis as it has been shown with a clear compartmentalization of subcellular structures, making it an ideal organism for cryo-ET studies ([Arnold, Mahamid et al. 2016](#)). The study in *C. reinhardtii* was performed in collaboration with Dr. Philipp Erdmann. Similar procedures described in the previous yeast section were adopted to prepare *Chlamydomonas* samples for cryo-ET.

From the reconstructed tomograms of *C. reinhardtii*, the typical tripartite organization of nucleoli was observed, and preribosome-like particles were found in close contact with the nucleoli. Based on the shapes and sizes of the three components (FC, DFC, and GC) (**Figure 13 B, C**), the nucleolar organization preserved in the cryo-ET samples shared a high similarity with that described in conventional EM. Besides, preribosome-like particles were shown in a highly preserved state in the tomograms, which is not achievable by conventional EM (**Figure 13 A**). Moreover, sparsely distributed preribosome-like particles were also found between the nucleoli and nuclear envelopes, which might indicate a maturation route that was not fully described in previous SPA studies.

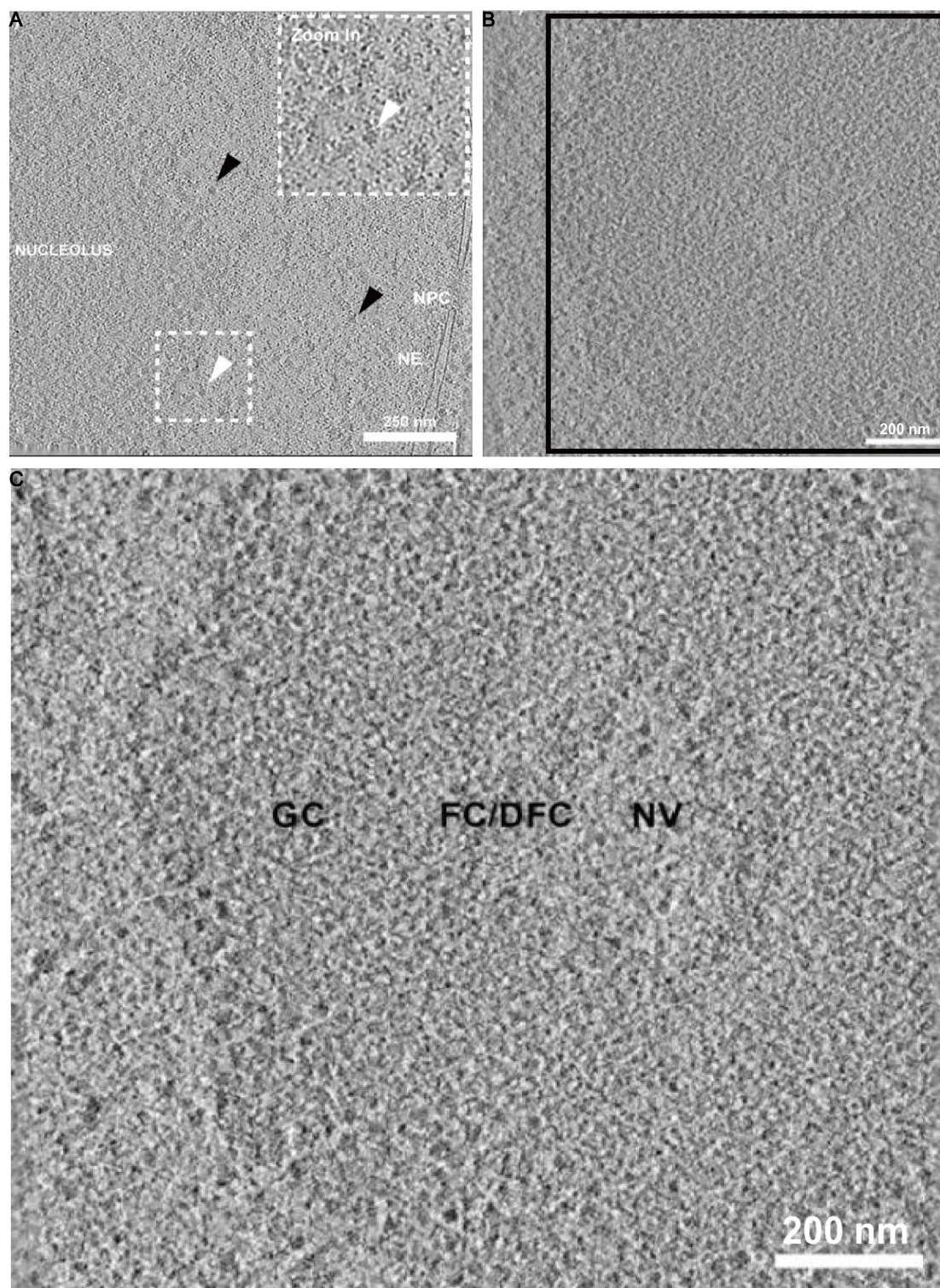


**Figure 13. Illustration of the nuclei and tripartite nucleolar organization in *C. reinhardtii*.** (A) A tomogram slice of *Chlamydomonas* nucleus. Nuclear pore complex (NPC), nuclear envelope (NE). Preribosome-like particles are indicated with arrowheads, white ones indicate the particles decorating the nucleolus, while black ones indicate particles drifting in the nucleoplasm. Part of the decorating particles is enlarged in a white dotted frame and shown on

the upright corner. (B) A tomogram slice of the nucleolus. The part in the black frame is enlarged and shown as (C) for better visualization. Nucleolar compartments are annotated based on their morphologies: GC (granular component), FC (fibrillar center), DFC (dense fibrillar component), and NV (nucleolar vacuole).

### 2.2.6 Subtomogram Averaging of Preribosome-like Particles in *C. reinhardtii*

To further characterize the preribosome-like particles, we set up template matching using an approach designed to reduce the inherent template bias. We manually picked 300 particles and generated a spherical template from them. Then we utilized that featureless template to perform template matching and 3D classification, by which possible structural bias from preferential structure was avoided. Particles were then extracted from 85 tomograms in total. After 3D classification, two dominant types of particles were identified. One resembled the SSU processome and the other resembled the LSU precursor (**Figure 14 A**).

Following that, we conducted further STA on those two particles. The SSU processome structure was resolved at 25 Å and LSU precursor was resolved at 24 Å. Moreover, the 3D localization of the individual species suggested a spherical arrangement. To examine that, we fitted a sphere equation based on the 3D coordinates of matched particles, and the results indicated a high sphericity (**Figure 14 C, D**). In addition, the data also showed that the mean radius of nucleoli in this study is  $599 \pm 29$  nm (mean  $\pm$  SEM;  $n = 26$ ), which is consistent with previous studies. However, there was a significant difference in the localization of SSU processome and LSU precursor. SSU processome appeared to have a sharp drop in numbers after leaving the surface of nucleolus assessed by plotting their probability density function (PDF) (**Figure 14 B**).

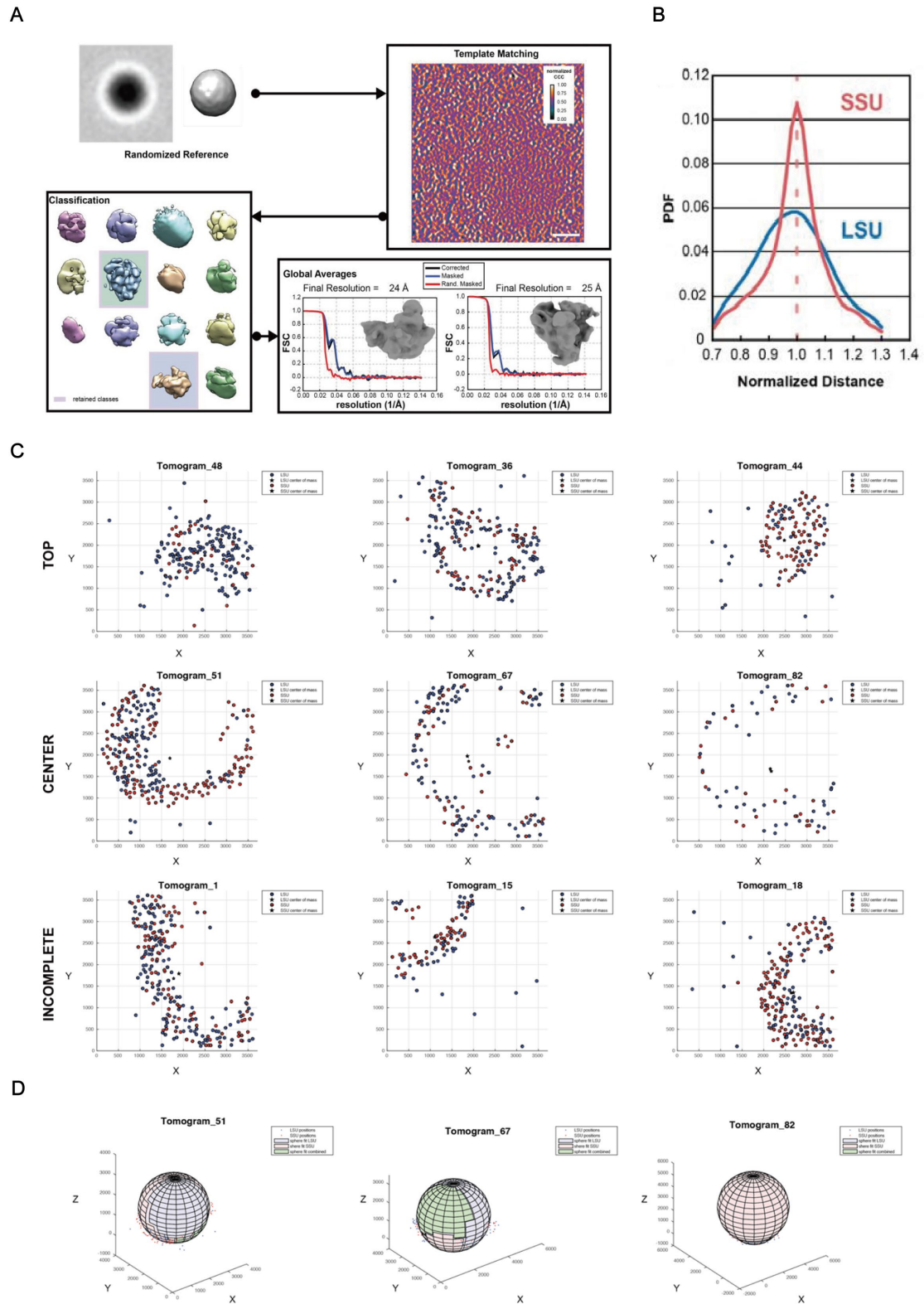


**Figure 14. Characterization of SSU processome and LSU precursor.** (A) The scheme of template matching and classification against preribosome-like particles, different classes are in different colors, and retained classes are in pastel purple frames. The final resolution is presented with an FSC graph. (B) The probability density function of SSU processome and LSU

precursor. SSU is presented with a red curve, while LSU is depicted with a blue curve. (C) Positions of preribosome particles that were mapped back in corresponding tomograms after template matching. Graphs are presented in the XY dimension. SSU is in red, and LSU is in blue. (D) Sphere fitting with preribosome particles in a 3D space. Blue dots are LSU precursors, while red dots are SSU precursors.

### 2.2.7 Classification of SSU Processome and LSU Precursors in *C. reinhardtii*

Apart from preribosome particles on the surface of nucleolus, smaller densities were also observed in the nucleolar center, which could be intermediates of ribosome biogenesis. To further characterize the relationship between ribosome biogenesis and nucleolar liquid-phase compartments, we thus set up an image-based analysis on the apparent particle mass of smaller densities along the distance from the center of the nucleolus (**Figure 15 A**). The analysis showed that the apparent mass keeps increasing from the nucleolar center to the surface, indicating the major association of assembly factors is restricted within the nucleolus. Additionally, the apparent mass stays stable in the nucleoplasm after departing from the nucleolus, the highest peak appears on the surface of nucleolus (**Figure 15 B**). Based on this result, we conclude that the average mass of ribosome-biogenesis-associated particles reaches maximum on the surface of the nucleolus, and the adjacent GC plays a pivotal role in hosting those association events.

Since no structured particles in the nucleolar center could be subjected to STA due to the highly dynamic nature of the early stage of ribosome biogenesis, we thus explored the later stages of ribosome biogenesis taking place towards the nucleoplasm by subjecting SSU processome and LSU precursor to another round of template matching and 3D classification using truncated early-obtained SSU and LSU structures. Strikingly, three different classes were identified for SSU processome and LSU precursor, respectively (**Figure 16**). Cross-effect analysis was conducted to examine the validity of SSU processome and LSU precursor classes. The analysis showed a distinct clustering of classes and no preferred orientation for those classes (**Figure 17**).

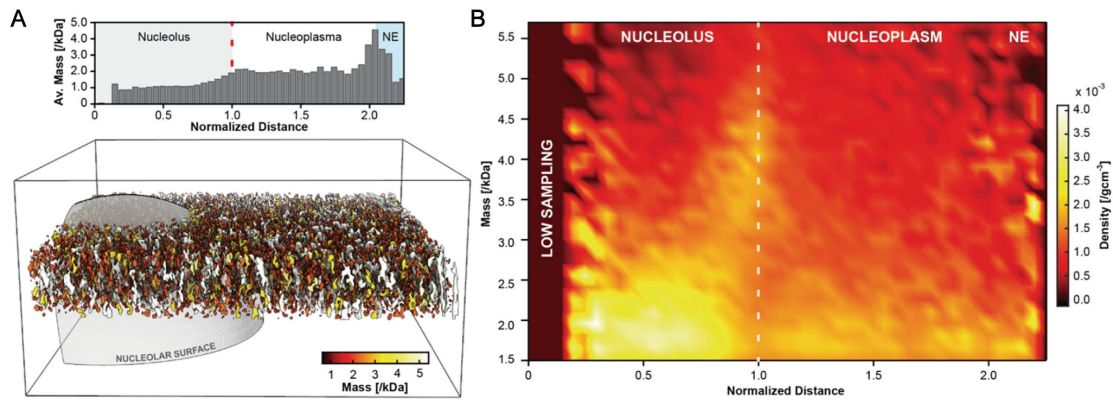


**Figure 15. Image-based analysis of nuclear particles.** (A) Graph of the average apparent mass of particles against their normalized distance to the nucleolar surface. There is a noticeable increase in the apparent mass within the nucleolus towards the nucleolar surface, and the apparent mass stays stable in the nucleoplasm and peaks again on the nuclear envelope. (B) Spectral analysis of particle mass against normalized distance to the nucleolar surface. The level of particles with a size up to 2.5 MDa is constantly high, and there appears a peak of mass on the nucleolar surface where SSU and LSU precursors are detected.

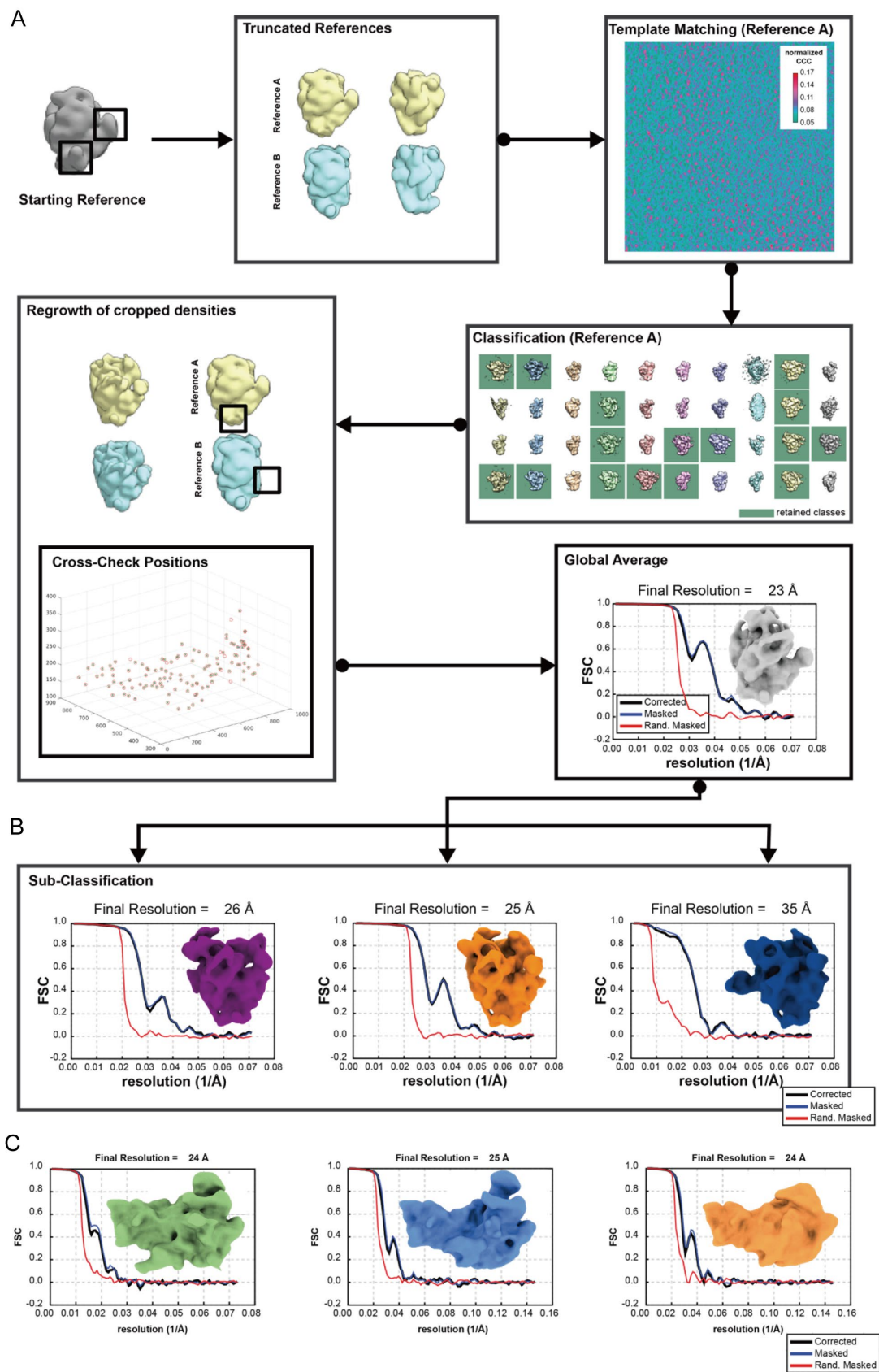


**Figure 16. Further classification of SSU processome and LSU precursor.** (A) Schematic illustration of the bias-mitigated strategy for classification of SSU processome. Two low-pass filtered references were computationally truncated on two conformational features. Only

classes that have the truncated features recovered were selected. Following that, the positions generated from two sets of template matching with those two references were cross checked, only positions present in both lists were kept. The same procedure was applied to LSU precursor. (B) Three SSU processome classes were identified. Final resolution is 26 Å for class 1, 25 Å for class 2, and 35 Å for class 3. (C) Three LSU precursor classes were identified with a final resolution of 24 Å, 25 Å, and 24 Å, respectively.

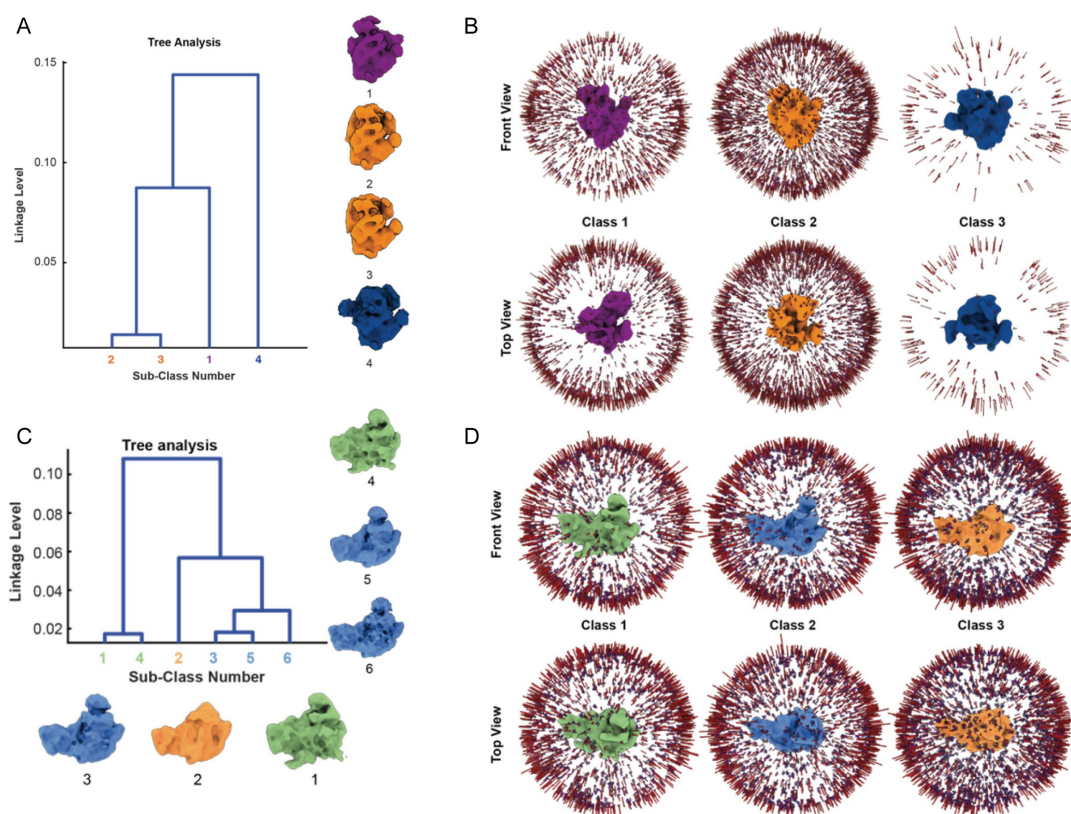


**Figure 17. Cross-effect analysis of SSU processome classes and LSU precursor classes.**

(A) Representative tree-cluster of a Relion 2.1 3D classification with six SSU processome classes, two of which came out empty and were discarded. (B) Angular distribution plots of three SSU processome classes. No preferred orientation was detected all three classes. (C) presentative tree-cluster of a Relion 2.1 3D classification with six LSU precursor classes. (D) Angular distribution plots of three SSU processome classes. No preferred orientation was detected all three classes,

### 2.2.8 Maturation of SSU Processome and LSU Precursor in *C. reinhardtii*

Since the morphology of SSU processome classes varied dramatically, so did that of LSU precursor classes, a conformational transition between classes was conceivable for both SSU processome classes and LSU precursor classes. This conformational transition shall comply with a maturation order in ribosome biogenesis. To verify that, we examined the normalized distance from both SSU processome and LSU precursor classes to the nucleolar center. The result showed that a significant difference existed among classes from both SSU processome and LSU precursor in terms of the distance to the nucleolar center (**Figure 18**). For the SSU processome, class 1 was the closest to the nucleolar center while class 2 was relatively farther from the center. The averaged distance of class 3 to the nucleolar center was the largest (**Figure 18 A**). Similar results were presented for LSU precursor classes: class 1 was the closest, followed by class 2, and class 3 was the farthest (**Figure 18 B**). Therefore, a maturation order from class 1 to class 2, and then to class 3 was hypothesized for both SSU processome and LSU precursor.

To test that hypothesis, we cultured *Chlamydomonas* cells in different conditions and analyzed the abundance of the three classes of both SSU processome and LSU precursors in those conditions. The results showed a progressive maturation for both SSU and LSU preribosome particles. For SSU processome, class 1, which was found most abundant in the dark environment and when ribosome biogenesis was blocked by inhibiting biogenesis of LSU with diazaborine (DAZ) (**Figure 19 A**), was believed to be the earliest conformation of SSU processome among the three classes. Class 2 that was shown dominating in the stationary phase (**Figure 19 A**) was then assumed to be the successive conformation of SSU processome after class 1. Class 3 was found the least abundant in all conditions (**Figure 19 A**), indicating that the existence of class 3 was very transient. Therefore, combining the results from the distance analysis, class 3 was assigned to be the final conformation of SSU processome among the three classes.

For LSU precursors, similar results were obtained. Class 1 was the most abundant in the dark environment and in the DAZ treated condition. Class 2 became the most abundant in the stationary phase. Class 3, which was found slightly more dominant in log phase was then assigned to be the last conformation in the maturation of LSU precursor in this study (**Figure 19 B**).

Next, the three classes of both SSU processome and LSU precursors were compared to published structures from different organisms (**Figure 20 A**). For SSU processome, the results presented an overall good fit for all three classes with the published structures. Among the three classes, class 2 showed the highest similarity to all published structures, while class 1 and 3 appeared to be more different (**Figure 20 B**). In comparison, class 1 displayed a more open conformation than published SSU processome intermediates, with the 5' domain distinctly shifted away from the central domain. Thus, class 1 was further confirmed as the early state of SSU processome. In contrary, class 3 had a more compact conformation than the other two, and this conformation could be essential for the final transition from SSU processome to the 40S preribosome. When compared to the PDB map 5WLC and density map EMD-11808, class 3 was confirmed as the late conformation of SSU processome with a prominent density next to Utp14 at helix 8 and 9 within the 5'ETS RNA (**Figure 20 D, E**). This density is presumed to be the binding site of MTR4 and the nuclear exosome complex ([Kowalinski, Kögel et al. 2016](#)). This finding is in a good agreement with previous studies where the nuclear exosome participates in the modification of preribosomes, especially during the transition of SSU processome to the 40S preribosome ([Hunziker, Barandun et al. 2016](#)). Likewise, the alignment of LSU precursor classes 1-3 with published structures was good and presented a consistency with the maturation order suggested by previous analyses in this study (**Figure 20 C**).

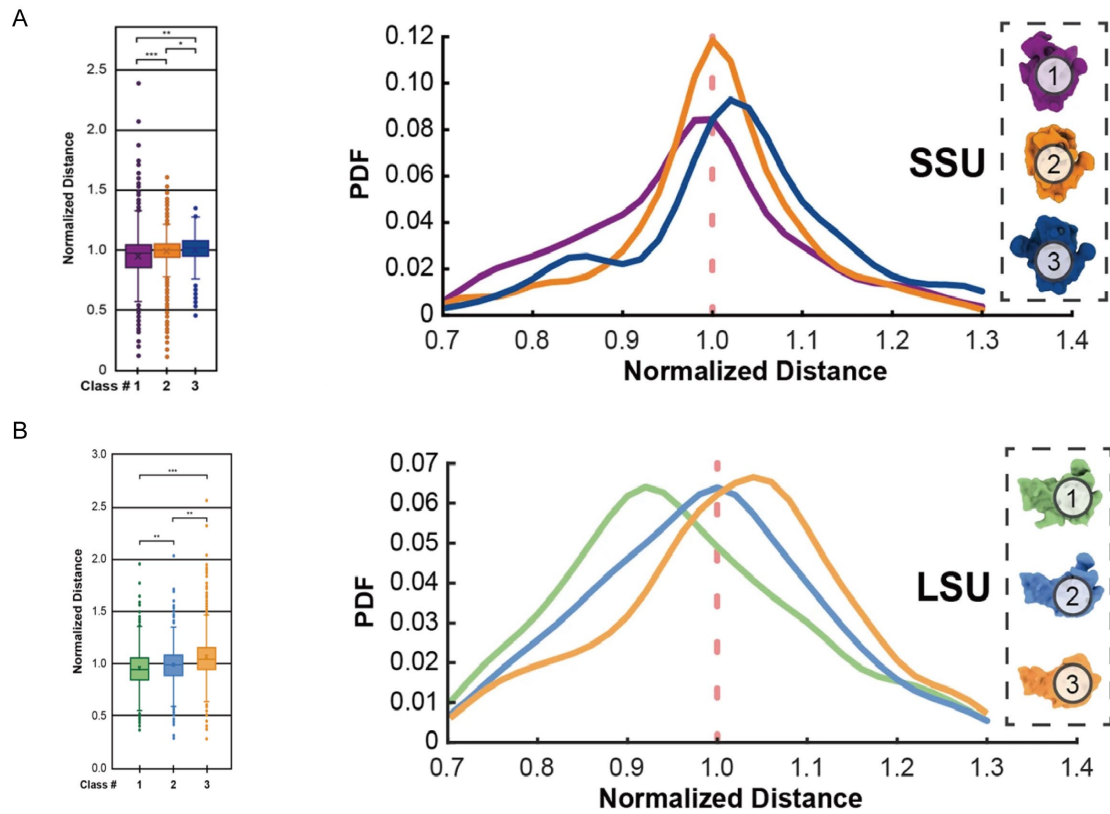


**Figure 18. Analysis on the distance of SSU processome classes and LSU precursor classes to the nucleolar center.** (A) The distance of 3 SSU processome classes to the nucleolar center. The significance was validated by two-sided Fisher-Pitman permutation test of mean:  $p_{1,2} = 1E-6$ ,  $p_{1,3} = 1.07E-04$ ,  $p_{2,3} = 4.1E-02$ ;  $n = 1809$  particles. PDF shows significant different distribution of three processome classes, the average distance of class 3 to the nucleolar center is the largest, followed by class 2. Class 1 is the closest to the nucleolar center. (B) The distance of LSU precursor classes. Permutation test mean:  $p_{1,2} = 1E-06$ ,  $p_{1,3} = 8.84E-04$ , and  $p_{2,3} = 1.59E-04$ . Just like the SSU processome, PDF of LSU precursor classes shows a maturation-related pattern from class 1 to class 3.

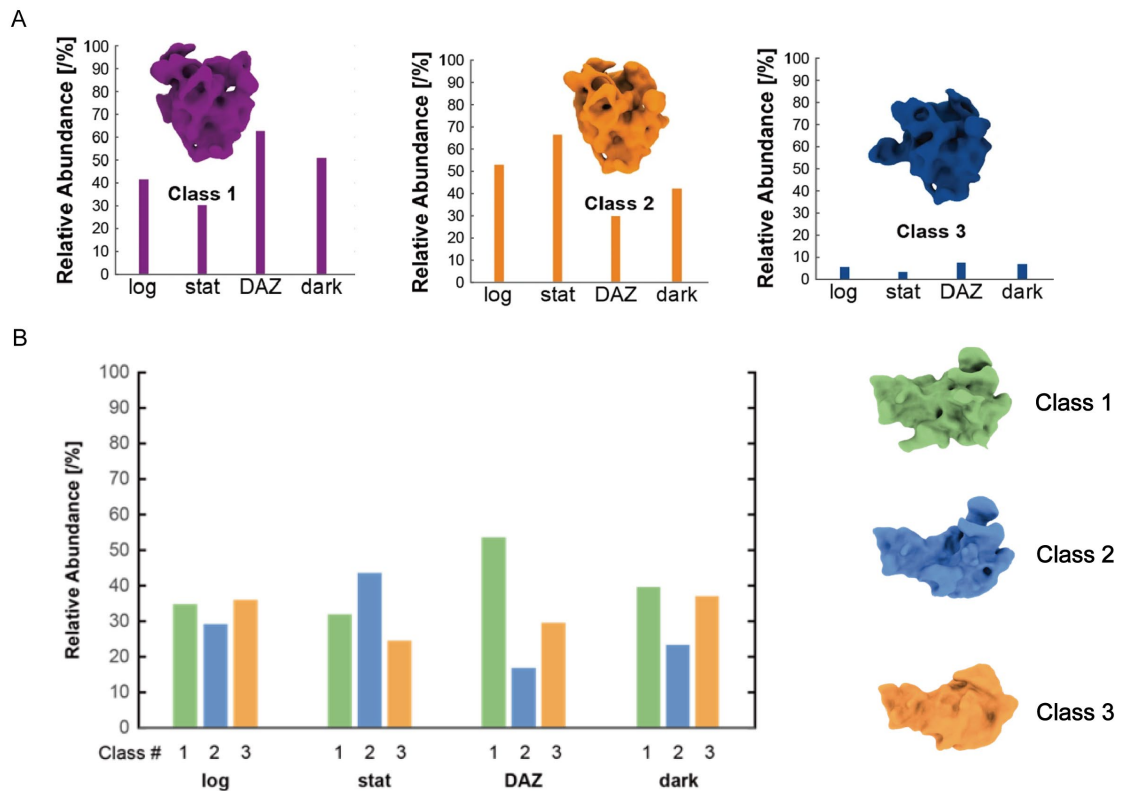


**Figure 19. Assessment on the abundance of SSU processome classes and LSU precursor classes in different conditions.** (A) The abundance of 3 SSU processome classes in different conditions. Class 1 dominates upon the treatment of diazaborine and in the dark environment, class 2 dominates in stationary phase, class 3 is the least abundant in all conditions. (B) The abundance of 3 LSU precursor classes in different conditions. Class 1 dominates upon the treatment of diazaborine and in the dark environment, class 2 is the most abundant in stationary phase, class 3 slight dominate in log phase. Log = log phase; stat = stationary phase; DAZ = diazaborine; dark = dark environment without light.

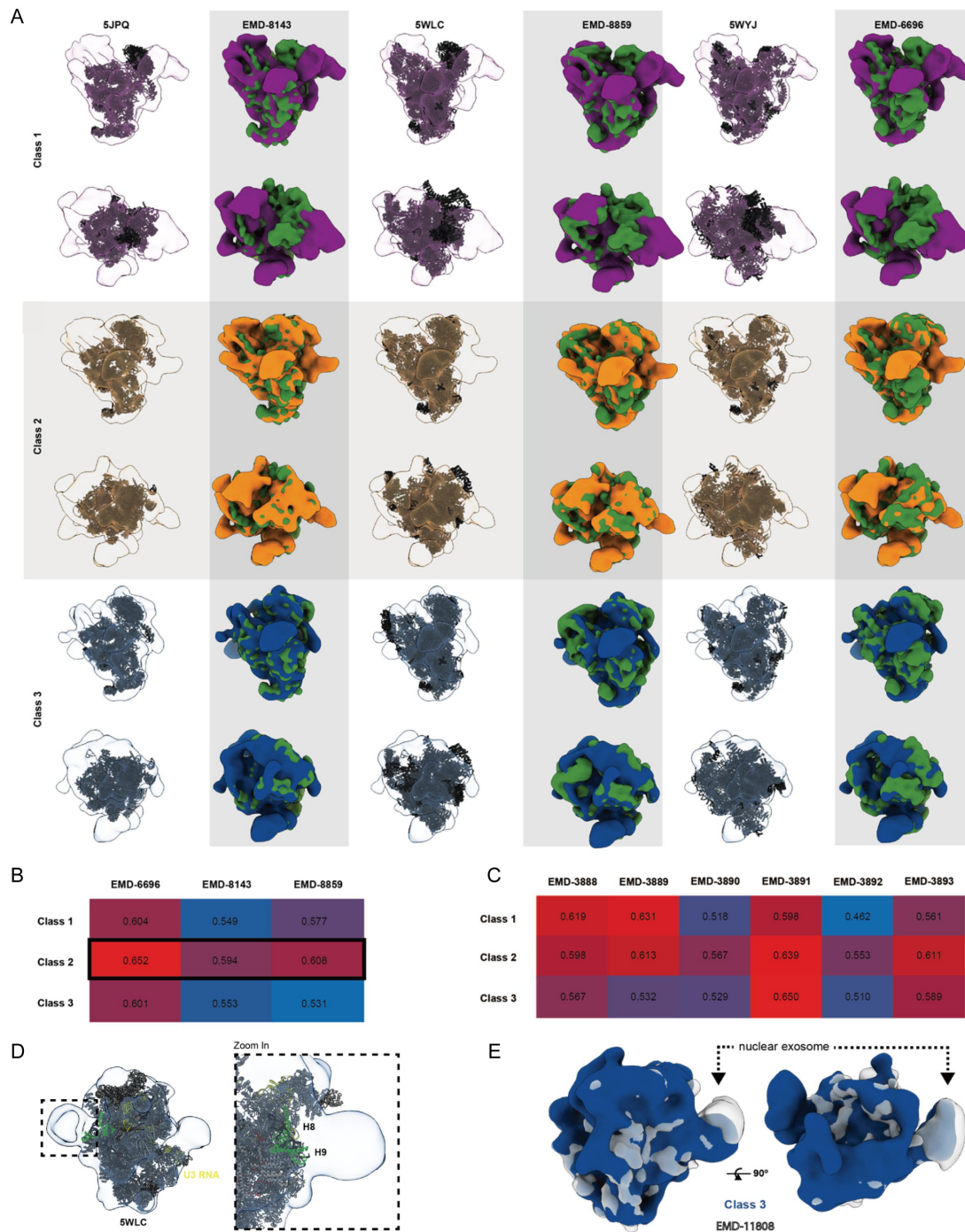


**Figure 20. Structural alignment of *in situ* SSU processome and LSU precursor structures with published PDB molecular models and EM density maps.** (A) Structure fitting of molecular models (5JPQ, 5WLC, and 5WYJ) and EM density maps (EMD-6696, EMD-8143, and EMD-8859) into the *in situ* SSU processome classes. The same procedure was performed for LSU precursor classes with published LSU structures, not shown here. (B) The normalized cross-correlation coefficients between the published EM density maps and the *in situ* SSU processome structures. The larger the number is, the higher the similarity is. (C) The normalized

cross-correlation coefficients between the published EM density maps and the *in situ* LSU precursor structures. (D) The structural fit of 5WLC in SSU processome class 3 identified a prominent density on the H8 and H8 of the 5'ETS RNA, which is enlarged on the right. (E) Structural alignment of SSU processome class 3 with EMD-11808 confirmed the exosome density on class 3.

### 2.3 Discussion

In this project, a reproducible cryo-ET workflow for studying ribosome biogenesis in both *S. cerevisiae* and *C. reinhardtii* was established and *in situ* structures of preribosome particles from both organisms were obtained, which makes a valuable contribution to completing our understanding of this intricate process.

For the cryo-ET study carried out on *S. cerevisiae*, less contrasted tomograms of the nucleus impose difficulties for me to identify the nucleoli. Even with the fluorescence correlation on the nucleus and proper denoising of the tomogram by CryoCare ([Buchholz, Jordan et al. 2019](#)), nucleolar compartments have not been recognized in my study. Additionally, the STA of preribosome-like particles is mainly impeded by the high dynamics of ribosome biogenesis in yeasts. As well, the preribosome-like particles detected in yeast tomograms remain suspicious since my further STA analysis showed that the final averaged structure had a high dependency on the template. To overcome those difficulties, one may need to introduce extracellular stimuli to the yeasts to synchronize the preribosomes and segregate the nucleolar compartments for cryo-ET analysis. Genetic manipulations to interrupt the ribosome biogenesis in yeasts could also be considered to enrich certain preribosomes. More importantly, a better and more precise strategy to perform template matching with fewer artifacts induced to the final result would be welcomed.

In contrary to the cryo-ET study in *S. cerevisiae*, I managed to finish a comprehensive and rigorous cryo-ET study with Dr. Philipp Erdmann on ribosome biogenesis in *C. reinhardtii*, in which we implemented multiple interdisciplinary methods with *in situ* cryo-ET analysis. This enabled us to make the best of the data and obtain unprecedented critical information that's been missing for long in ribosome biogenesis.

First of all, we successfully visualized the unperturbed nucleolar organization in *C. reinhardtii*, which is consistent with the canonical tripartite nucleolar organization observed for higher eukaryotes, validating the authenticity of the model. Second, we successfully identified distinct unperturbed preribosome species in their native environment (**Figure 21 A, B**), which could not be achieved by conventional biochemical methods and SPA, providing valuable information from another level of understanding biogenesis of SSU and LSU.

Moreover, the maturation of SSU processome and LSU precursor and their spatiotemporal arrangement shown in this study are in good agreement with previous SPA studies. But unlike other *in vitro* studies, the *in situ* data of this study provide direct evidence to corroborate the ribosome biogenesis model that was purely established with SPA structures. More interestingly, a gradual compactification of SSU processome from class 1 to class 3 was demonstrated in this study (**Figure 21 C**), providing more genuine information on the conformational transition of SSU processome during ribosome biogenesis. In the model of ribosome biogenesis suggested by this study, SSU processome and LSU precursor particles mature from the nucleolar center to the nuclear envelope and remarkable conformational changes take place on the nucleolar surface where major assemblies of preribosome particles are accomplished.

As introduced previously, formation of nucleolus is a result of LLPS of different nucleolar liquid-phase compartments, but it was not clear whether the compartmentalization is driven by the different preribosome particles during ribosome biogenesis. This question was difficult to address as the nucleolus is a membraneless structure and liquid-phase compartments could be easily lost or irreversibly disrupted by conventional biochemical methods. In this study, the GC, a liquid-phase compartment in the nucleolus was shown to play a critical role in hosting the assembly of preribosome particles since it was found adjacent to the preribosome maturation gradient where distinct preribosome particles were identified and resolved as solid structures (**Figure 21 D**). Moreover, a mass gradient was observed in the nucleolus and the gradient was shown to reach the first peak when SSU processome and LSU precursor became identifiable. This gradient might contribute to the distinct

morphologies of nucleolar compartments, which are inferred to be direct reflections of the variable abundance of different preribosome particles in different nucleolar regions, especially those without a well-resolved structure at the early stage of ribosome biogenesis. Therefore, this work provides the first molecular-level evidence to the prediction that the LLPS organization of the nucleolus is tied to multivalent interactions of the preribosome particles and their assembly state. As preribosome particles mature, interactions with assembly factors are gradually lost and the promiscuity of LLPS decreases accordingly. The boundary of nucleolus is then defined when the nucleolar LLPS ceases with the maturation of preribosome particles. Therefore, a maturation gradient of preribosome particles is expected within the LLPS before those particles depart from the nucleolus. Besides, the spherical distribution of SSU processome and LSU precursor around the nucleolus also suggests a modulating function that LLPS compartments can wield at interfaces. In addition, the exosome-associated SSU processome class identified in this study strongly indicates a pivotal role that LLPS compartments can play in quality control of ribosome biogenesis as a clear departure signal must be sent and received on time to complete the drastic conformational transition from SSU processome to 40S preribosome.

Taken together, my *in situ* cryo-ET study on ribosome biogenesis in *S. cerevisiae* and *C. reinhardtii* builds up a bridge between molecular structural studies and cellular studies on ribosome biogenesis, filling up the knowledge gap in understanding the morphology and function of the liquid-phase nucleolar compartments in this process.

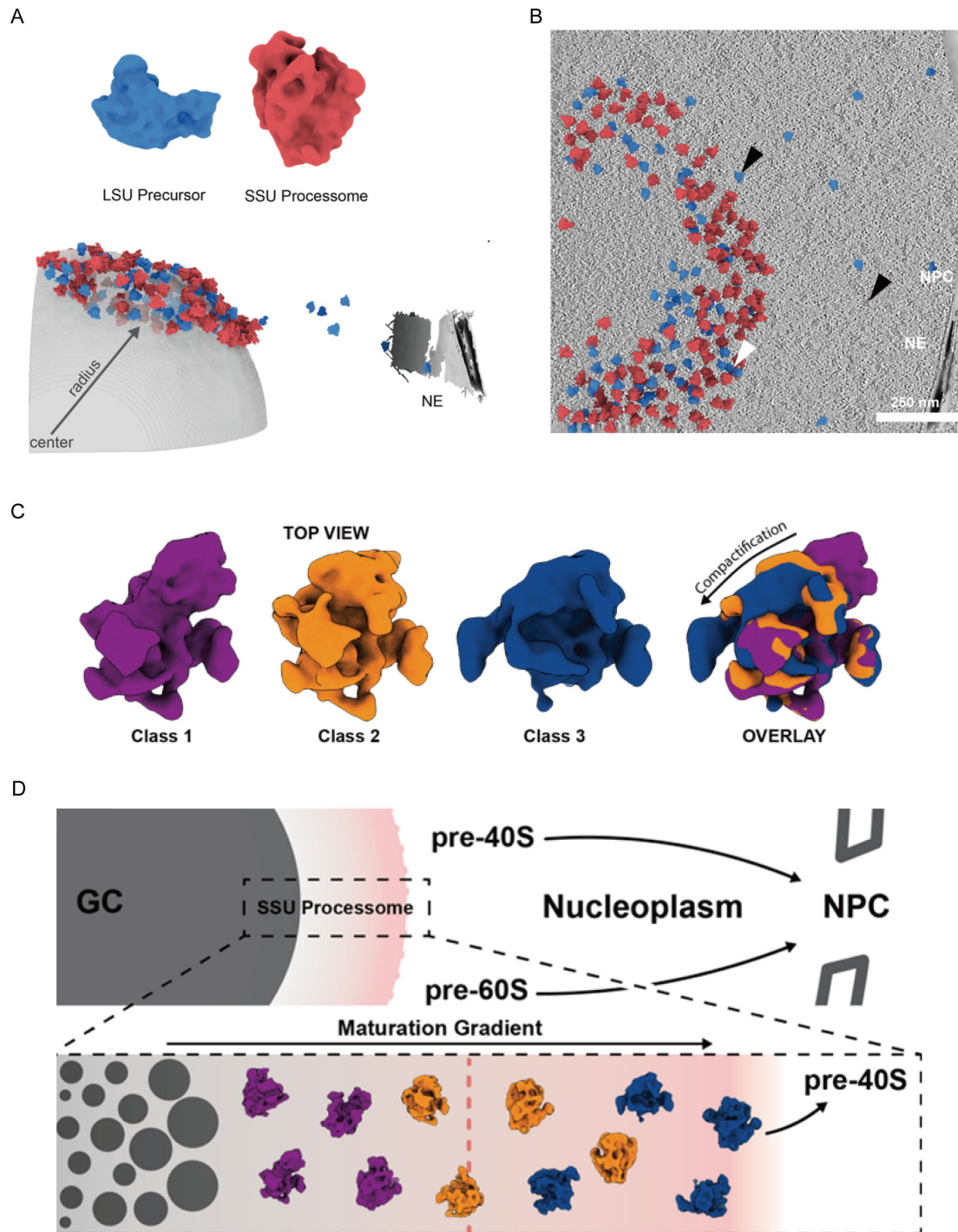


**Figure 21. Summary of the *in situ* study of ribosome biogenesis in *C. reinhardtii*.** (A) 3D demonstration of the spatial organization of LSU precursor and SSU processome in nucleus. The nucleolus is presented as a gray sphere. Nuclear envelope (NE). (B) A representative segmented tomogram with LSU precursor and SSU processome. (C) The compactification of SSU processome from class 1 to class 3. (D) The maturation order of SSU processome classes on the nucleolar surface. Granular component (GC), Nuclear pore complex (NPC).

## 3. Non-stop mRNA Decay Project

### 3.1 Introduction and Aims

This section presents our current knowledge of mRNA surveillance and specifically focuses on non-stop mRNA decay in yeasts. This mechanism is covered in detail with its key components, including the exosome complex, Superkiller protein 7 (Ski7), and the Ski complex. Decent SPA structures of these complexes are presented and remaining challenges are described in terms of critical associations of them. To answer those questions, aims are set accordingly.

#### 3.1.1 mRNA Surveillance

Not only ribosome biogenesis is under strict surveillance, but also multiple processes where mature ribosomes participate in the cytoplasm are strictly regulated. To ensure the development of life, deleterious products made from errors must be corrected or eliminated in time. Most toxic molecules in cells are aberrant proteins rising from gene mutations, incomplete translation, and protein misfolding ([Maniatis and Reed 2002](#)). As the essential intermediates between DNA and proteins, mRNAs are under rigorous surveillance, starting from their synthesis to the final step translation.

The maturation of mRNAs involves transcription, capping, splicing, cleavage, polyadenylation, and export. In each step, errors may occur. Considerable research focused on mRNA surveillance, has been conducted in various organisms over decades, and different mechanisms were discovered in both nucleus and the cytoplasm. In the nucleus, the degradation of aberrant mRNAs is mainly carried out by a multi-protein complex named nuclear exosome, and this process is aided by several cofactors such as TRf4/5-Air1/20-Mtr4 polyadenylation (TRAMP) complex ([Anderson, Phan et al. 2000](#), [Kadaba, Krueger et al. 2004](#), [LaCava, Houseley et al. 2005](#)), decay of mRNA in the nucleus (DRN) complex ([Das, Guo et al. 2000](#)), and Nrd1p/Nab3p/Sen1p (NNS) complex in yeast ([Vasiljeva, Kim et al. 2008](#)), hTRAMP, nuclear exosome targeting (NEXT), and PolyA tail-exosome targeting (PAXT) complexes in human ([Schilders, van Dijk et al. 2007](#), [Lubas, Christensen et al. 2011](#)). In the cytoplasm, there are three

pathways characterized for mRNA surveillance, including nonsense-mediated mRNA decay (NMD), nonstop mRNA decay (NSD), and no-go mRNA decay (NGD) ([Conti and Izaurralde 2005](#), [van Hoof and Wagner 2011](#)). These pathways are highly involved in monitoring the turnover of different types of erroneous mRNAs. As indicated by the name, NMD monitors mRNAs with a premature termination codon, which are then regarded as nonsense mRNAs; NSD is featured at degrading mRNAs without a stop codon; while NGD is involved in removing ribosome-stalling mRNAs, for instance mRNAs with a strong secondary structure ([van Hoof and Wagner 2011](#)). In addition, when ribosome-associated quality control (RQC) is triggered, mRNAs can also be degraded by the 5'-to-3' exoribonuclease Xrn1 in the 5' to 3' direction ([Stevens and Maupin 1987](#)) after the decapping and by the exosome complex in the 3' to 5' direction ([Anderson and Parker 1998](#)) after the deadenylation. Based on previous clinical researches, the dysfunction of the abovementioned mRNA surveillance pathways has been reported to play a critical role in a wide range of diseases such as cancer, X-chromosome-linked mental retardation, Parkinson's disease, and scleroderma ([Singh, Saha et al. 2018](#)).

### 3.1.2 Nonstop mRNA Decay in *S. cerevisiae*

Nonstop mRNA decay, as introduced previously, is a mRNA surveillance mechanism designated to degrade aberrant mRNAs without a stop codon in the cytoplasm ([Vasudevan, Peltz et al. 2002](#)). It is commonly believed that this surveillance mechanism starts when the ribosome reaches the far 3' end of a nonstop mRNA during translation ([Vasudevan, Peltz et al. 2002](#)). Usually, when a stop codon (UAG, UAA, or UGA) enters the empty A-site of the ribosome, termination of translation occurs. In eukaryotes, this process is mainly mediated by two release factors, eukaryotic peptide chain release factor subunit 1 (eRF1) and eRF3. eRF1 and eRF3 form a complex with GTP and eRF1 is responsible for recognizing the stop codon. After the recognition, the nascent-peptide chain is then released upon the hydrolysis of GTP by eRF3, followed by the splitting of the ribosome into LSU and SSU ([Frolova, Le Goff et al. 1996](#), [Cheng, Saito et al. 2009](#)).

However, it is known that ribosomes translating a NSD transcript cannot be split due to the absence of a proper stop codon, which therefore stalls them at the 3' end. In yeasts, this is presumed to be a transient process where several cofactors, including Ski7, the Ski complex (Ski2-Ski3-Ski8), and the cytoplasmic exosome complex are subsequently recruited to rescue the ribosome and degrade the NSD transcript, followed by the proteolysis of the nascent-peptide chain ([Anderson and Parker 1998](#), [Brown, Bai et al. 2000](#), [Araki, Takahashi et al. 2001](#), [van Hoof, Frischmeyer et al. 2002](#)) (**Figure 22**).

NSD was first described in 1989 by Herrick and Jacobson when the yeast nuclear factor-kappa-B activator 1 (ACT1) mRNA lacking an in-frame stop codon showed a much shorter half-life than the normal one ([Herrick 1989](#)). And after that, yeast phosphoglycerate kinase 1 (PGK1) mRNA was modified and verified by Roy Parker as a canonical reporter for studying the mechanism of NSD ([Frischmeyer, van Hoof et al. 2002](#), [van Hoof, Frischmeyer et al. 2002](#)). Subsequent studies have revealed that NSD requires the exosome complex for the final shredding of the aberrant mRNA, but this process is distinct from the exosome-mediated decay of normal mRNAs as described previously, as it does not depend on the deadenylation of the 3' poly-A tail ([Meaux and Van Hoof 2006](#)). In yeasts, NSD is highly dependent on the Ski complex and Ski7 that are not necessary for normal mRNA decay. The deletion of Ski7 is not lethal but it significantly impairs NSD ([Anderson and Parker 1998](#), [Brown, Bai et al. 2000](#), [van Hoof, Staples et al. 2000](#)). On the other hand, disrupting NSD and Xrn1-mediated 5'-to-3' mRNA degradation at the same time is lethal to the yeast ([Johnson and Kolodner 1995](#), [Araki, Takahashi et al. 2001](#)).

In yeasts NGD, Dom34 and Hbs1 that share a high conformational similarity with eRF1 and eRF3 ([Doma and Parker 2006](#)) are first recruited to the empty A-site of the stalled ribosome, followed by the GTP hydrolysis mediated by Hbs1. Hbs1 and Pelota (homolog of Dom34) have been reported to function in mammalian NSD ([Saito, Hosoda et al. 2013](#)). In yeast NSD, Ski7, a paralogue of Hbs1, is speculated to recognize the stalled ribosome because its C-terminus possesses a translational GTPase-like structure that is presented in eEF1 $\alpha$  and eRF3 ([van Hoof, Frischmeyer et al. 2002](#)). However, Ski7 does not form any heterodimer with other proteins and it does not

contain a conserved His site that is essential for other ribosome-associated GTPases to conduct GTP hydrolysis ([Salas-Marco and Bedwell 2004](#), [Shoemaker, Eyler et al. 2010](#)). Therefore, whether Ski7 is responsible for the recognition of stalled ribosomes in yeast NSD remains elusive. Alternatively, recent studies indicate that site-specific ubiquitination that results from a unique surface created by collided ribosomes may be a prerequisite for the initial recognition of stalled ribosomes ([Matsuo, Ikeuchi et al. 2017](#), [Juszkiewicz, Chandrasekaran et al. 2018](#), [Ikeuchi, Tesina et al. 2019](#)).

Following the recognition of stalled ribosomes, the Ski complex has been shown to interact with the ribosome directly and thread the 3' end of mRNA out to the helicase channel of Ski2. This implies a concerted NSD process where the NSD mRNA is dragged out by the Ski complex from stalled ribosomes to the exosome complex for a complete degradation ([Schmidt, Kowalinski et al. 2016](#)). However, this model may not be the only one where the Ski complex can thread the mRNA from ribosomes to exosomes since there have been studies indicating that the Ski complex can still assist the cytoplasmic exosome without the presence of ribosomes ([Zhang, Khanna et al. 2019](#), [Zinoviev, Ayupov et al. 2020](#)).

Taken together, recent X-ray crystallography and SPA work has significantly advanced our understanding of the mechanism of NSD, structural detail of key complexes are well resolved, indicating conceivable dynamics of this process. However, as a tightly controlled mRNA surveillance mechanism, there is still critical information missing in NSD, such as the recognition of stalled ribosomes, the subcellular location of NSD, the timing of each interaction, and its relationship with other cellular machinery.

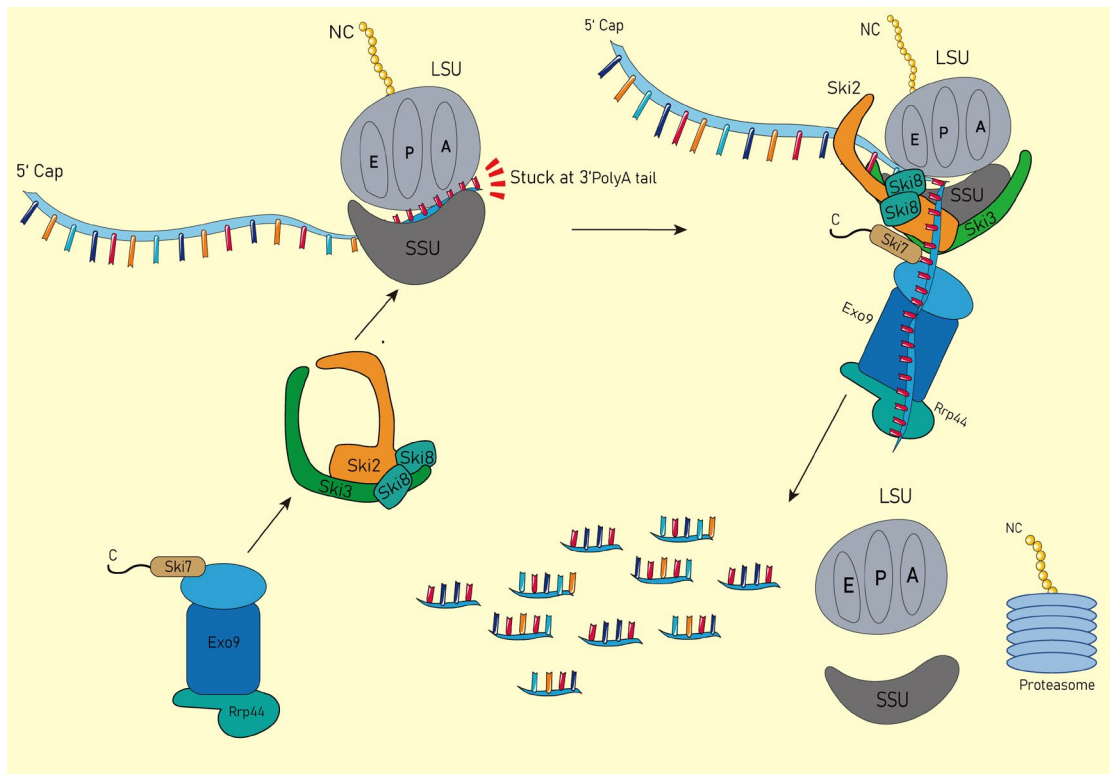


**Figure 22. Schematic overview of nonstop mRNA decay in yeasts.** Stalled ribosomes at the far 3' end of mRNAs lacking a stop codon trigger a distress signal that recruits the Ski complex to the SSU, and the interaction sequentially causes a conformational change to Ski2, abolishing its auto-inhibition. After that, the cytoplasmic exosome complex is recruited to the Ski complex together with Ski7, serving as a bridging factor. Eventually, the mRNA is threaded by Ski2 into the exosome complex's catalytic core (Rrp44) and gets shredded. This process is coupled with the spitting of ribosomal subunits and the degradation of nascent-peptide chains (NC) by the proteasome. Meanwhile, the Ski complex and cytoplasmic exosome complex are recycled.

### 3.1.3 The Exosome Complex and Ski7 of *S. cerevisiae*

In yeast, the exosome complex was first described as having a role in 3'-to-5' mRNA degradation in Tollervey's lab in 1997 ([Mitchell, Petfalski et al. 1997](#)). At that time, the exosome complex was found essential for the 5.8S rRNA processing, which is now recognized as a nuclear exosome complex ([Allmang, Kufel et al. 1999](#), [Chekanova, Gregory et al. 2007](#)). Following studies have shown that the exosome complex exists in the cytoplasm as well for the quality control of mRNAs, and that is then defined as

the cytoplasmic exosome complex ([Anderson and Parker 1998](#), [Araki, Takahashi et al. 2001](#), [Gudipati, Xu et al. 2012](#)).

There is a slight difference in the components between the nuclear exosome complex and the cytoplasmic exosome complex in yeasts. The core components including Csl4, Rrp4, Rrp40, Rrp41, Rrp46, Mtr3, Rrp42, Rrp43, Rrp45, and Rrp44/Dis3, which are described as Exo10, remain the same ([Liu, Greimann et al. 2006](#), [Makino, Schuch et al. 2015](#)) (**Figure 23 A**). In the nucleus, Exo10 associates with extra proteins, namely Rrp6-Rrp47, Mtr4, and Mpp6, forming a complex named Exo14 ([Butler and Mitchell 2010](#), [Schuch, Feigenbutz et al. 2014](#)). While in the cytoplasm, Exo10 associates with the Ski complex and a bridging factor Ski7 which is also speculated to be a constitutive part of the yeast cytoplasmic exosome complex ([Anderson and Parker 1998](#), [Dziembowski, Lorentzen et al. 2007](#), [Kowalinski, Kögel et al. 2016](#)) (**Figure 23 B**). From the catalytic analysis, the nine-subunit core Exo9 of the exosome complex from which Rrp44/Dis3 is subtracted has been shown to be incapable of conducting the 3'-to-5' exoribonucleolytic activity, thus the catalytic activity of Exo10 is solely contributed by Rrp44/Dis3 ([Dziembowski, Lorentzen et al. 2007](#)). Whereas in the nuclear Exo14, Rrp6 provides extra distributive 3'-to-5' exoribonucleolytic activity and Mtr4 serves as a helicase ([Briggs, Burkard et al. 1998](#), [Schuch, Feigenbutz et al. 2014](#), [Wasmuth, Januszyk et al. 2014](#)).

The yeast Exo9 shares an overall conformational similarity with that of archaea, forming a barrel-like structure where a RNase PH-like ring composed of Mtr3, Rrp41, Rrp42, Rrp43, Rrp45, and Rrp46) is capped by a ring formed by Csl4, Rrp4, and Rrp40. Since all the three proteins contain a S1 RNA binding domain and Rrp4 and Rr40 have a K-homology domain, the cap is also called the S1/KH cap ([Lorentzen, Dziembowski et al. 2007](#)). The structure of Exo9 provides a noncatalytic channel where RNAs can be well accommodated, and the variable inner surface of the channel is believed to be critical for the purposeful degradation of specific RNAs ([Liu, Greimann et al. 2006](#)). Rrp44/Dis3 sits on the surface of the PH-like ring opposite to the surface interacting with the S1/KH cap ([Bonneau, Basquin et al. 2009](#), [Drazkowska, Tomecki et al. 2013](#), [Liu, Bratkowski et al. 2014](#)). The PIN (PilT N-terminus) domain of Rrp44/Dis3, which

interacts directly with the PH-like ring, stays stable. While the exoribonuclease module adopts a direct-access conformation when it binds a short RNA of fewer than 14 nucleotides and shifts to a through-channel conformation when a longer RNA is present ([Makino, Schuch et al. 2015](#), [Schuller, Falk et al. 2018](#)). The conformational change of Rrp44/Dis3 upon processing different RNAs reflects a dynamic and selective modulating mechanism for the processing activity of the exosome, and it is associated with the interaction between Exo9 Rrp44/Dis3 ([Drazkowska, Tomecki et al. 2013](#)).

Apart from the Rrp44/Dis3, Rrp6 also works as a catalytic module for the nuclear exosome complex. Previous structural studies have shown that Rrp6 can accommodate the 3' end of RNAs for digestion while the 5' end is deflected from the central channel by the S1/KH cap to the HRDC (helicase and RNaseD C-terminal) domain of Rrp6. Rrp6 has two conformations: the open conformation and the closed conformation. The open conformation is presented when Mtr4 binds to Rrp4 while the closed conformation is found in the absence of Mtr4 ([Schuch, Feigenbutz et al. 2014](#), [Wasmuth, Januszyk et al. 2014](#), [Makino, Schuch et al. 2015](#), [Mukherjee, Gardin et al. 2016](#)) (**Figure 23 C**). However, the exact function of Rrp6 remains elusive since different studies have suggested various roles it may have in nuclear exosome-mediated RNA processing. Some studies point out that Rrp6 plays a passive role in the Rrp44/Dis3-mediated RNA trimming ([Makino, Schuch et al. 2015](#)), while in other studies, it also has been reported to enhance the Rrp44/Dis3 activity ([Mukherjee, Gardin et al. 2016](#)).

Yeast super killer proteins were initially identified as proteins, the null mutation of which gives rise to the superkiller phenotype of increased accumulation of viral double-stranded RNA (dsRNA) ([Toh, Guerry et al. 1978](#), [Toh and Wickner 1980](#), [Ridley, Sommer et al. 1984](#)). Yeast Ski7 serves as a bridging factor connecting the cytoplasmic exosome complex to the Ski complex through its N-terminus. The structure of its C-terminus resembles an active translational GTPase Hbs1, thus its C-terminus is hypothesized to be responsible for its binding to the ribosome ([van Hoof, Staples et al. 2000](#), [Araki, Takahashi et al. 2001](#), [Wang, Lewis et al. 2005](#)) (**Figure 23 D**).

However, there is no detailed structure available for a ribosome-Ski7 complex. The N-terminus contains a region that binds to the exosome and another region that binds to the Ski complex. Previous studies have shown that the N-terminus of Ski7 binds to Exo10 via the surfaces that have been reported for the binding of Rrp6 to the nuclear exosome complex ([Liu, Niu et al. 2016](#)), which then brings the speculation that Ski7 is a constitutive part of the cytoplasmic exosome complex ([Kowalinski, Kögel et al. 2016](#)).

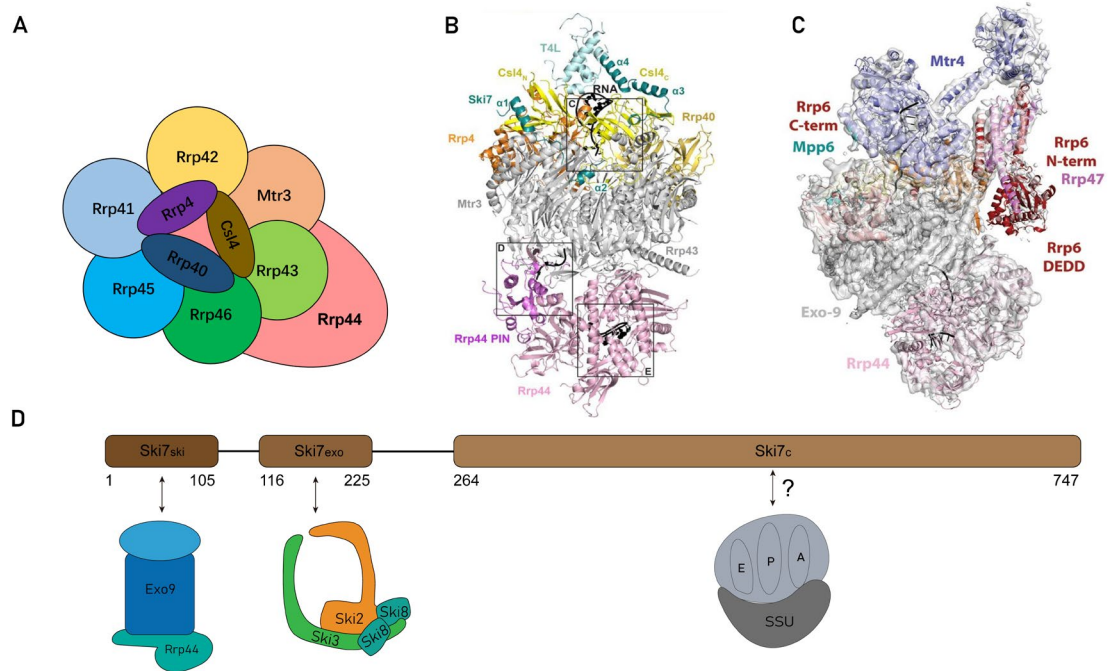


**Figure 23. Overview of yeast exosome complex and Ski7.** (A) The domain schematic of Ski7. The N-terminal region of Ski7 can be characterized into two domains (Ski7<sub>ski</sub> and Ski7<sub>exo</sub>) responsible for the interaction with the Ski complex and the exosome complex, respectively. And the C-terminal region of Ski7 shares a high similarity with GTPases, which makes it plausible that this domain is to bind to ribosomes in NSD. (B) Schematic depiction of the Exo10, in which Rrp4, Rrp40, and Csl4 form an S1/KH ring sitting on the bigger RNase PH ring formed by Mtr3, Rrp41, Rrp42, Rrp43, Rrp45, and Rrp46 pedestalled by Rrp44. (C) The crystal structure of the cytoplasmic exosome: Exo10 with Ski7<sub>exo</sub>. Rrp4, Rrp40, and Csl4 are colored yellowish, while the RNase PH ring is in gray and Rrp44 is colored in pink. Ski7<sub>exo</sub> is in presented in green. Adapted from Kowalinski et al., 2016 (D) The EM structure of the nuclear exosome: Exo10 with Rrp6-Rrp47, Mtr4, and Mpp6. Rrp44 is colored in light pink and Exo9 is in gray,

Rrp6 and Rrp47 are shown in brown and pink, respectively, while Mtr4 is in light purple. Adapted from Schuller et al., 2018.

### 3.1.4 The Ski2-Ski3-Ski8 Complex of *S. cerevisiae*

In yeast, the Ski2-Ski3-Ski8 complex, also called the Ski complex, is a helicase complex consisting of one copy of Ski2, the helicase, one copy of Ski3, the scaffold protein, and two copies of Ski8, the  $\beta$ -propeller protein ([Brown, Bai et al. 2000](#), [Synowsky and Heck 2008](#), [Halbach, Reichelt et al. 2013](#), [Schmidt, Kowalinski et al. 2016](#)). It plays a pivotal role with the cytoplasmic exosome complex in NSD and NMD where the Ski complex is believed to wield the helicase power of Ski2 to thread the mRNA from the ribosome to the exosome ([Schmidt, Kowalinski et al. 2016](#), [Zinoviev, Ayupov et al. 2020](#)). The Ski complex was firstly reported functioning in the 3'-5' mRNA degradation in 1998 in Roy Parker's lab ([Anderson and Parker 1998](#)). The deletion of any subunit of the Ski complex in yeast results in synthetic lethality when the 5'-to-3' exoribonuclease Xrn1 is deleted simultaneously ([Anderson and Parker 1998](#), [Araki, Takahashi et al. 2001](#)). Ski2 is a DExH-box helicase that shares an overall structural similarity with Mtr4 that functions as a helicase assisting the nuclear exosome complex, and Ski2 is a multidomain protein containing an N-terminal region and a helicase core followed by a flexible insertion domain ([Halbach, Rode et al. 2012](#), [Halbach, Reichelt et al. 2013](#), [Schmidt, Kowalinski et al. 2016](#)). The N-terminal region of Ski2 is crucial for its interaction with Ski3 and Ski8, while the helicase core is a typical RNA-dependent ATPase of the DExH family and the insertion domain is responsible for its binding to RNAs ([Wang, Lewis et al. 2005](#)). Ski3 is a tetratricopeptide repeats (TPRs) containing protein, and it forms a scaffold for the Ski complex where its N-terminus is stretched out to the solution while the C-terminus accommodates Ski2 and Ski8 ([D'Andrea and Regan 2003](#), [Halbach, Reichelt et al. 2013](#)). Ski8 is formed by seven WD40 repeats, and the two copies of it in the Ski complex function differently as the outer one doesn't affect the structural integrity of the complex while the inner one does ([Stirnemann, Petsalaki et al. 2010](#), [Halbach, Reichelt et al. 2013](#)) (**Figure 24 A**). Moreover, the outer Ski8 has an essential role in regulating Ski2 when binding to RNAs.

Interestingly, the ATPase and helicase activity of Ski2 is down-regulated when it is associated with Ski3 and Ski8, which indicates that although Ski2 is the only catalytic component of the Ski complex, the modulation by Ski3 and Ski8 is indispensable for its function in exosome-mediated mRNA decays ([Wang, Lewis et al. 2005](#), [Halbach, Reichelt et al. 2013](#)). Recent studies have shown that the Ski complex directly interacts with the translating ribosome with mRNA 3' overhang threaded from the SSU to the helicase channel of Ski2 ([Schmidt, Kowalinski et al. 2016](#)). Moreover, the autoinhibitory domain of Ski2 undergoes a conformational change upon the ribosome binding, which rationalizes that exosome-mediated mRNA decays are co-translational processes where the association of ribosomes is important ([Schmidt, Kowalinski et al. 2016](#), [Zinoviev, Ayupov et al. 2020](#)) (**Figure 24 B**). However, it has also been demonstrated that the Ski complex with Ska1 can also facilitate the exosome-mediated degradation of long 3'UTR-containing RNAs without a close association with ribosomes ([Zhang, Khanna et al. 2019](#)). This implies a more extensive role of Ski complex in mRNA turnover.

Based on the abovementioned studies, the Ski complex plays a crucial role in recognizing and extracting the target mRNA with a 3' overhang from the ribosome, forming a ribosome-Ski complex. Together with the exosome-Ski7 complex, a model where the ribosome-Ski complex initiates the NSD and then recruits the exosome-Ski7 complex to shred mRNA can be speculated. However, there is no direct structural information on such a super complex that contains the ribosome-Ski complex and the exosome-Ski7 complex. This missing information is indispensable for us to complete the whole picture of NSD. Apart from that, potential structural damage by biochemical isolation and over-manipulation in previous studies are also concerning since they might induce unwanted artifacts to the structures and harm the integrity of the genuine NSD-related complexes.

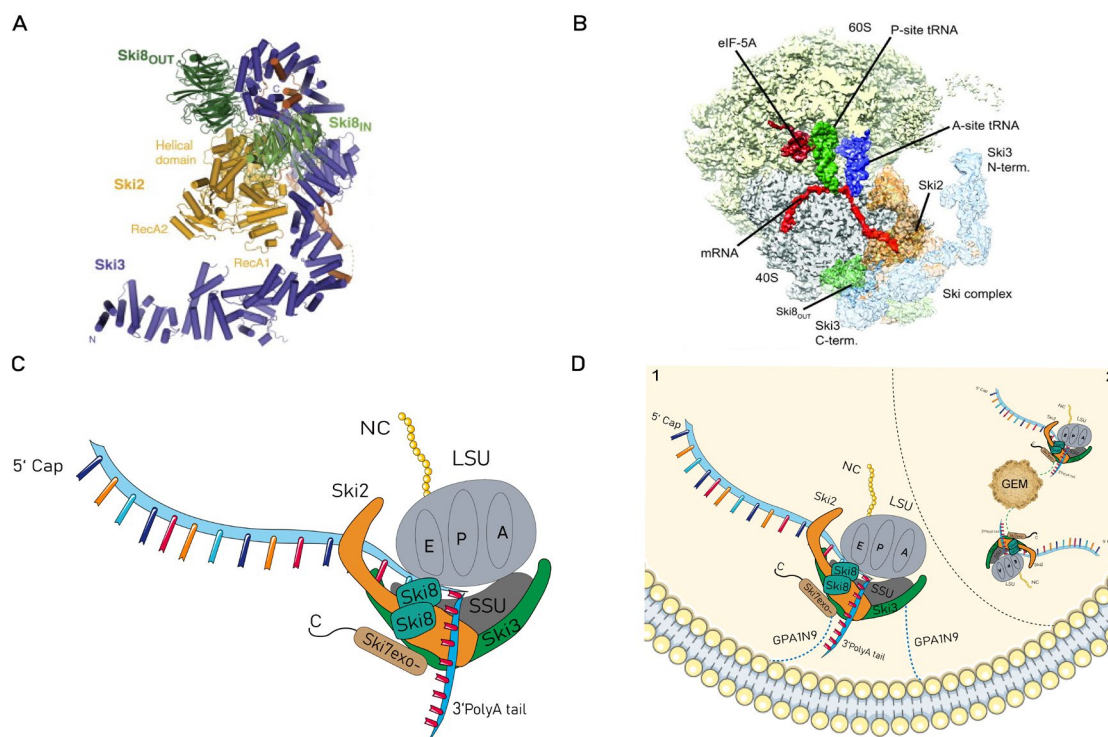


**Figure 24. Structural overview of the yeast Ski complex and project hypotheses.** (A) The crystal structure of the yeast Ski complex in which the insertion domain of Ski2 is mutated. Ski2 is colored in yellow and orange, and Ski3 is colored in blue. Two copies of Ski8 are shown in green (Ski8<sub>in</sub> in light green while Ski8<sub>out</sub> in dark green). Adapted from Halbach et al., 2013. (B) The EM structure of the yeast Ski complex docking on SSU of the ribosome. LSU is depicted in light yellow, and SSU is depicted in silver gray with P-site tRNA and A-site tRNA colored in green and blue, respectively. mRNA is colored in red, and Ski2 is shown in orange, Ski8<sub>out</sub> is in green, while Ski8<sub>in</sub> is in light green. Ski3 is depicted in light blue overall and additionally eIF-5A is colored in dark red. Adapted from Schmidt et al., 2016. (C) Hypothesized cartoon model of the Ski complex with a stalled ribosome in the cell when NSD is induced. Ski7 is mutated in the exosome-binding domain and colored in red (Ski7<sub>exo-</sub>). The Ski complex adopts an open conformation with mRNA threaded through the helicase channel of Ski2. (D) Depiction of the hypothesized subcellular localizations of the Ski complex with stalled ribosomes in two situations. In scenario 1, Ski7<sub>exo-</sub> and Ski3 are genetically fused with the plasma membrane signal peptide GPA1N9. In scenario 2, Ski7<sub>exo-</sub> is genetically fused with GEM40/20.

### 3.1.5 Aims of the NSD Project

To address abovementioned questions, below are the objectives that I aim to achieve:

1. To enrich stalled ribosomes by overexpressing the NSD reporters in NSD-defective yeasts.
2. To establish a reproducible cryo-ET workflow for *in situ* analysis of NSD in yeasts.
3. To identify stalled ribosomes with the Ski complex attached (**Figure 24 B, C**).
4. To resolve the *in situ* structure of Ski-complex-associated ribosomes and compare it to SPA structure (**Figure 24 B**).
5. To map Ski-complex-associated ribosomes back into the tomograms and then examine their cellular localization and biological relevance with other cellular components.
6. In case of inadequate Ski-complex-associated ribosomes for STA, to perform the subcellular localization of NSD-related protein complexes for the enrichment of NSD at specific subcellular structure (Plasma membrane and GEM40/20) ([Gillen, Pausch et al. 1998](#), [Delarue, Brittingham et al. 2018](#)) (**Figure 24 D**).

## 3.2 Results

This section covers major results from the NSD project. Both conventional biochemical experiments and *in situ* analysis by cryo-ET were performed to characterize this tightly controlled ribosome-associated mRNA surveillance process, including establishing a reliable system to introduce NSD, deciphering the *in situ* structure of ribosomes, and developing novel strategies to enrich target protein complexes.

### 3.2.1 Impairment of NSD

To impair NSD in yeasts, I in collaboration with Dr. Nicole Eisele and Achim Keidel conducted mutagenesis of one crucial gene, *SKI7*, which is specifically involved in yeast NSD. Several corresponding NSD-defective strains with a genetic background of *hbs1Δ ski7Δ* for subsequent cryo-ET studies were generated and verified. In parallel, NSD-defective yeast strains were transformed with a canonical NSD reporter PGK1-nonstop which was constructed in a galactose-inducible plasmid to increase the

occurrence of NSD in yeasts, making the expression of PGK1-nonstop controllable with the induction of galactose (**Figure 25**).

Based on the structure of Ski7, we generated strains with the Ski7 truncated either at the N-terminus or the C-terminus, and the Ski7 mutated in the exosome-binding domain. After the induction of 2% galactose, the NSD reporters started accumulating significantly over time in the NSD mutant compared to the wild type, and this was measured by detecting the FLAG tag on PGK1-nonstop through western blot (**Figure 26 A, B**). Therefore, this result indicates that NSD can be sufficiently impaired by mutating Ski7. In addition, we performed ribosome profiling in wild-type and *hbs1Δ ski7Δ* yeasts and the data showed that undegraded NSD reporters only migrated together with 80S ribosomes (**Figure 26 C, D**), indicating that some 80S ribosomes stall with the nascent-peptide chain of PGK1-nonstop upon the impairment of NSD.

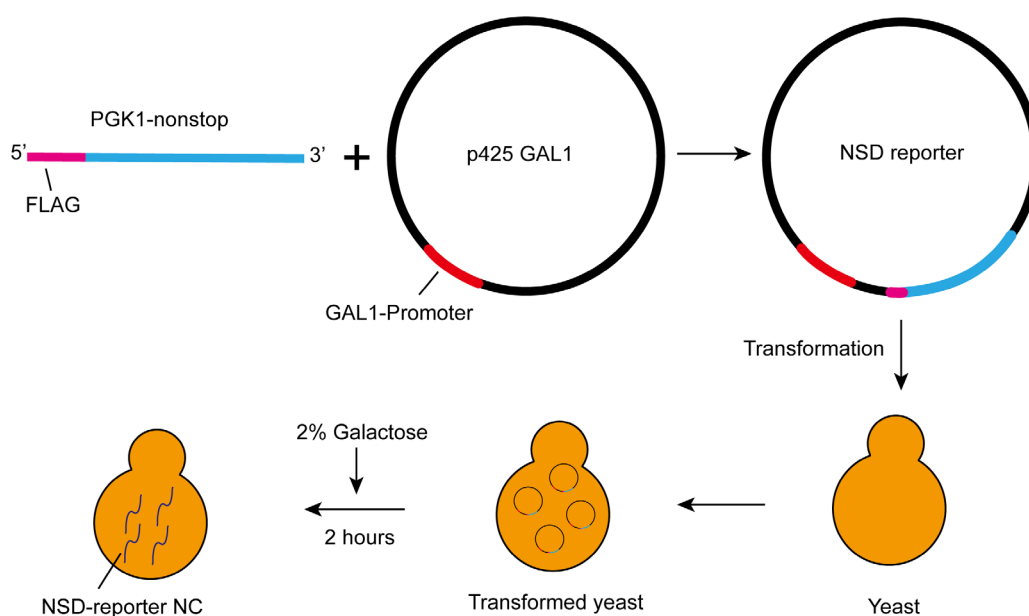


**Figure 25. Schematic illustration of NSD-induction by galactose in yeasts.** PGK1-nonstop was constructed into yeast plasmid p425 GAL1 under the regulation of GAL1 promoter. A FLAG tag was introduced on the 5' end. Yeasts were then transformed with such fused plasmids. Transformed yeasts did not produce any NSD-reporter nascent peptide chain (NC) until galactose was added to the medium with a final concentration of 2%. After 2 hours of incubation, significant expression of NSD-reporter NC could be detected.

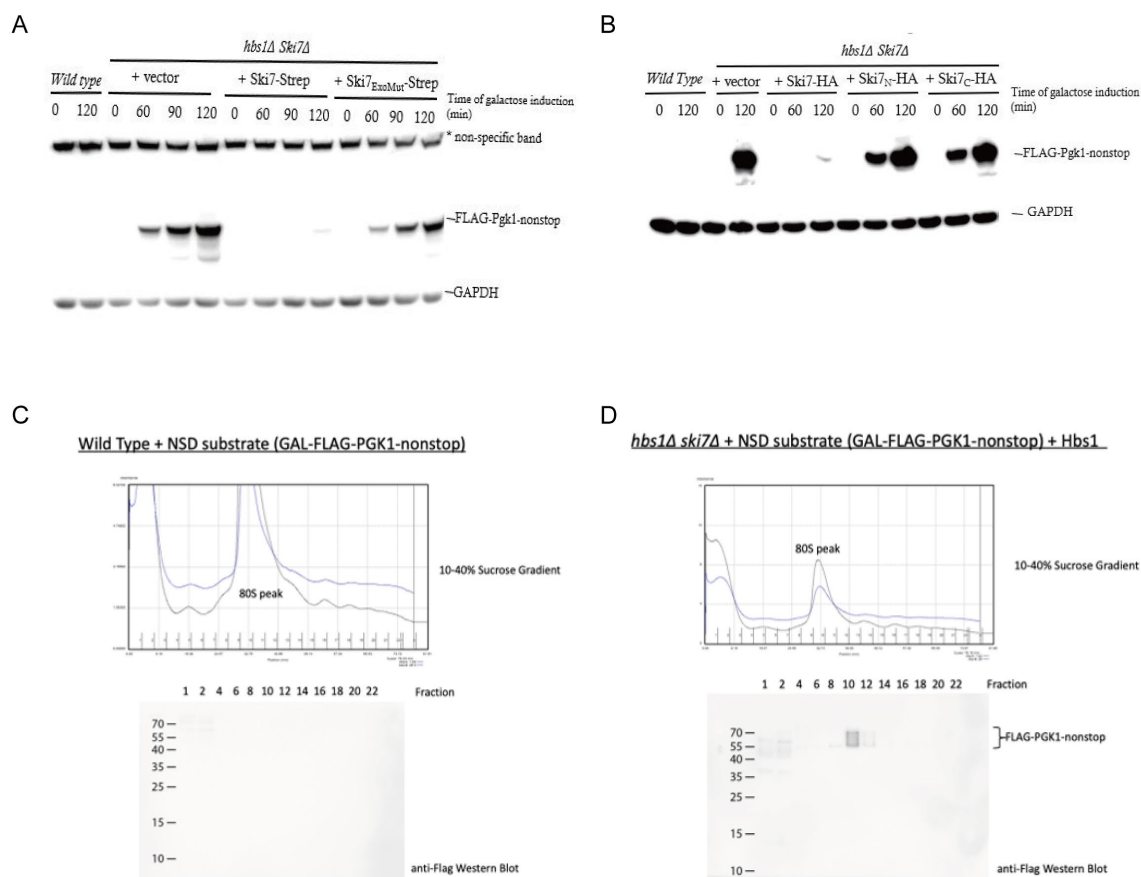


**Figure 26. Assessment of impairment of NSD.** (A), (B) Western blot of NSD reporter PGK1-nonstop in *hbs1Δ ski7Δ* yeasts. PGK1-nonstop accumulates over time in *hbs1Δ ski7Δ* yeasts expressing mutated Ski7 (Ski7<sup>ExoMut</sup>-) and truncated Ski7 (Ski7<sup>N</sup>- and Ski7<sup>C</sup>-) but not in yeasts expressing wild type Ski7. Yeasts were harvested after 0, 60, 90, 120, and 150 minutes of galactose induction and immediately subjected to lysis for western blot. \* Non-specific band doesn't intervene in the results. (C), (D) The profiling of ribosomes in wild type and *hbs1Δ ski7Δ* yeasts after the galactose induction, followed by the anti-FLAG western blot. Ribosomes were profiled by sucrose gradient fractionation. PGK1-nonstop could be seen migrating with 80S ribosome only.

### 3.2.2 Tomograms of NSD-defective Yeast Cells

To characterize the ribosomes stalling with the nascent-peptide chain of PGK1-nonstop, I prepared yeast lamellae from all NSD-defective yeast strains ( $Ski7^{ExoMut^-}$ ,  $Ski7^C^-$ , and  $Ski7^N^-$ ) after 2 hours of galactose induction.

To prepare the grids, yeast cells were cultured until the  $OD_{600}$  reached above 0.6 and then 2% galactose was added to each strain, followed by another 2-hour culture. Then cells were plunged on holey carbon R2/1 copper grids. Next, lamellae were made without any correlation. Lamellae were checked by SEM at 5kV/3kV for a rough estimation of thickness. The less the overcharging is, represented by a white reflection on the lamella, the thinner the lamella is. White reflections result from the charging during the passing of electrons through the thick region of lamellae (**Figure 27 A**). The average thickness of my lamellae is around 130 nm and some good ones can reach below 70 nm, which comes from the calculation based on reconstructed tomograms and is the ideal thickness for cryo-ET. To avoid the bending problem that often happens to thin lamellae, the width of lamellae was maintained at around 10  $\mu$ m and two trenches were made flanking the lamella. After that, lamellae were transferred to the TEM and the magnification was set to 42k for the recording (**Figure 27 B**).

Tomograms were taken mainly on the cytosol areas of yeast cells to include as many ribosomes as possible, and tomograms were reconstructed using IMOD without any denoising. From the reconstructed tomograms, apart from ribosomes, multiple cellular components could also be clearly identified, including ER, the mitochondrion, the cell wall, and the nucleus (**Figure 28**). No significant difference could be detected between the wild type and NSD-defective yeasts in terms of the morphology. Thus, further analyses were performed.

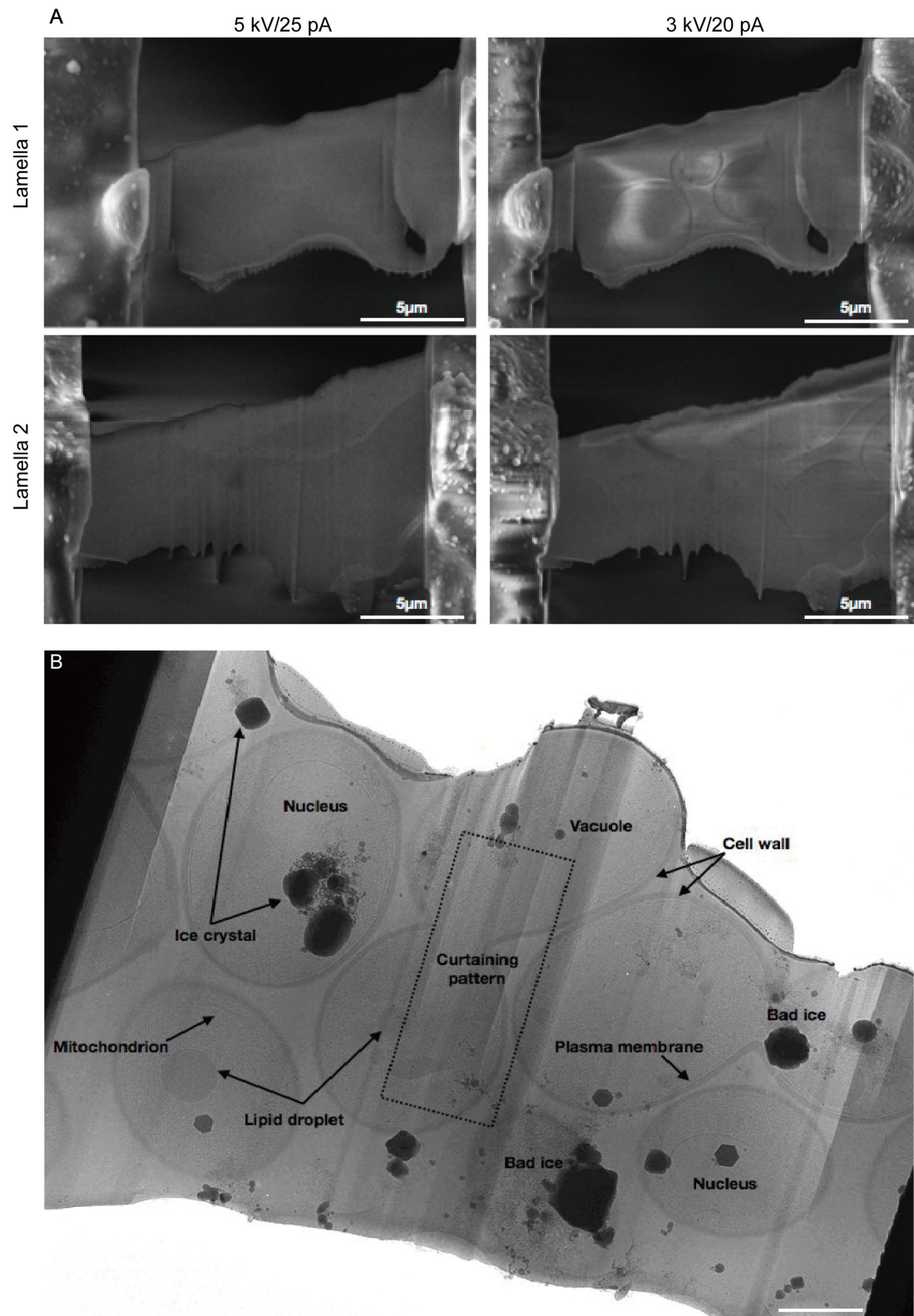


**Figure 27. Lamellae of yeasts.** (A) SEM overviews of two yeast lamellae at the magnification of 10,000x with current 3kV/5kV checking the charging extent. (B) TEM overview of the yeast lamella at the magnification of 3000x, features are labeled accordingly. Scale bar = 1  $\mu$ m.

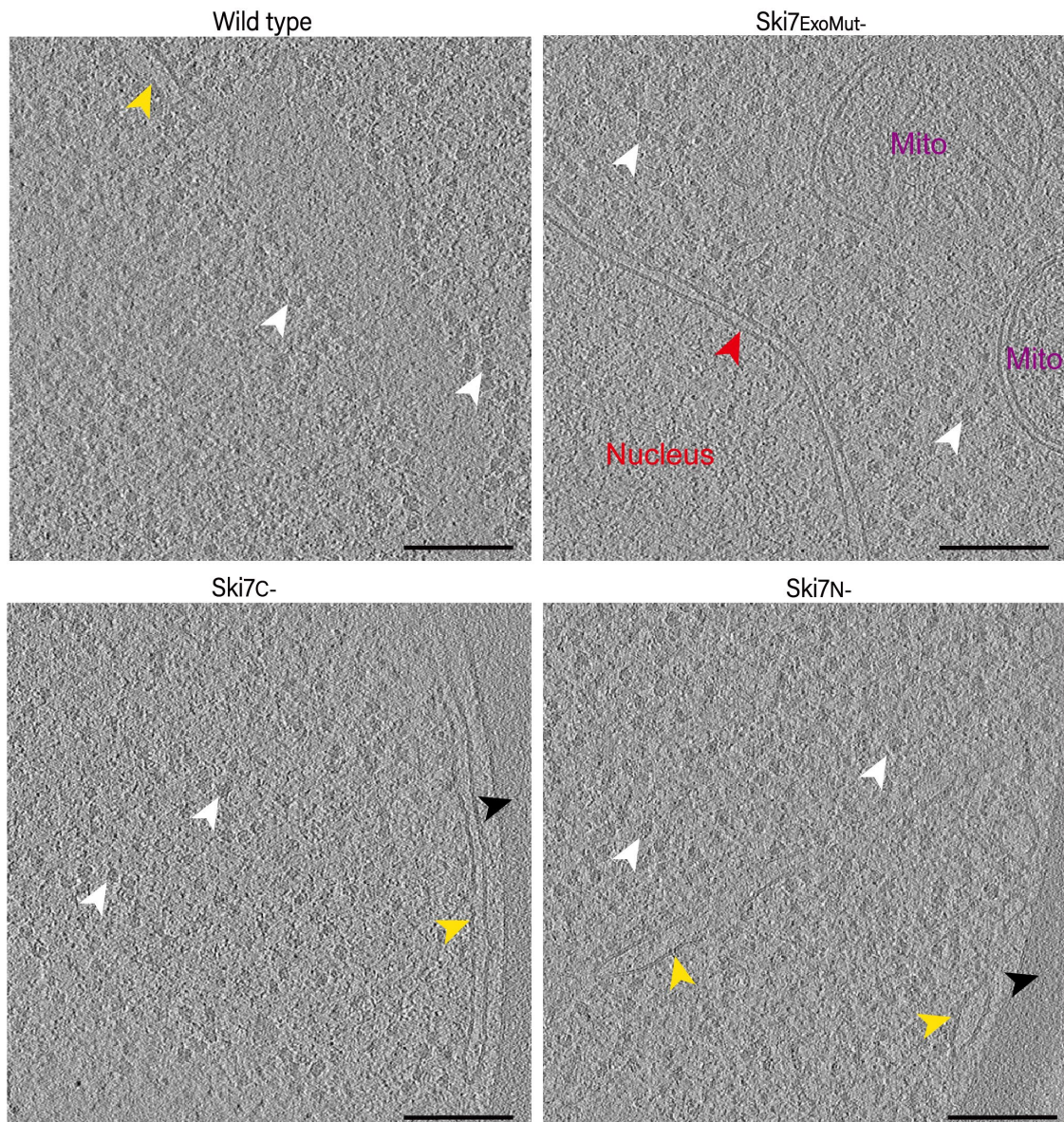


**Figure 28. Reconstructed tomograms of wild type and NSD-defective yeasts.** Four representative slices of reconstructed tomograms from wild type and NSD-defective yeast strains are shown. Ribosomes are indicated by white arrowheads, yellow arrowheads indicate ER, black arrowheads indicate the cell wall, and the nuclear envelope is indicated by the red arrowhead. Mito: mitochondria. Scale bar = 250 nm. Pixel size = 14.08 Å/pixel. Binning = 4.

### 3.2.3 Subtomogram Averaging of Ribosomes in NSD-defective Yeasts

To further characterize the ribosomes in NSD-defective yeasts, I carried out template matching with a template generated by manually-picked particles. Ribosomes were then subjected to 3D classification and refinement. Since the particle number of ribosomes extracted from each tomogram is much smaller compared with what can be used in SPA, I then decided to combine all tomograms for a larger scale of *in situ* structural analysis. In total, 64 tomograms of good quality from all NSD-defective yeast were selected and the average extracting number from each tomogram was set to 2500 for oversampling. Eventually, 153984 particles were extracted, followed by three rounds of 3D classification to clean out false positives, and 134481 particles remained (**Figure 29**). However, no ribosome class with a Ski-complex-like density or any other NSD-related complex densities was identified. Intriguingly, there was a ribosome class identified with a distinct extra density on SSU. This ribosome class took about 5.7% of the total population, and the final resolution reached at 16.09 Å (**Figure 29**). From the morphology and position of this extra density, it is speculated to be the yeast translation elongation factor 3 (eEF3) that is essential for the translation elongation in fungi ([Andersen, Becker et al. 2006](#), [Ranjan, Pochopien et al. 2021](#)).

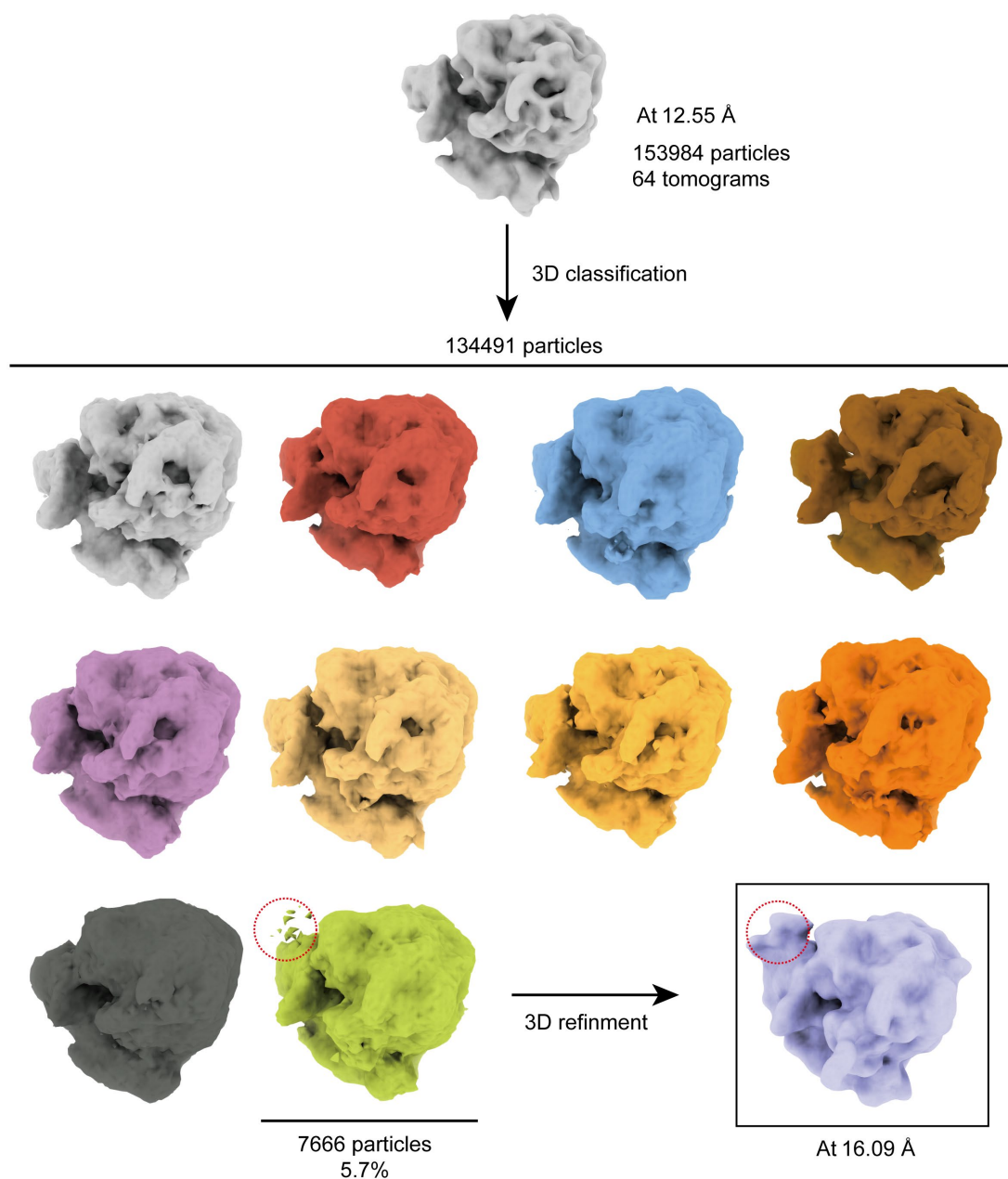


**Figure 29. Subtomogram averaging of ribosomes in NSD-defective yeasts.** All particles were subjected to a 10-class classification after the CTF correction, and the classification was performed three times with 25 iterations each time. Different classes are in different colors. The class (7666 particles, 5.7%) with the eEF3-like density is firstly presented in light green after the classification and eventually in light yellow after the final refinement. The extra density is indicated with red dotted circles. Pixel size = 3.52 Å/pixel.

### 3.2.4 Assessment of NSD Induction for Correlative FIB Milling

Since no Ski-complex-associated ribosomes were identified from NSD-defective yeasts after a 2-hour NSD induction, I then made a PGK1-nonstop construct fused with mApple for a more direct detection of the NSD reporter using fluorescence microscopy (FLM). In addition, I also fused Ski3, which is an indispensable part of the Ski complex, with eGFP not only as an internal control group for the measurement of fluorescence intensity but also for the colocalization with PGK1-nonstop. Yeasts cells were induced with 2% galactose for 12 hours. Images were taken every 2 hours, and OD<sub>600</sub> was recorded simultaneously for all groups. Since similar results were obtained for all NSD-defective yeasts in comparison with wild type yeasts, only images of Ski7<sub>ExoMut-</sub> and wild type yeasts, which were taken at 0 hour, 2 hours, 4 hours, and 6 hours, are shown in this dissertation as examples.

The FLM data showed that the intensity of mApple kept increasing as the time of galactose induction prolonged. But its intensity at 2 hours of galactose induction was not as strong as expected since the background noise was still presented in the image (**Figure 30**). This likely reflects inadequate expression of the NSD reporter. However, previous results from western blot suggested that 2-hour galactose induction was sufficient for yeasts to accumulate an enough number of NSD reporters. The two results thus appeared to be conflicting, likely due to the different sensitivity of western blotting and FLM. Western blot is a very sensitive method to detect the expression of proteins and it is carried out with a much larger number of cells. FLM in comparison is a much less sensitive method since it relied on the fluorescent signals emitted from a few cells. Therefore, the two results together might suggest that the expression of the NSD reporter in individual cells is not enough after 2-hour induction of galactose, explaining why there was no Ski-complex-associated ribosome class identified in the previous STA. Although mApple intensity still kept increasing after 12 hours, yeasts were not considered in a viable state for successive experiments. Thus, to balance the expression of NSD reporter and health of cells, 6-hour NSD induction was then chosen and applied in successive experiments.

In comparison, there was no significant increase in the expression of NSD reporter PGK1-nonstop in wild type yeasts where NSD is fully functional (**Figure 30**). Despite a difference in the expression of PGK1-nonstop between the wild type and Ski7<sup>ExoMut</sup>-yeasts, the growth rate showed no significant difference, indicating alternative pathways activated to attenuate NSD stress (**Figure 30**). In addition, the expression of PGK1-nonstop varied dramatically amongst cells when the fluorescence intensity in individual cells was compared (**Figure 30**), indicating an uneven induction of NSD in cells. Thus, correlative FIB milling on cells that have a strong expression of PGK1-nonstop is needed.

As a control, the expression of Ski3 was more stable with a mild increase over time in both wild type and Ski7<sup>ExoMut</sup>-yeasts (**Figure 31**). In some cells, Ski3 showed a strong colocalization with PGK1-nonstop, thus those cells were selected for correlative FIB milling.

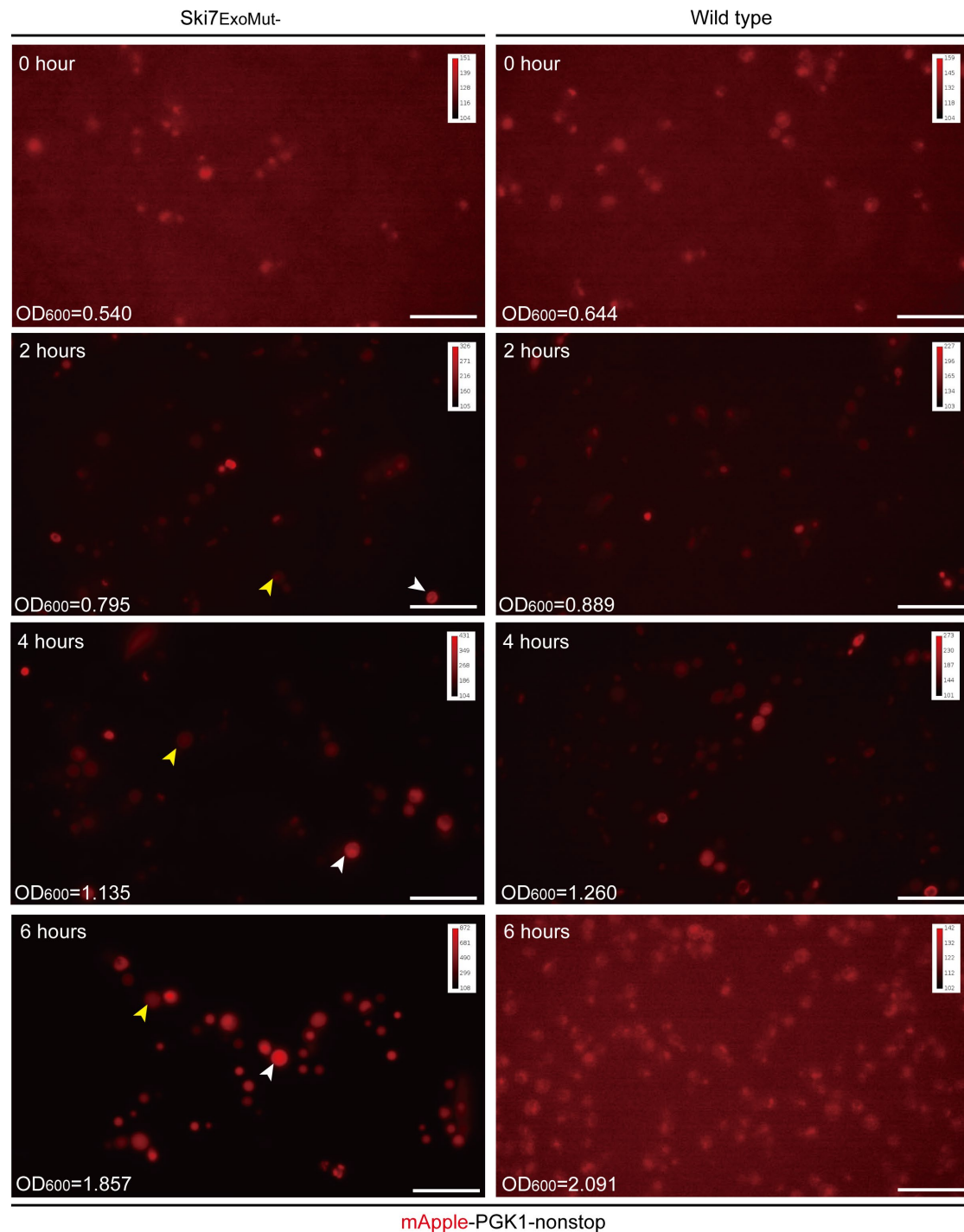


**Figure 30. Time-course FLM of wild type and *Ski7<sup>ExoMut-</sup>* yeasts detecting mApple-PGK1-nonstop under galactose induction.** *Ski7<sup>ExoMut-</sup>* is shown on the left, wild type is shown on the right. Images were taken in RFP channel at 0 hour, 2 hours, 4 hours, and 6 hours. The intensity was measured by ImageJ. Yeast cells with weaker fluorescence are indicated by

yellow arrowheads and those with stronger fluorescence are indicated by white arrowheads.

Scale bar = 10  $\mu$ m, the magnification = 63x, exposure time = 250 ms.

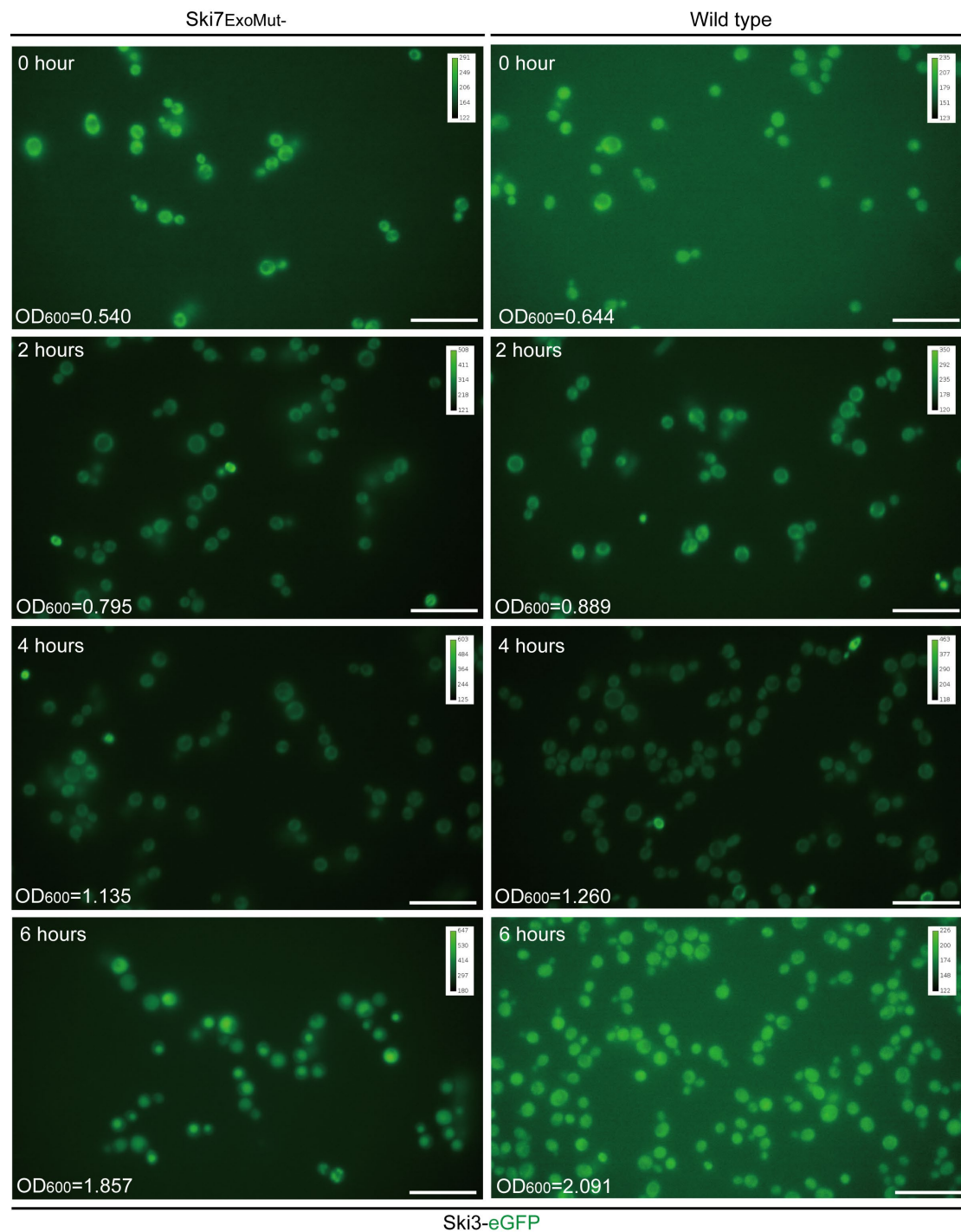


**Figure 31. Time-course FLM of wild type and Ski7<sub>ExoMut-</sub> yeasts detecting Ski3-eGFP under galactose induction.** Ski7<sub>ExoMut-</sub> is shown on the left, wild type is shown on the right. Images were taken in in GFP channel at 0 hour, 2 hours, 4 hours, and 6 hours. The intensity was measured by ImageJ. Scale bar = 10  $\mu$ m, magnification = 63x, exposure time = 250 ms.

### 3.2.5 Granule Aggregates in NSD-defective Yeast Cells

To target cells with a high expression of the NSD reporters, I carried out correlative FIB milling on those yeasts, which are highly fluorescent in both RFP and GFP channels after 6 hours of galactose induction, and recorded tomograms on corresponding regions of lamellae (**Figure 32 A, B**). For the fluorescence correlation in NSD-defective yeasts, the Z-stack acquisition was not required as the signal was evenly distributed across the whole cell. But due to the low number of highly fluorescent cells, only 1-3 yeast cells of interest were found on each lamella (**Figure 32 B**).

Intriguingly, a larger number of granule aggregates were found in the cytoplasm and their distribution was stochastic (**Figure 32 C, D**). Those granule aggregates were in clusters with more prominent granules in the center and smaller ones on the periphery (**Figure 32 E, F**), and ribosomes were notably excluded from them. The images showed that the size of those aggregates varies, some of them are in the same size of the mitochondrion while some of them are merely bigger than ribosomes. Based on the morphology, they resemble glycogen granules ([Wilson, Roach et al. 2010](#), [Prats, Graham et al. 2018](#)) that accumulate in yeasts under stressful conditions, therefore they could be related to the massive accumulation of NSD reporters in the cytoplasm.

Moreover, the density of ribosomes in those cells decreased dramatically, showing a much sparser distribution, and the size of vacuoles enlarges significantly compared with the wild-type yeast cells (**Figure 32 E**), indicating increase protein degradation. These together suggest that yeasts are under tremendous stress with prolonged NSD induction.

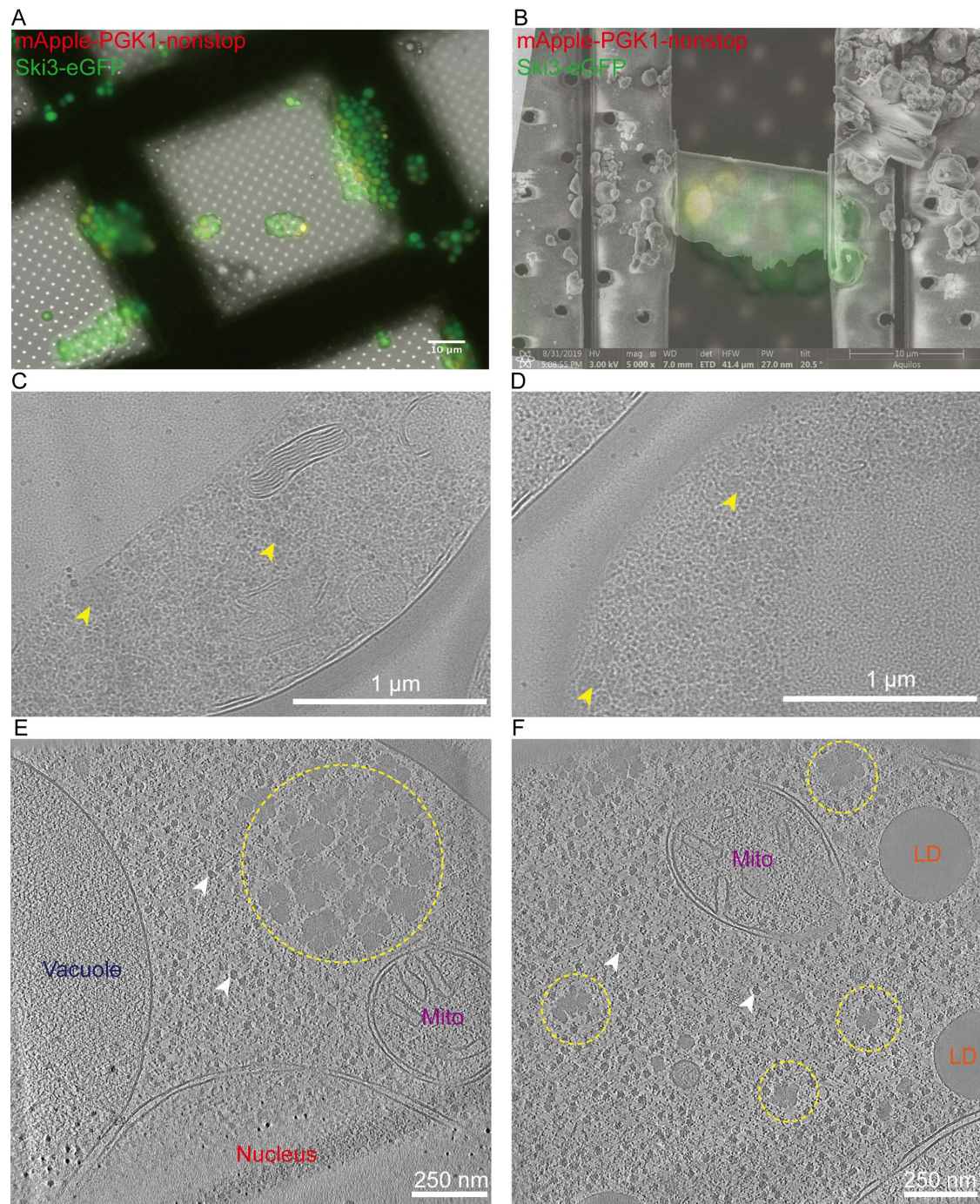


**Figure 32. Correlative FIB milling and tomograms of *Ski7<sup>ExoMut-</sup>* yeasts under 6-hour galactose induction.** (A) A merged image of yeasts under cryo-CLEM in BF, RFP, and GFP channels. The small yeast cluster sitting in the middle was chosen for the correlative milling. (B) The SEM image of the lamella image merged with (A), indicating positions of individual yeasts on the lamella. (C), (D) Two zoom-in TEM overviews of a correlatively milled lamella. Granule aggregate are indicated by yellow arrowheads. Magnification = 6500x. (E), (F) Reconstructed tomograms containing granule aggregates. Granule aggregates of different sizes are framed

with yellow dotted circles. Ribosomes are indicated by white arrowheads. Mitochondrion (Mito), lipid droplet (LD). pixel size = 14.08 Å/pixel. Tomograms were denoised with CryoCare.

### 3.2.6 Subtomogram Averaging of Ribosomes in Granule-aggregates-containing Yeast Cells

As shown in the previous section, the emergence of granule aggregates in NSD-defective yeasts was then hypothesized to be closely related to massive stalled ribosomes generated from the accumulation of NSD reporters after 6-hour galactose induction. To address that, I performed subtomogram averaging on ribosomes from those tomograms containing granule aggregates to obtain a ribosome class with the Ski complex attached.

In total, 14 tomograms were selected and 19991 ribosome particles were extracted for 3D classification and refinement. However, through several rounds of classification, no Ski-complex-associated ribosome class was identified. Only the eEF3-containing class was identified again but with a lower percentage (**Figure 33**).

To this end, I speculate that the missing of Ski-complex-associated ribosomes in NSD-defective yeast cells could be caused by the low abundance of both stalled ribosomes and the Ski complex, alternatively such complexes *in situ* could be extremely transient. Therefore, additional methods to enrich NSD-related complexes in living yeast cells are likely needed.

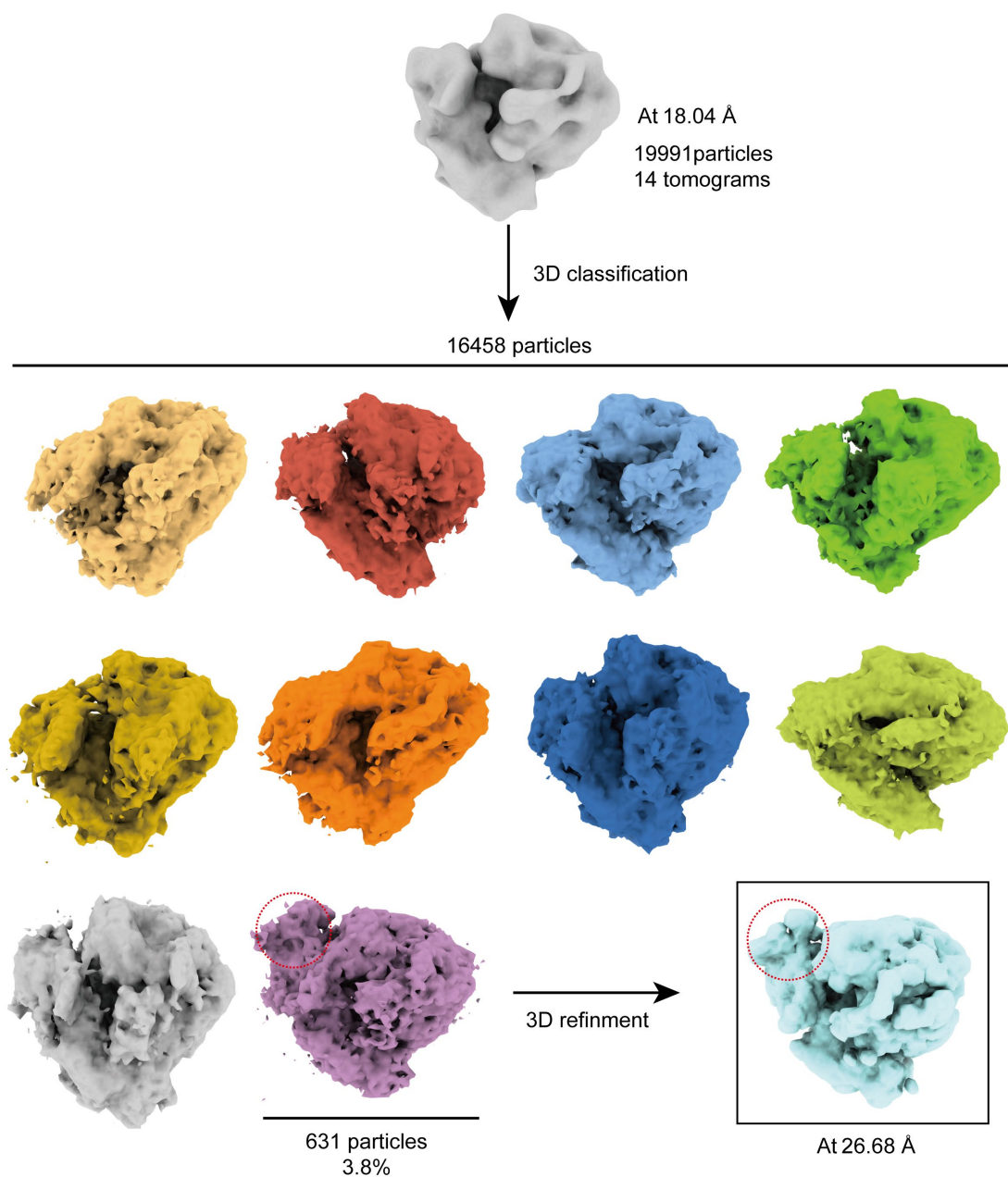


**Figure 33. Subtomogram averaging of ribosomes in granule-aggregates-containing Ski7ExoMut- yeasts.** Yeasts were induced with NSD for 6 hours. All particles were subjected to a 10-class classification after the CTF correction, and the classification was performed three times with 25 iterations each time. Different classes are in different colors. The class with the eEF3-like (631 particles, 3.8%) density is firstly presented in light purple after the classification and eventually in light blue after the final refinement. The extra density is indicated with red dotted circles. Pixel size = 3.52 Å/pixel.

### 3.2.7 Subcellular Localization of Ski7 with GPA1N9 and GEMs

To enrich stalled ribosomes in NSD-defective yeast at a specific subcellular location or a well-defined subcellular structure. I thus selected two constructs to perform the experiments. The first one is a well-defined spheric structure: genetically encoded multimer (GEM), which is a multimeric fluorescent nanoparticle with a diameter of 40 nm or 20 nm (named as GEM40 and GEM20). It is composed of homomultimeric scaffolds fused to a fluorescent protein (yGFP in this study). GEMs have been utilized in analyzing mTORC1-associated phase separation and verified to be an easily identifiable object in tomograms ([Delarue, Brittingham et al. 2018](#)). The second one is a plasma membrane signal peptide GPA1N9, which is sufficient for anchoring fusion proteins to the plasma membrane in yeasts ([Gillen, Pausch et al. 1998](#)). GPA1N9 used in my study is fused with mApple.

In detail, I cloned the N-terminus of Ski7 with GEM40/20 and GPA1N9, respectively. C-terminus of Ski7 was truncated for impairing the NSD. A Strep tag was put at the 3' end of GEM40/20 fused constructs (**Figure 34 A**). Separately, I also created GPA1N9-Rrp44, GPA1N9-Ski3, and GPA1N9-Rpn5 constructs, of which the first two are speculated to enrich NSD-related complexes while Rpn5, which is a constituent of the lid complex of 26S proteasome, serves as the control group for following cryo-ET study. A FLAG tag was constructed at the 3' end of GPA1N9 fused constructs (**Figure 34 B**).

After generating those constructs, I first tested GEM40/20-Ski7 constructs in both wild type and *hbs1Δ ski7Δ* yeast cells and measured the expression of corresponding proteins by western blot and FLM.

In the western blot, bands of GEM40-Ski7<sup>C</sup>, GEM20-Ski7<sup>wt</sup>, and GEM20-Ski7<sup>C</sup> were detected for both wild type and *hbs1Δ ski7Δ* yeasts but the bands from *hbs1Δ ski7Δ* yeasts were stronger, which was expected since there is no competition from the endogenous Ski7 in *hbs1Δ ski7Δ*s yeast cells (**Figure 35 A**). Nevertheless, several faint bands were also detected in the individual lane of all fusion proteins, indicating potential degradations of proteins. Moreover, there was a constant band at the size of

GEM40/20 in all lanes, implying that a potential cleavage between GEM40/20 and other proteins might have happened due to the multimerization of GEM40/20. Separately, pull-down assay was conducted to characterize the interactome of GEM40/20-Ski7 fusion proteins in *hbs1Δ ski7Δ* yeasts, but there was no significant difference between the GEM40 and GEM40/20-Ski7 fusion protein ( **Figure 35 B** )

In FLM, the fluorescent intensities of different groups were assessed. The GFP signal was detected in all yeasts, whereas the GFP signal in the GEM40 yeasts was much stronger than others (**Figure 36**). Besides, fast-moving green puncta, representing mature GEM particles, were detected in all groups, but the number of puncta was much higher in the GEM40 yeasts (**Figure 36**). Therefore, these data suggest that the expression of GEM40/20 is affected by the length of fusion constructs, the longer the construct is, the less GEM40/20 is expressed, leading to the fewer GEM40/20 nanoparticles in the cell.

In parallel, cryo-ET was performed on the *hbs1Δ ski7Δ* yeast cells expressing the GEM40-Ski7 fusion protein to verify the existence of GEM particles in tomograms. Lamellae were prepared without any correlation because the fluorescence was diffused across the entire cell. In total, 18 tomograms were reconstructed and denoised. However, much fewer GEM40 nanoparticles were observed in my tomograms in comparison with what was stated in ([Delarue, Brittingham et al. 2018](#)) (**Figure 35 C, D**). Due to the small number of GEM40 nanoparticles in each tomogram, it would not be wise to continue with this construct for the subcellular localization.

Then I continued to test the validity of GPA1N9 for the subcellular localization to the plasma membrane, FLM and western blot were performed on GPA1N9 and GPA1N9-Rpn5 yeasts. In the western blot, both GPA1N9 and GPA1N9-Rpn5 were detected using anti-FLAG antibodies ( **Figure 37 A** ). However, there was a strong extra band presented in the size of GPA1N9 in the GPA1N9-Rpn5 lane, which was similar to what was found for GEM40/20 fusion proteins, indicating partial degradation of the fusion proteins.

In FLM, both GPA1N9 and GPA1N9-Rpn5 yeasts showed mApple fluorescence on the plasma membrane, but the fluorescence in GPA1N9-Rpn5 yeasts was slightly weaker than that of GPA1N9 yeasts ( **Figure 37 B**). The mApple fluorescence could also be seen in vacuoles in both strains ( **Figure 37 B**), indicating partial degradations of the fusion proteins as well. This was consistent with the western blot result.

Taken together, I conclude that GPA1N9 is sufficient to localize proteins fused with it to the plasma membrane, but its effectiveness in cryo-ET remains to be determined. For other GAP1N9-fused proteins not examined, subsequent biochemical and cryo-ET analysis will be carried out once they are verified to function correctly in my yeast strains.

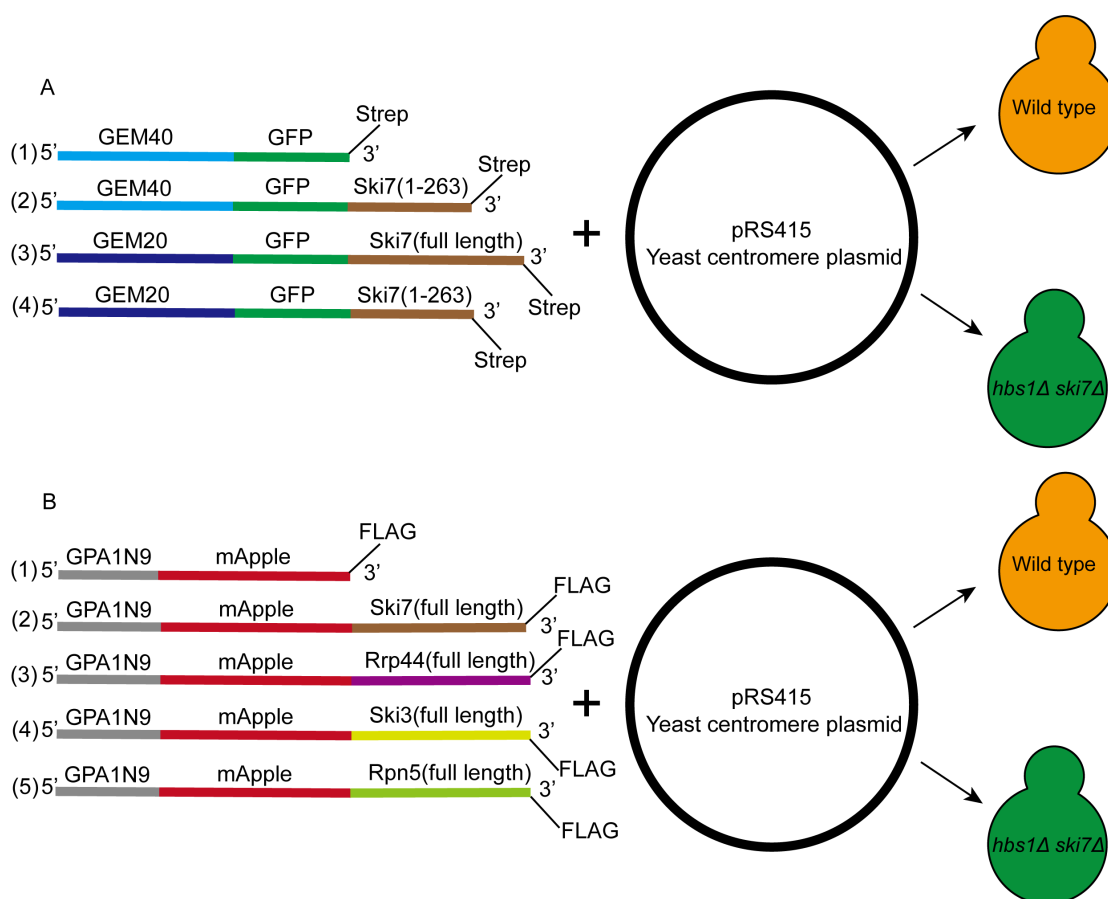


**Figure 34. Schematic illustration of generating yeast strains for subcellular localization.**

(A) Schematic illustration of generating GEM40/20-Ski7 strains. (1): GEM40; (2): GEM40-Ski7c-; (3): GEM20-Ski7; (4): GEM20-Ski7c-. DNA fragments were joined by Gibson assembly and cloned into the yeast centromere plasmid pRS415. A Strep tag sequence is added to the 3' end of each construct. New constructs were transformed into wild type and *hbs1Δ ski7Δ*

yeasts, producing eight new strains. (B) Schematic illustration of generating GPA1N9, GPA1N9-Ski7, -Rrp44, -Ski3, and -Rpn5 strains. (1): GPA1N9; (2): GPA1N9-Ski7; (3): GPA1N9-Rrp44; (4): GPA1N9-Ski3; (5): GPA1N9-Rpn5. DNA fragments were joined by Gibson assembly and cloned into the yeast centromere plasmid pRS415. A FLAG tag sequence is added to the 3'end of each construct. New constructs were transformed into wild type and *hbs1Δ ski7Δ* yeasts, producing ten new strains.

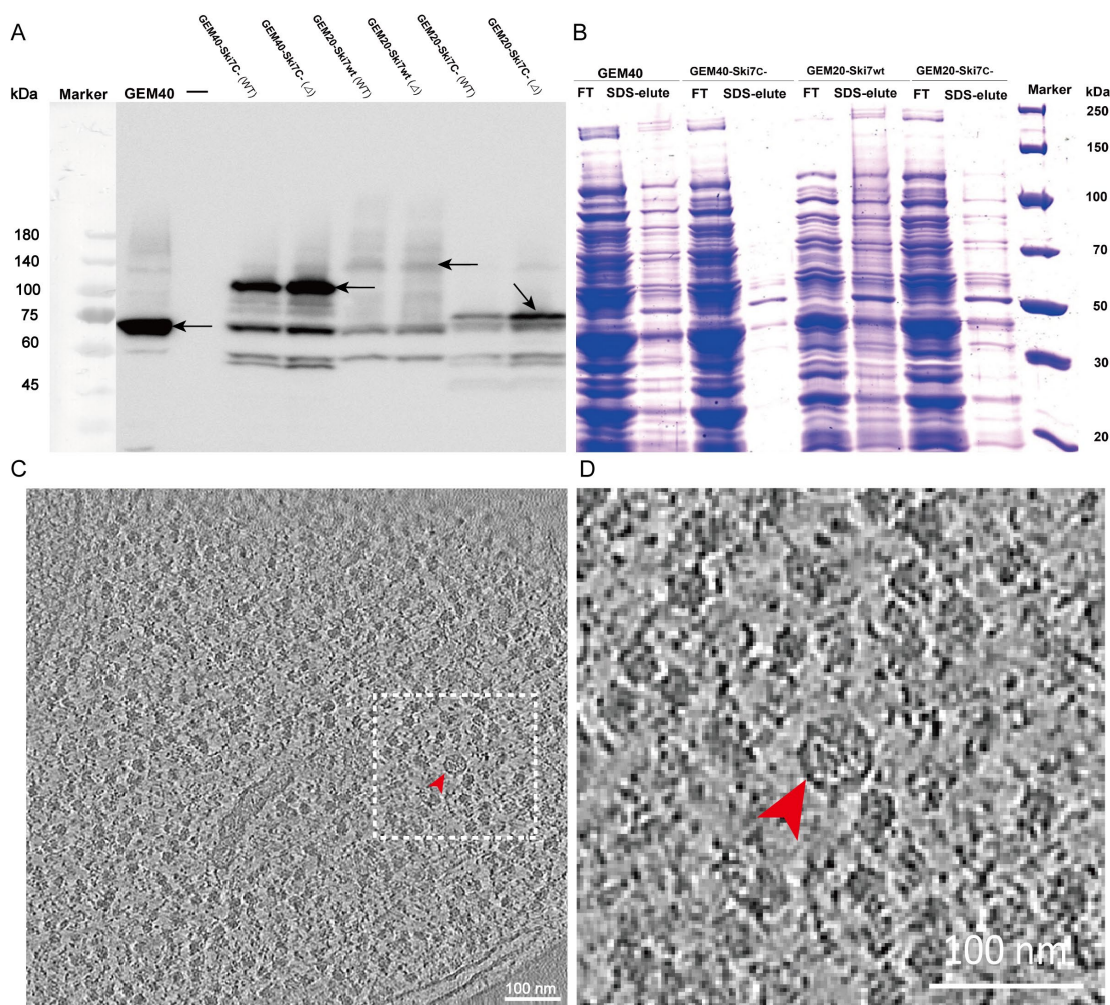


**Figure 35. Verification of GEM40 and GEM40/20-Ski7 constructs.** (A) Western blot against GFP. True signal bands are indicated with black arrows based on the molecular mass of each fusion protein. Negative control is Ski7wt. (WT): expressed in wild type yeasts. (Δ): expressed in *hbs1Δ ski7Δ* yeasts. (B) Pull-down of GEM40/20-Ski7 fusion proteins in *hbs1Δ ski7Δ* yeasts. Proteins were pulled down by G-beads coated with GFP antibodies. Gel was stained with Coomassie Blue. FT: the flow through before washing. (C) One representative tomogram slice of GEM40 yeasts. The GEM40 nanoparticle is indicated by the red arrowhead. The area framed

by white dots is enlarged as (D) for better visualization of the GEM40 particle. Scale bar = 250 nm. Pixel size = 14.08 Å/pixel. The tomogram was denoised with CryoCare.

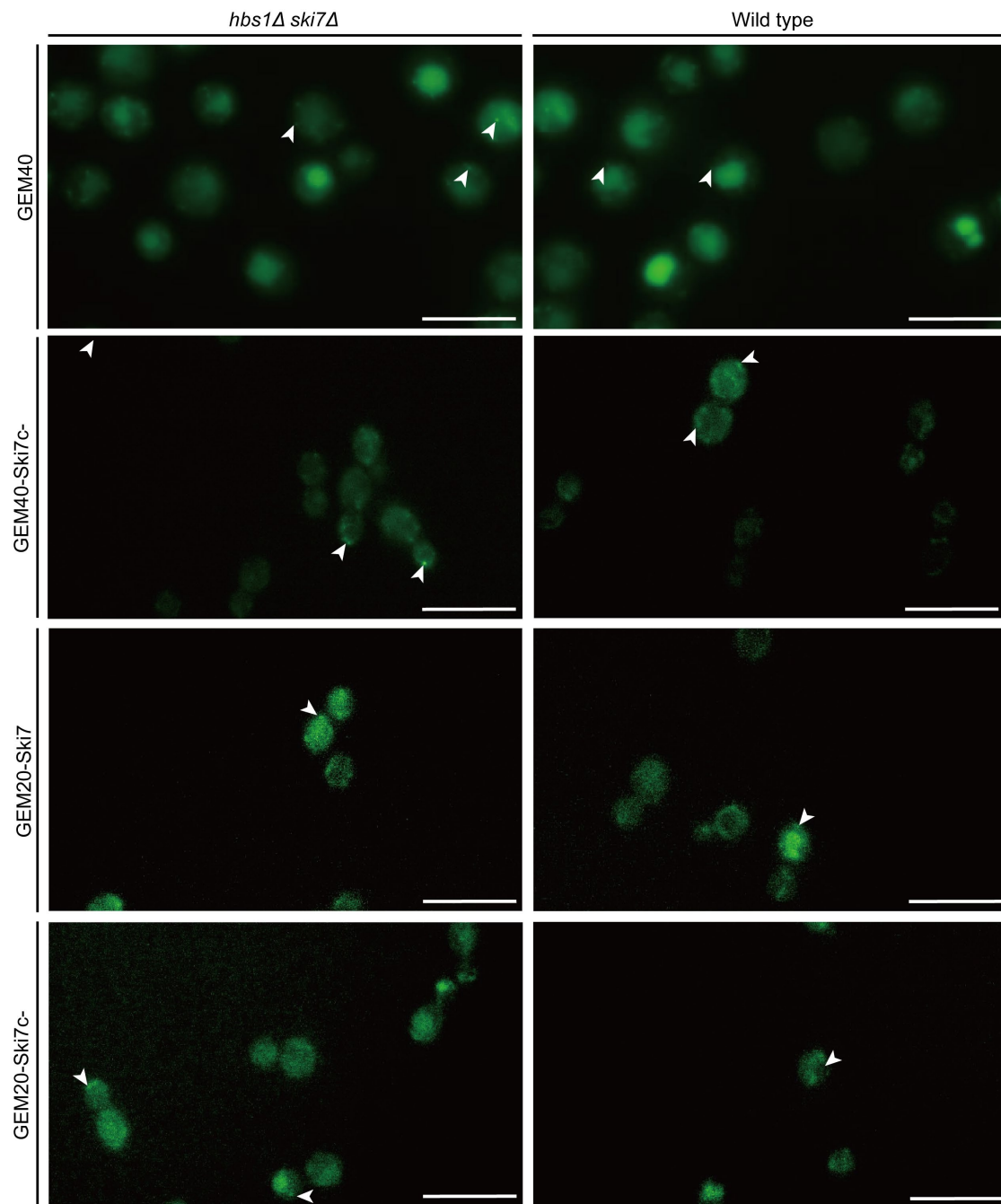


**Figure 36. FLM of GEM40 and GEM40/20-Ski7 strains.** In total, eight fluorescence pictures of cells from eight strains are presented. Strains with *hbs1Δ ski7Δ* genetic background are depicted in the left column, strains with wild type genetic background are depicted in the right column. Fast-moving puncta are indicated with white arrowheads. Images were taken in GFP channel. Scale bar = 5  $\mu$ m. Magnification = 63x. Exposure time = 250 ms.

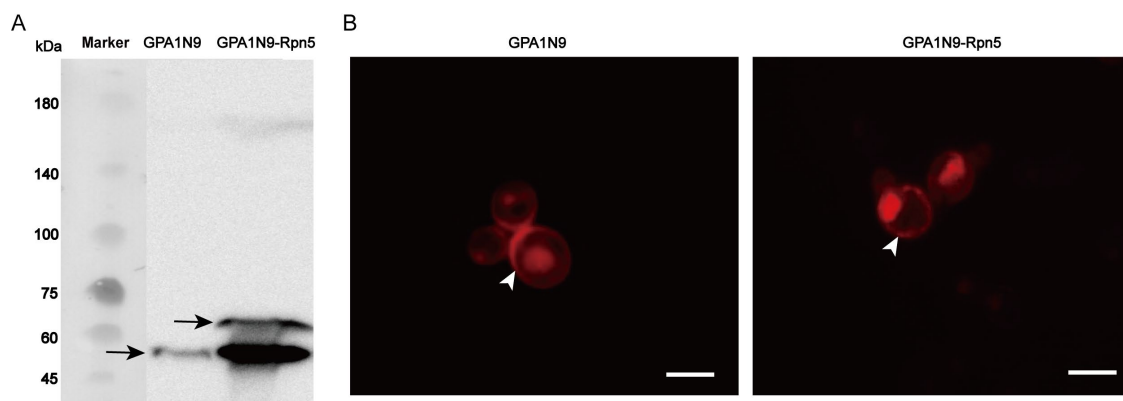


**Figure 37. Verification of GPA1N9 and GPA1N9-Rpn5 constructs.** (A) Western blot using the anti-FLAG antibody. Protein lysate was prepared from wild type yeasts expressing GPA1N9 and GPA1N9-Rpn5. Corresponding signal bands are indicated with black arrows. (B) FLM of GPA1N9 and GPA1N9-Rpn5 yeasts. Yeasts are in the wild type genetic background. The fluorescence image of GPA1N9 yeasts is depicted on the left and the fluorescence image of GPA1N9-Rpn5 is depicted on the right. Fluorescence on the plasma membrane is indicated by white arrowheads. Images were taken in RFP channel. Scale bar = 2  $\mu\text{m}$ , magnification = 63x, exposure time = 250 ms.

### 3.3 Discussion

In the NSD project, I successfully established a workflow for the *in situ* analysis of nonstop mRNA decay in yeasts to explore the participation of ribosomes in mRNA surveillance mechanisms. However, the ribosome class with the anticipated NSD-related complexes has not been identified yet. The reason why such a structure of stalled ribosomes with the Ski complex was not resolved in my study as what has been achieved in the previous SPA study ([Schmidt, Kowalinski et al. 2016](#)) lies in several possibilities. The first is the particle number, which can easily be over 1 million in one data set for SPA but is much limited in STA. Usually 1500-2000 ribosomes at maximum can be extracted from a tomogram recorded at the magnification of 42k (pixel size = 3.52  $\text{\AA}$ /pixel), which means even with 100 tomograms, around 100-200k particles can be gathered. Considering the time spent preparing samples and the attrition rate during the sample transferring, it is thought to be inefficient to increase the particle number in STA to classify particular structures.

To avoid taking a huge number of tomograms, the enrichment of target particles is then needed for cryo-ET, which has been considered at the initial phase of this project. Genetic manipulations on NSD-related genes were performed to defect NSD and NSD reporters were expressed in the NSD-defective strains to increase the amount of NSD events and stalled ribosomes. However, this still might not be enough to enrich the ribosome-Ski complexes to meet the lowest percentage requirement (5-10% of the total population). As I incidentally found a rare ribosome class with the eEF3-like density ([Andersen, Becker et al. 2006](#), [Ranjan, Pochopien et al. 2021](#)) (**Figure 38 A, B**) that was verified with model fitting presenting an overall good fit (**Figure 38 C, D, E**). I compared the copy number of eEF3 with that of Ski3 in yeasts and the result was striking. According to the average from different databases, the copy number of eEF3 is estimated to be from 200k-400k per cell, while the copy number of Ski3 only ranges from 1.5 to 2.5k per cell ([Ho, Baryshnikova et al. 2018](#)). This means that eEF3 on average is hundreds of times more abundant than Ski3 in yeast cells. But even with 200k-400k copies of eEF3 per cell, only 3.8-5.7% of ribosomes from my *in situ* data was associated with eEF3, suggesting that it would be unlikely to obtain an *in situ* ribosome-Ski complex structure from my current data set.

Moreover, NSD-defective yeasts were found surviving after a long time of NSD induction, implying that the yeasts can circumvent NSD stress by utilizing alternative mechanisms, e.g., RQC. In addition, during the NSD induction by galactose, the extent of accumulation of NSD reporters varied dramatically amongst cells. In some cells, there were barely any fluorescent signals detected, while some cells were found highly fluorescent, and this difference could result from the induction system I applied in this project and could also be caused by the uneven distribution of plasmids during the cell division, which could hardly be reflected by biochemical analyses. Unlike conventional biochemical analyses carried out with a large number of cells, cryo-ET is conducted on a single-cell scale, which then requires a more accurate and stronger induction system.

Unexpectedly, we observed massive granule aggregates to emerge in the cytoplasm after the prolonged NSD induction and the actual reason for that remains elusive. Although the granule aggregates in my study resemble glycogen granules ([Wilson,](#)

[Roach et al. 2010](#), [Prats, Graham et al. 2018](#)), a solid conclusion cannot be drawn yet, and the exact mechanism by which they were induced in NSD-defective yeasts after the NSD induction needs further investigations. In general, the emergence of granule aggregates added up complexities to the identification of stalled ribosomes in NSD.

Another possibility for the missing structure of the stalled ribosome with NSD-related complexes could be the highly dynamic and transient nature of NSD, which is reflected by the low copy numbers of proteins involved in it. There have been some studies indicating that those complexes may participate in this process sequentially rather than through the formation of a well-ordered stable complex ([Kowalinski, Kögel et al. 2016](#), [Schmidt, Kowalinski et al. 2016](#), [Zinoviev, Ayupov et al. 2020](#)). Even in the previous SPA studies of these complexes, the synchronization of ribosomes was still needed to obtain a stable structure.

The cell volume contained in one lamella only accounts for 1-3% of the total cell volume. Therefore, the chance by which the stalled ribosomes with NSD-related complexes could be captured in tomograms would be extremely low if the NSD took place across the whole cell. To address that, in the later phase of my research, I proposed new strategies to enrich stalled ribosomes with NSD-related complexes at specific subcellular locations or structures. GEMs and GPA1N9 were utilized to anchor Ski7, but the expression of GEMs was severely decreased when fused with Ski7. Following that, new constructs were made with GPA1N9, and I have already verified the effectiveness of GPA1N9 in subcellular localization to the plasma membrane with two fusion proteins GPA1N9 and GPA1N9-Rpn5. Further assessments on those constructs shall be carried out.

In summary, despite difficulties in identifying the stalled ribosomes with NSD-related complexes in cellular context, novel strategies have been developed to improve the application of cryo-ET in studying transient mechanisms and promising progresses have been made in this project.

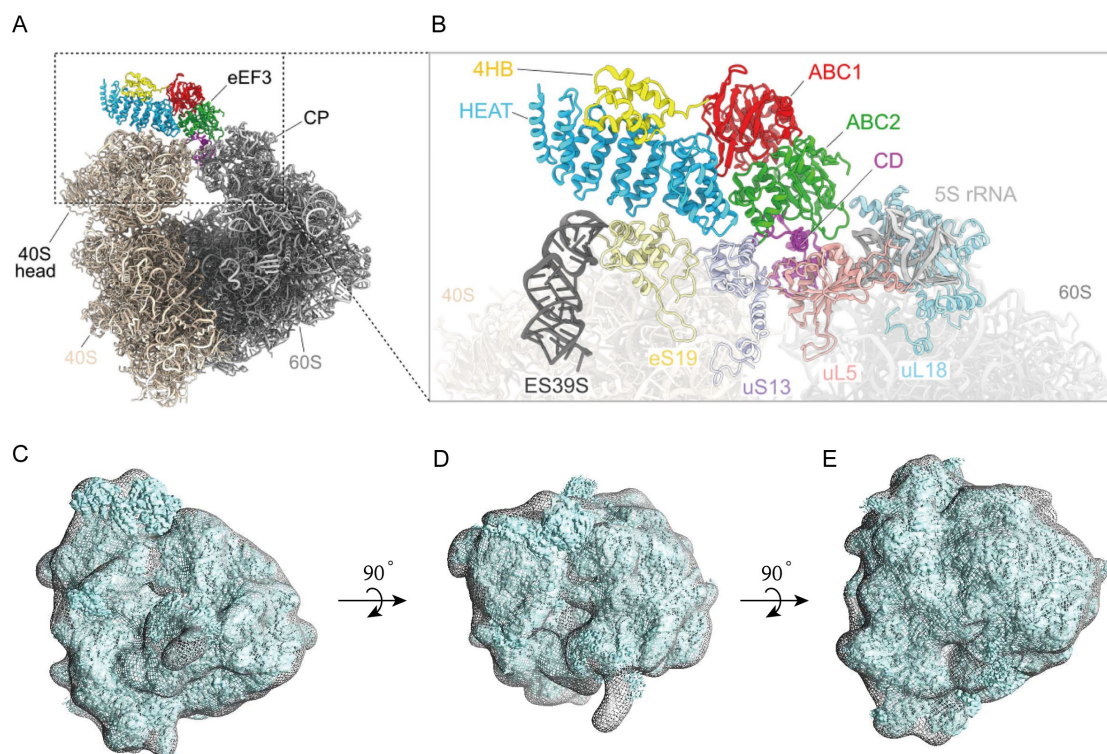


**Figure 38. The structural comparison between the published eEF3-80S ribosome structure and the ribosome structure containing an eEF3-likedensity.** (A) The overview of the eEF3-80S molecular model. (B) The overview of eEF3. ES39S is colored in dark gray, uS13 is in pastel violet, eS19 is presented in pale yellow, uL18 is in light blue, uL5 is depicted in coral and 5S rRNA is colored in light gray. Adapted from Ranjan et al., 2021. (C)-(E) Model fitting of the eEF3-containing ribosome class with EMD-12081, the published EM density map of (A). (C) Front view; (D) Side view; (E) Back view. The structure is presented in gray mesh and the published structure is in light blue with solid densities. The fitting and visualization were performed with Chimera.

## 4. SLP65-CIN85 LLPS Project

### 4.1 Introduction and Aims

This section introduces our current understanding of BCR activation in B lymphocyte and previous research on a key protein complex SLP65-CIN85 involved in this process. The detailed molecular mechanism is covered and our current understanding of the novel SLP65-CIN85 LLPS is described. Based on this, aims are set to find the missing information on function of this LLPS in B cell activation.

#### 4.1.1 The B Lymphocyte and BCR Activation

The B lymphocyte is white blood cell and plays an indispensable role in the adaptive immune system. For mammals, it matures in the bone marrow, while for poultries, it matures in the bursa of Fabricius. For example, the chicken DT40 cell derived from the bursa of Fabricius of chickens is a canonical cell line widely used in many B lymphocyte-related studies ([Winding and Berchtold 2001](#), [Cooper 2015](#)). The function of B cells depends on their status: resting and activated, which relies on the switch on/off of several signaling pathways. The activation of B cells is triggered by the binding between antigens and B cell receptors (BCRs). BCRs are antibodies, which are not secreted but translocated on the plasma membrane ([DeFranco 1997](#)). After the activation, B cells undergo a fast proliferation and differentiation that gives rise to the antibody-secreting plasma cells, memory B cells, etc. ([DeFranco 1997](#), [Reth and Wienands 1997](#)).

The activation of B cells occurs in secondary lymphoid organs, such as the spleen, where numerous antigens are presented to them for recognition ([Loder, Mutschler et al. 1999](#)). After the activation by various antigens, B cells undergo immunoglobulin class switching to produce various antibodies against these antigens. The activation of B cells is critical for the production of antibodies and pivotal for the T cells to recognize the antigens. During the activation, some B cells undergo endocytosis to degrade the antigens resulting in a production of fragmented peptides. Those peptides are then presented with the major histocompatibility complex II (MHC-II) to T cells, and the

following endocytosis is mediated by the BCRs ([Jurewicz and Stern 2019](#), [Kwak, Akkaya et al. 2019](#)).

The BCR is composed of the membrane-bound immunoglobulin (Ig) and the Ig- $\alpha$ /Ig- $\beta$  heterodimer. The membrane-bound Ig is responsible for antigen-binding while the Ig- $\alpha$ /Ig- $\beta$  heterodimer is essential for the subsequent signaling ([Schamel and Reth 2000](#), [Casola, Otipoby et al. 2004](#)). The binding of antigens causes phosphorylation and conformational changes to the immunoreceptor tyrosine-based activation motifs (ITAMS) of the Ig- $\alpha$ /Ig- $\beta$  heterodimer ([Reth 1989](#), [Benschop and Cambier 1999](#))(**Figure 39**). Besides, this process is coupled with a fast and transient aggregation of multimeric complexes, including several enzymes and second messengers, which has been shown to be associated with a highly coordinated subcellular relocation ([Rudd 1999](#)).

After that, the next critical step in the BCR-mediated B cell activation is the engagement of protein tyrosine kinases (PTKs), of which the Src family is dominant. The activated Src family kinases include Blk, Lyn, Syk, and Btk ([Treanor 2012](#)). The phosphorylated Syk has been shown to bind to the ITAMs and then phosphorylate one of its substrate protein named SLP65 (also known as B cell linker:BLNK) ([Fu, Turck et al. 1998](#), [Wienands, Schweikert et al. 1998](#)) which is a key player in initializing the downstream signaling pathways, such as Ca<sup>2+</sup> mediated NFAT pathway, NF $\kappa$ B pathway and Ras/Raf/MAPK pathway ([Burger and Wiestner 2018](#)) (**Figure 39**).

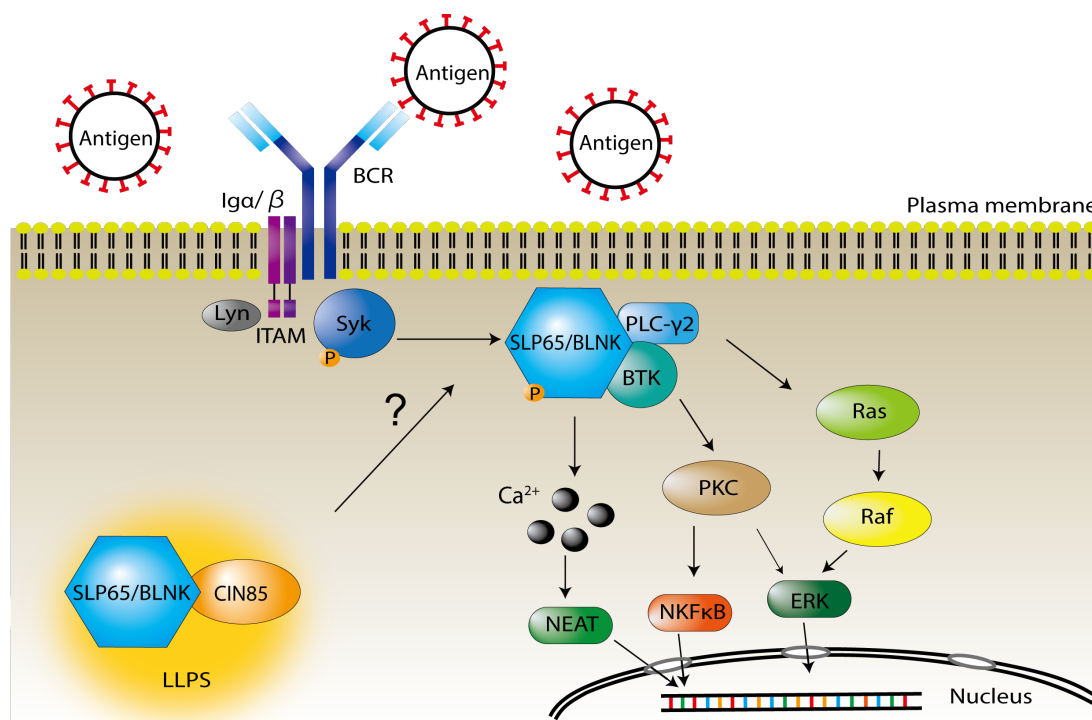


**Figure 39. Schematic illustration of BCR-mediated activation of B lymphocytes.** This scheme shows major signaling pathways, including Ca<sup>2+</sup> mediated NEAT pathway, BTK-NFκB pathway, and Ras-ERK pathway involved in the activation of B lymphocytes, in which the phosphorylation of Syk upon the binding to the ITAM of BCR that undergoes a conformational change when antigens are present results in the phosphorylation of SLP65/BLNK, and it sequentially triggers the downstream pathways well known in cell proliferation and differentiation. SLP65-CIN85 is depicted in a yellow circle standing for the LLPS area. However, the translocation of SLP65/BLNK-CIN85 to the plasma membrane remains unclear.

#### 4.1.2 SLP65 and CIN85

Activated BCRs recruit the spleen tyrosine kinase Syk that contains tandemly arranged Src homology 2 (SH2) domains ([Kurosaki and Tsukada 2000](#)). The phosphorylated Syk subsequently interacts with another SH2 domain-containing adaptor protein with a molecular weight of 65 kDa, thus named SLP65 or BLNK ([Fu, Turck et al. 1998](#), [Wienands, Schweikert et al. 1998](#), [Abudula, Grabbe et al. 2007](#)). The SH2 domain of SLP65 is on its C-terminus, and the interaction causes the phosphorylation of nine tyrosine residues and over twenty serine residues on SLP65, which enables it to activate the downstream signal transducers, for instance, the Bruton's tyrosine kinase (BTK)

that phosphorylates PLC- $\gamma$ 2 ([Ishiai, Kurosaki et al. 1999](#), [Su, Zhang et al. 1999](#), [Pal Singh, Dammeijer et al. 2018](#)). After that, various signaling pathways, including the nucleation of Ca<sup>2+</sup>, are triggered, and the B cells are activated. Based on previous studies, the Ca<sup>2+</sup> initiation complex works at the periphery of B cells upon the activation. SLP65 is not originally produced and located at the same spot, which indicates an effective translocation of SLP65 to the plasma membrane, followed by the recruitment of the Ca<sup>2+</sup> initiation complex ([Kurosaki and Tsukada 2000](#)). However, the mechanism by which SLP65 is translocated remains unclear.

It has been demonstrated that the loss of SLP65 significantly impairs the immune response and impedes the activation of B cells in different organisms. Therefore, SLP65 is regarded as a gatekeeper for B cell activation ([Jumaa, Wollscheid et al. 1999](#)). Through the studies on the sequence and structure of SLP65, it has been reported to be an intrinsically disordered protein ([Wong, Maier et al. 2018](#)). Apart from containing tyrosine phosphorylation sites, it also contains several proline-rich motifs that are believed to be responsible for its binding to SH3 domain-containing proteins ([Abudula, Grabbe et al. 2007](#), [Oellerich, Bremes et al. 2011](#)). The N-terminus of SLP65 is structurally disordered and indispensable for the function SLP65 has in B cell activation. Previous studies have demonstrated that lipid vesicles bind to the N-terminus of SLP65 both *in vitro* and *in vivo* ([Köhler, Storch et al. 2005](#), [Engelke, Pirkuliyeva et al. 2014](#), [Wong, Maier et al. 2018](#)) (**Figure 40 A**), but how this interaction attributes to the translocation of SLP65 remains unclear. Moreover, the SH2 domain and SH3-binding motifs of SLP65 are both crucial for its binding to a non-ITAM phosphotyrosine of Syk ([Engelke, Pirkuliyeva et al. 2014](#), [Kühn, Wong et al. 2016](#)), which in turn brings SLP65 close to the ITAM domain of Syk for subsequent phosphorylation ([Bohnenberger, Oellerich et al. 2011](#)).

There are three ligand classes for SLP65 in B cells, the first class includes some transient protein complexes involved in Ca<sup>2+</sup> mediated signaling pathways, for instance, Grb2 and Nck ([Oellerich, Bremes et al. 2011](#)). The second class includes the CapZ family that plays a role in sustaining the cytoskeleton, the interaction between SLP65 and the second class happens lately after the activation of B cells ([Oellerich, Bremes et](#)

[al. 2011](#)). The third class is characterized as a group of interactors that form a stable and long-lasting interaction with SLP65, including CD2AP and CIN85 ([Oellerich, Bremes et al. 2011](#), [Engelke, Pirkuliyeva et al. 2014](#)). Thus, CD2AP and CIN85 are initially identified as two critical interactors of SLP65 in BCR-mediated B cell activation and were later shown to play an extensive role in cell surface receptor-related signaling ([Zhang, Zheng et al. 2009](#)). CD2AP and CIN85 contain three major domains: a tetra-SH3 domain on the N-terminus, a proline-rich environment in the middle, and a coiled-coil domain on the C-terminus([Oellerich, Bremes et al. 2011](#)).

Studies have shown that CD2AP and CIN85 bind to the SH3-binding motifs of SLP65 that contain three conserved proline/arginine-based docking sites ([Oellerich, Bremes et al. 2011](#)). Three SH3 domains of CD2AP and CIN85 are well accommodated to those three motifs of SLP65 when the interaction happens ([Oellerich, Bremes et al. 2011](#), [Wong, Maier et al. 2018](#)). Nevertheless, the SH3 domain of CD2AP has been shown to be unrelated to the translocation of SLP65, while the SH3 domain of CIN85 is highly associated with the translocation of SLP65 ([Oellerich, Bremes et al. 2011](#)). The translocation of SLP65 is completely lost when its interaction with CIN85 is abolished ([Oellerich, Bremes et al. 2011](#), [Engelke, Pirkuliyeva et al. 2014](#)). Since the translocation of SLP65 from the cytosol to the plasma membrane is essential for its function in B cell activation, CIN85 is the key interactor of SLP65 in B cell activation ([Kühn, Wong et al. 2016](#)). More interestingly, interruption of the binding between CIN85 and SLP65 either by mutating the SH3-binding motifs or by depleting CIN85 has been shown to severely undermine the B cell activation affecting and even abolish some key signaling pathways ([Kühn, Wong et al. 2016](#)). However, the preformed complex of CIN85 and SLP65 is not engaged at the early stage where BCR-mediated phosphorylation of Syk takes place([Oellerich, Bremes et al. 2011](#), [Engelke, Pirkuliyeva et al. 2014](#)). This indicates that the translocation of SLP65, aided by CIN85, is signaled after the phosphorylation of Syk. Further structural studies also show that the C-terminus of CIN85 naturally forms a coiled-coil trimer, indicating an enhanced ability to bridge more interactions with lipids ([Kühn, Wong et al. 2016](#)) (**Figure 40 B, C**).

SLP65 and CIN85 together have been observed to form puncta in the resting B cells before the activation, and those puncta are proven to be the product of SLP65-CIN85 LLPS ([Engelke et al., 2014](#)). Functional analysis showed that SLP65-CIN85 puncta are closely related to the effectiveness of B cell activation, and most importantly, it plays a pivotal role in orchestrating the translocation of SLP65 to the plasma membrane ([Oellerich, Bremes et al. 2011](#), [Wong, Maier et al. 2018](#)). In addition, studies have specified that it is the 50 amino acid residues on the N-terminus of SLP65 that harness the lipid-binding ability, and the deletion of the 50 amino acid residues results in the loss of SLP65-CIN85 puncta in resting B cells ([Engelke, Pirkuliyeva et al. 2014](#)). Interestingly, SLP65 colocalizes with exosome-like vesicles labeled with vesicle-associated membrane protein 7 (VAMP7) and quinacrine that stains ATP ([Engelke, Pirkuliyeva et al. 2014](#)). The colocalization is lost when CIN85 is knocked out, indicating a critical role that CIN85 plays in the interaction between SLP65 and exosome-like vesicles ([Kühn, Wong et al. 2016](#)).

Taken together, previous studies on the SLP65-CIN85 LLPS and its function in the activation of B lymphocytes have disentangled this intricate process in great detail and much broadened our understanding of the mechanism of SLP65 translocation. However, no valid structure of SLP65-CIN85 has been obtained since the complex is believed to be intrinsically disordered. This hinders our understanding of the LLPS organization and their crucial function in the B cell activation. In particular, the information on lipid vesicles involved in the LLPS is incomplete due to the limited resolution of fluorescence microscopy and the lack of knowledge of their potential membrane source. Besides, most of the information is obtained from *in vitro* experiments through the simplification of the system and favored manipulations, which can induce inevitable bias to the results. Therefore, there is a need to obtain the conformational information of the SLP65-CIN85 LLPS at a higher resolution and investigate it in its native environment.

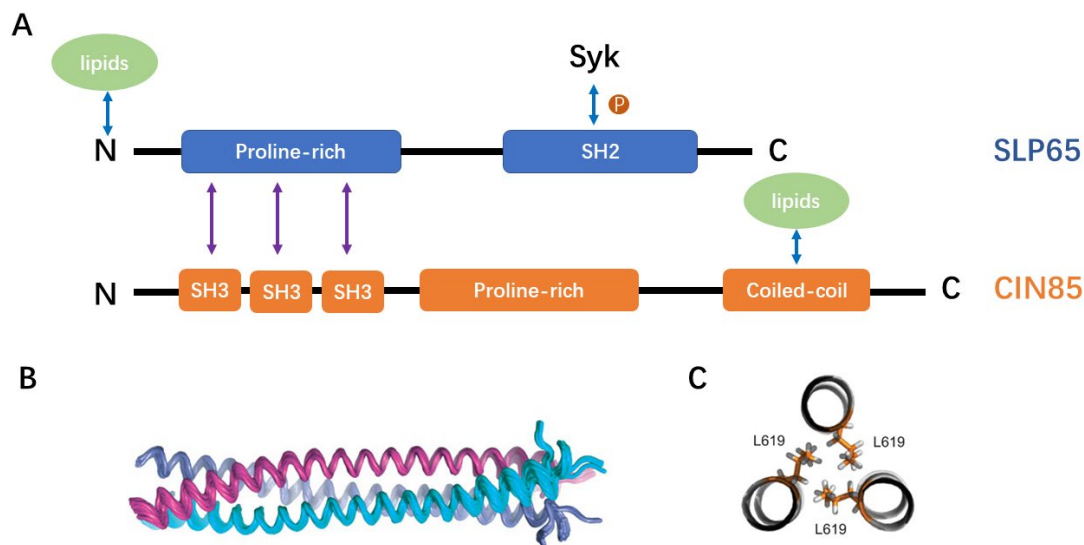


**Figure 40. Overview of SLP65 and CIN85.** (A) According to the sequence and functional analysis of SLP65 and CIN85, they both contain a proline-rich domain which of SLP65 is essential for its interaction with CIN85 on the tetra-SH3 domain of CIN85. The SH2 domain of SLP65 serves as the phosphorylation site, and the N-terminus of SLP65 is believed to be responsible for binding to lipids. (B) and (C) NMR structure of the C-terminus of CIN85 in both longitudinal (B) and lateral (C) views show a stable coiled-coil trimer, and it has been demonstrated with an ability to bind membrane lipids. Adapted from Kühn et al., 2016.

### 4.1.3 Aims of the SLP65-CIN85 LLPS Project

To address abovementioned questions, I set out:

1. To examine the SLP65-CIN85 LLPS with lipid vesicles by FLM and cryo-EM.
2. To accurately target the SLP65-CIN85 LLPS puncta in B cells with cryo-CLEM and correlative FIB milling, and then establish a reproducible cryo-ET workflow for the *in situ* analysis of SLP65-CIN85 LLPS.
3. To visualize and analyze the SLP65-CIN85 LLPS puncta in their native environments.

4. To decipher the ‘cellular sociology’ of the SLP65-CIN85 LLPS with other cellular components, especially vesicles, and then propose a novel mechanism by which SLP65 is efficiently translocated to the plasma membrane during B cell activation.

## 4.2 Results

This section presents both *in vitro* and *in situ* analysis of SLP65-CIN85 LLPS. The *in vitro* analysis was mainly conducted by FLM and cryo-EM, and the *in situ* analysis was performed with cryo-CLEM, cryo-FIB milling, and cryo-ET, including visualization of the LLPS region and deciphering the *in situ* structure of novel protein densities. The *in vitro* analysis has been published in Wong et al., 2020.

### 4.2.1 *In Vitro* Analysis of SLP65-CIN85 LLPS

To conduct a fast and direct analysis on SLP65-CIN85 LLPS, *in vitro* experiments were first conducted in collaboration with Dr. Leo E Wong. SLP65 and CIN85 of different concentrations were mixed with small unilamellar vesicles (SUVs) and checked by FLM and heteronuclear single quantum coherence (HSQC). The FLM data showed that the protein concentration threshold for both SLP65 and CIN85 LLPS was significantly reduced to a physiological level when SLP65 and CIN85 were mixed with SUVs (**Figure 41 A**). Separately, the HSQC data showed that SLP65 retained high fluidity when mixed with CIN85 and SUVs (**Figure 41 B**), evidencing that the droplets were in the liquid phase.

To further characterize the LLPS formed by SLP65-CIN85 complex and SUVs, the mixture was plunged on the EM grids for a closer inspection under TEM. The result showed a significant difference between the grids plunged with only SUVs and the grids plunged with SUVs mixed with SLP65-CIN85 at the physiological concentration. On the grids plunged with only SUVs, there were barely any SUVs clustered in the hole, while on the grids plunged with SUVs and SLP65-CIN85, SUVs were tightly clustered (**Figure 41 C**). To evaluate the clustered SUVs with SLP65-CIN85, tomograms were taken on those areas and segmented. The tomograms showed that SUVs were compactly concentrated in the LLPS and their distribution was stochastic (**Figure 42 A**). I then examined the distance between any two closest SUVs and the diameters of

segmented SUVs, and the analysis suggested an average surface-to-surface distance of 5nm and an average radius of 9.10 nm (Figure 42 B, C). This was consistent with previous studies where SLP65-CIN85 was reported to have a strong ability to bind to lipids and the tripartite SLP65-CIN85 LLPS was supported by highly curved small vesicles.

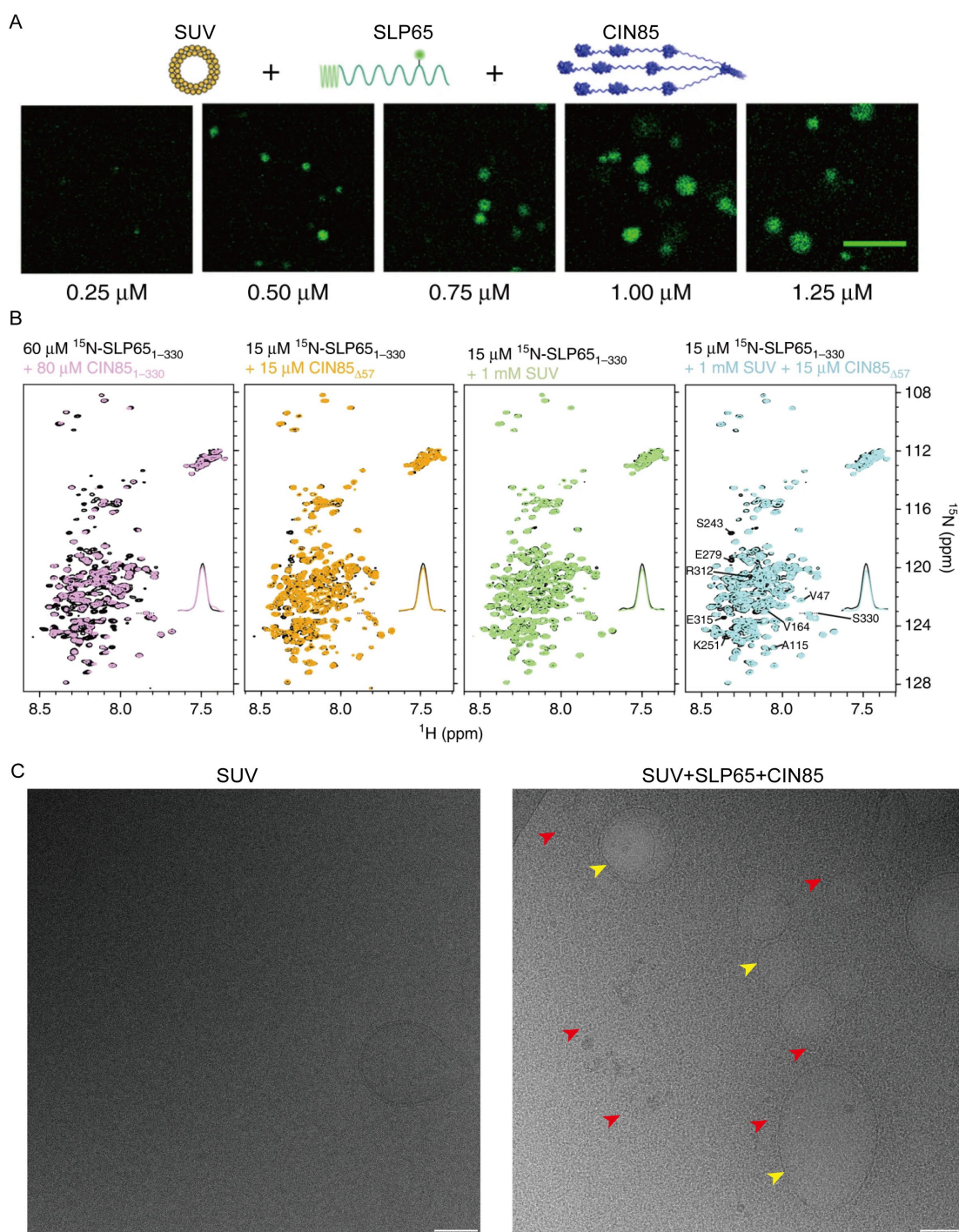


**Figure 41. *In vitro* analysis of SLP65-CIN85 LLPS.** (A) FLM images of SLP65-CIN85 LLPS. GFP-tagged SLP65 and CIN85 trimer were mixed with SUVs with a diameter of ~20 nm, LLPS

occurs at a physiological concentration of both proteins (0.5  $\mu\text{M}$ ). (B)  $^{15}\text{N}$ -HSQC spectra of  $^{15}\text{N}$ -labeled SLP65 in four conditions. High fluidity of SLP65 is shown in all conditions. Adapted from Wong et al., 2020. (C) TEM overviews of only SUVs and SUVs mixed with SLP65 and CIN85. Small vesicles are indicated by red arrowheads, gigantic vesicles are indicated by yellow arrowheads. Protein concentration = 1  $\mu\text{M}$ ; SUV concentration = 1 mM; Magnification = 34k; Scale bar = 100 nm.

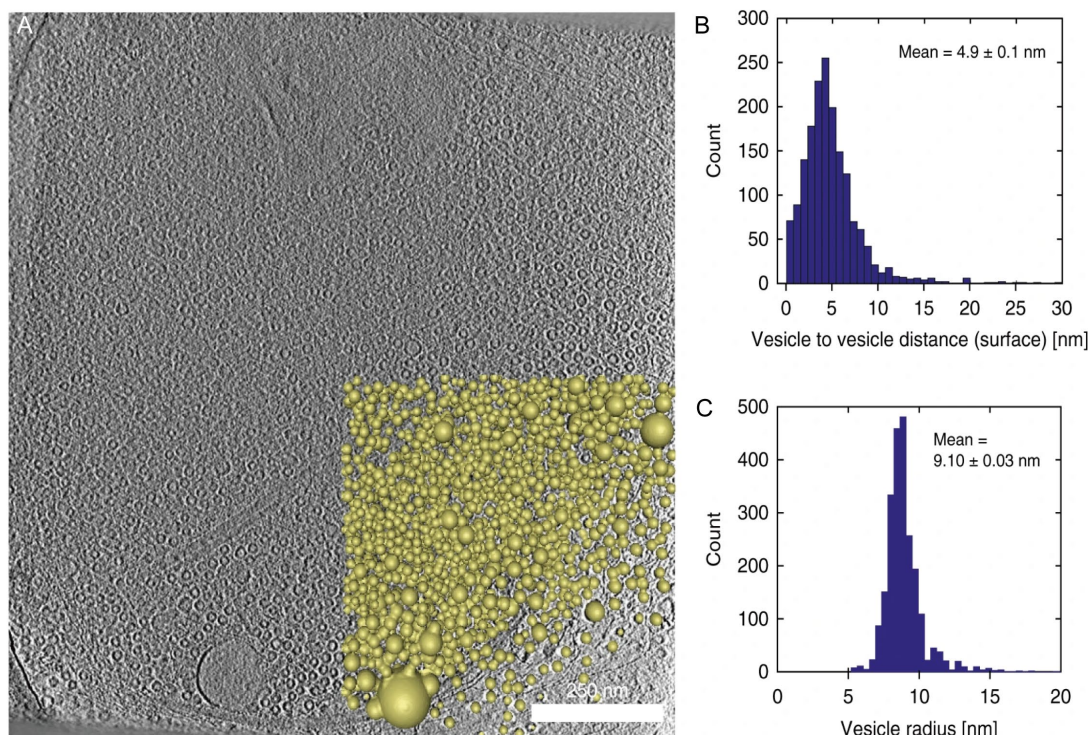


**Figure 42. Cryo-ET analysis of *in vitro* prepared SLP65-CIN85 LLPS.** (A) A representative slice from the tomogram of SLP65-CIN85 LLPS. A quarter of the tomogram is segmented with AMIRA 6.2 and processed with an in-house python script. SUVs are presented as golden spheres. (B) Histogram of distances between any two closest vesicles, the average distance is  $4.92 \pm 0.1$  nm (mean  $\pm$  SEM;  $n = 2349$ ). (C) The histogram of radii of segmented vesicles and the averaged radius is  $9.10 \pm 0.03$  nm (mean  $\pm$  SEM;  $n = 1718$ ).

#### 4.2.2 Correlative FIB Milling of SLP65-CIN85 LLPS

To perform the correlative FIB milling, SLP65 and CIN85 were constructed with GFP and RFP, respectively. The FLM data showed that SLP65 was expressed across the entire cell and formed a punctum at the periphery, while CIN85 formed a more condensed punctum but that punctum did not always show colocalization with the

SLP65 punctum (**Figure 43**), suggesting that the localization of this LLPS cannot be solely indicated by CIN85. On the other hand, there was no colocalization of SLP65-CIN85 with the ER that is the major membrane source of most vesicles (**Figure 43**).

To examine the fluorescence intensity in the cryogenic condition and prepare for subsequent correlative FIB milling, DT40 cells were plunged with auto-fluorescent dynabeads with a diameter of  $\sim 1 \mu\text{m}$ . Fluorescence was checked with cryo-CLEM. SLP65-CIN85 LLPS puncta could be clearly identified with a stronger fluorescent intensity and differentiated from the dynabeads (**Figure 44 A**), which was ideal for the following correlative FIB milling. In addition, a layered organization of these two proteins within the LLPS was indicated by the 3D fluorescence reconstruction of the LLPS where CIN85 was concentrated in the middle while SLP65 was less condensed and more at the periphery surrounding CIN85 (**Figure 44 B**).

Correlative FIB milling was then performed based on those images. The accurate position of LLPS was located with an in-house software 3D Correlation, and auto-fluorescent dynabeads were used to assist the correlation, especially in the Z dimension (**Figure 45 A, B**). The SEM image of milled lamella was then superimposed with the fluorescent image to confirm the XY position of LLPS on the lamella (**Figure 45 C**).

Next, the grid was transferred to the TEM, and tomograms were taken on the corresponding areas on lamellae after another round of correlation of TEM images with SEM images from FIB. From overviews of lamellae, distinct areas without any ribosomes and other organelles were identified, and their positions were highly correlated with the LLPS areas in the fluorescent image (**Figure 45 D, E**), confirming these areas to be the SLP65-CIN85 LLPS.

There are several distinctive features for SLP65-CIN85 LLPS: 1. The shape is amorphous; 2. The size ranges from 600 nm to 1000 nm in diameter along the longest axis; 3. It is electron-light and not occupied by any other organelles; 4. It is usually surrounded by membrane structures or vesicle-like structures, and in some cases, it is tightly wrapped by microtubules.

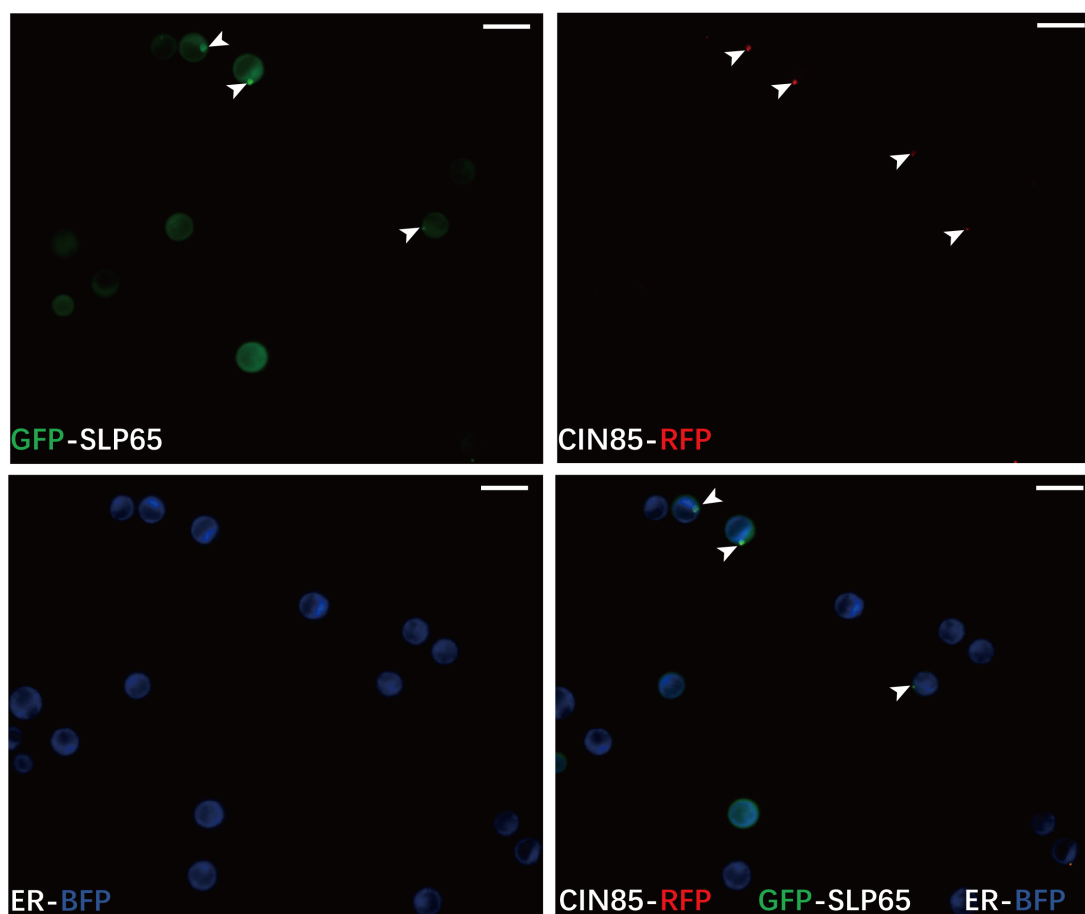


**Figure 43. FLM of SLP65-CIN85 LLPS in DT40 cells.** Living cells were incubated with a blue ER-tracker for 15 minutes and washed with PBS. SLP65-CIN85 puncta are indicated by white arrowheads. Images were taken in RFP, GFP, BFP channels. Magnification = 40x, exposure time = 250 ms, scale bar= 20  $\mu$ m.

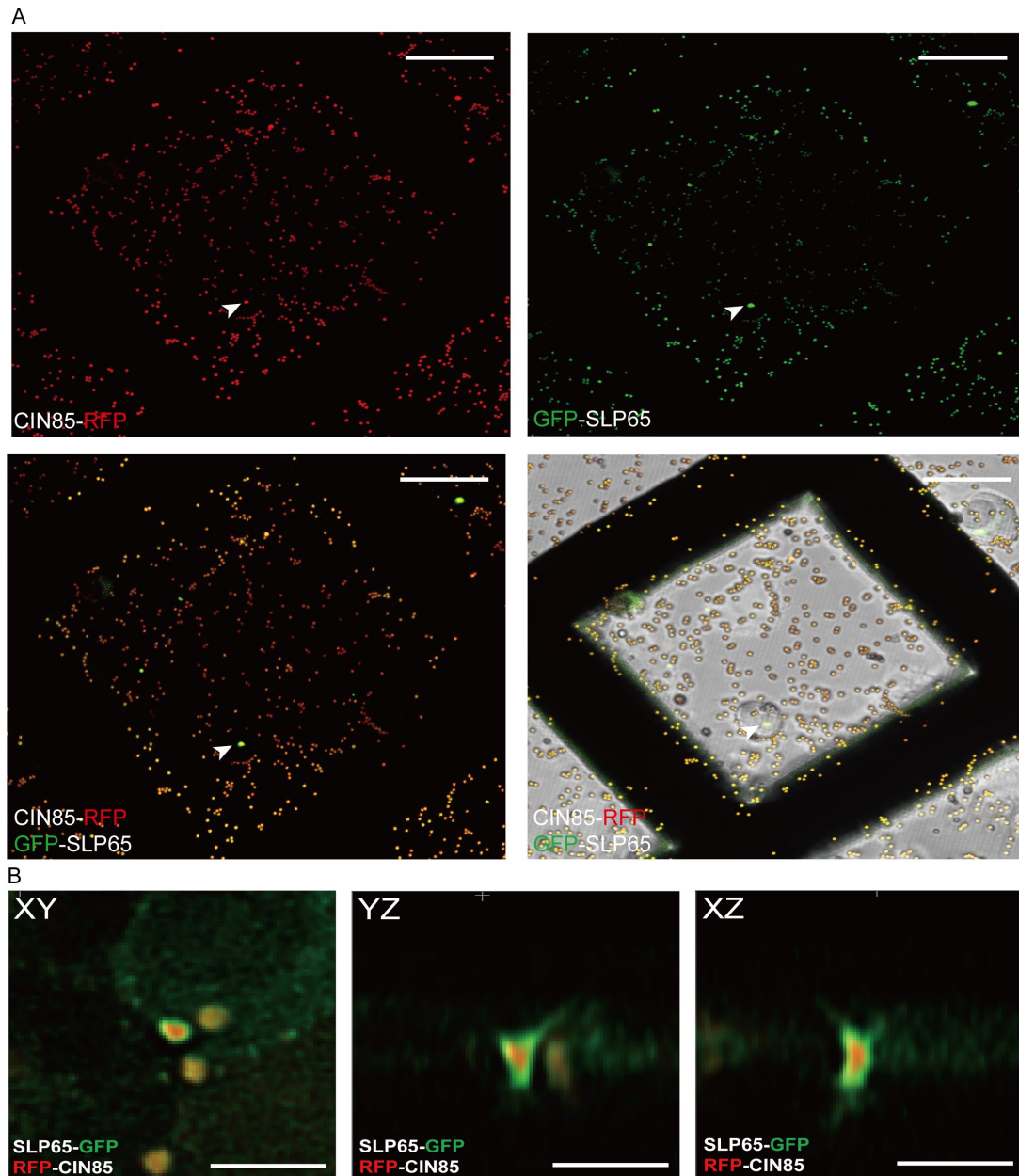


**Figure 44. Cryo-CLEM of SLP65-CIN85 LLPS.** (A) Four cryo-CLEM images of SLP65-CIN85 LLPS. SLP65-CIN85 LLPS is indicated by white arrowheads, other fluorescent dots are auto-fluorescent dynabeads. The exposure time was automatically optimized with the built-in auto mode. Z-stack images were taken in GFP, RFP, and BF channels with an increment of 100 nm along the Z axis. Scale bar = 20  $\mu$ m. (B) The 3D fluorescence reconstruction of SLP65-CIN85 LLPS by Huygens. The LLPS was viewed along the Z, X, and Y-axis, respectively. Images were deconvolved. Scale bar = 5  $\mu$ m.

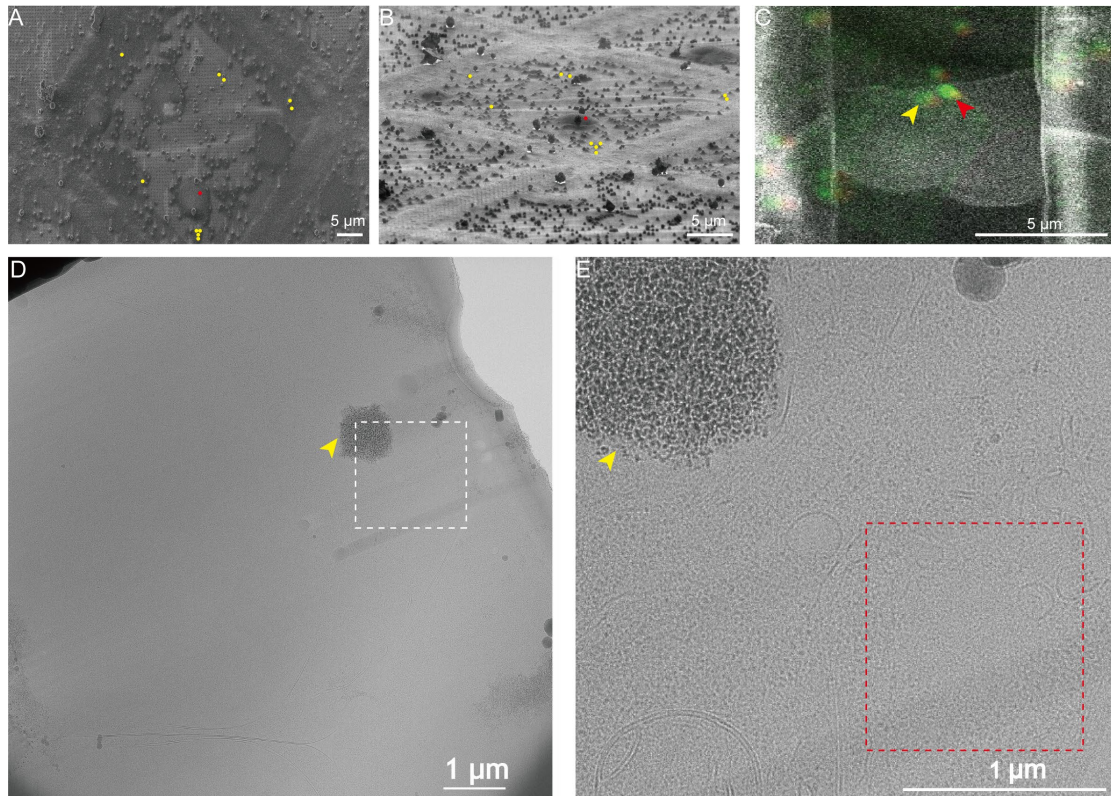


**Figure 45. Images for correlative FIB milling and TEM overview of SLP65-CIN85 LLPS.**

(A) SEM image of the correlated DT40 cell containing the LLPS at the magnification of 1000x. (B) FIB image of the correlated DT40 cell containing the LLPS at the magnification of 2000x. for (A) and (B), dynabeads used for 3D correlation are indicated by yellow dots, the correlated LLPS area is indicated by red dots. (C) Superimposed SEM image of the lamella with the fluorescent image from cryo-CLEM. The correlated LLPS area is indicated by the red arrowhead, the dynabead is indicated by the yellow arrowhead. (D) TEM overview of the lamella at the magnification of 6500x. The area framed by white dotted lines is enlarged as (E) for better visualization of the correlated LLPS area. The dynabead is indicated by the yellow arrowhead, and the correlated LLPS area is indicated by the red dotted frame.

### 4.2.3 *In Situ* Visualization of SLP65-CIN85 LLPS

Tomograms were recorded on the correlated areas at the magnification of 42000x and the pixel size was calibrated to be 3.52 Å/pixel. Then, tomograms were reconstructed in binned form (IMOD bin4, 14.08 Å/pixel) and denoised with CryoCare ([Buchholz, Jordan et al. 2019](#)). The denoised reconstructed tomograms depicted the morphology of SLP65-CIN85 LLPS with great detail (**Figure 46 A, B**). The LLPS area was electron-light and no obvious structures could be identified within, reflecting that the SLP65-CIN85 complex is intrinsically disordered. Ribosomes were always excluded from the LLPS areas; Mitochondria could be seen in its vicinity from most of the tomograms; ER was also sitting next to the LLPS and found protruding into it in some tomograms; The most interesting feature was that there are always various vesicles surrounding the LLPS, and the distribution of vesicles was polarized since they were always concentrated on one side but were barely seen on the other side of the LLPS.

To further characterize the LLPS area and define its border, I performed the template matching for ribosomes and matched ribosomes were then mapped back into the tomograms based on their coordinates. This analysis was carried out based on the computational algorithm without any subjective bias. The results showed that ribosomes were completely excluded from the LLPS and no small vesicles were found in the LLPS (**Figure 46 C**). Additionally, the LLPS area is much more electron-light than its vicinity and was then segmented with an automatic density generating function in Amira for a better visualization.

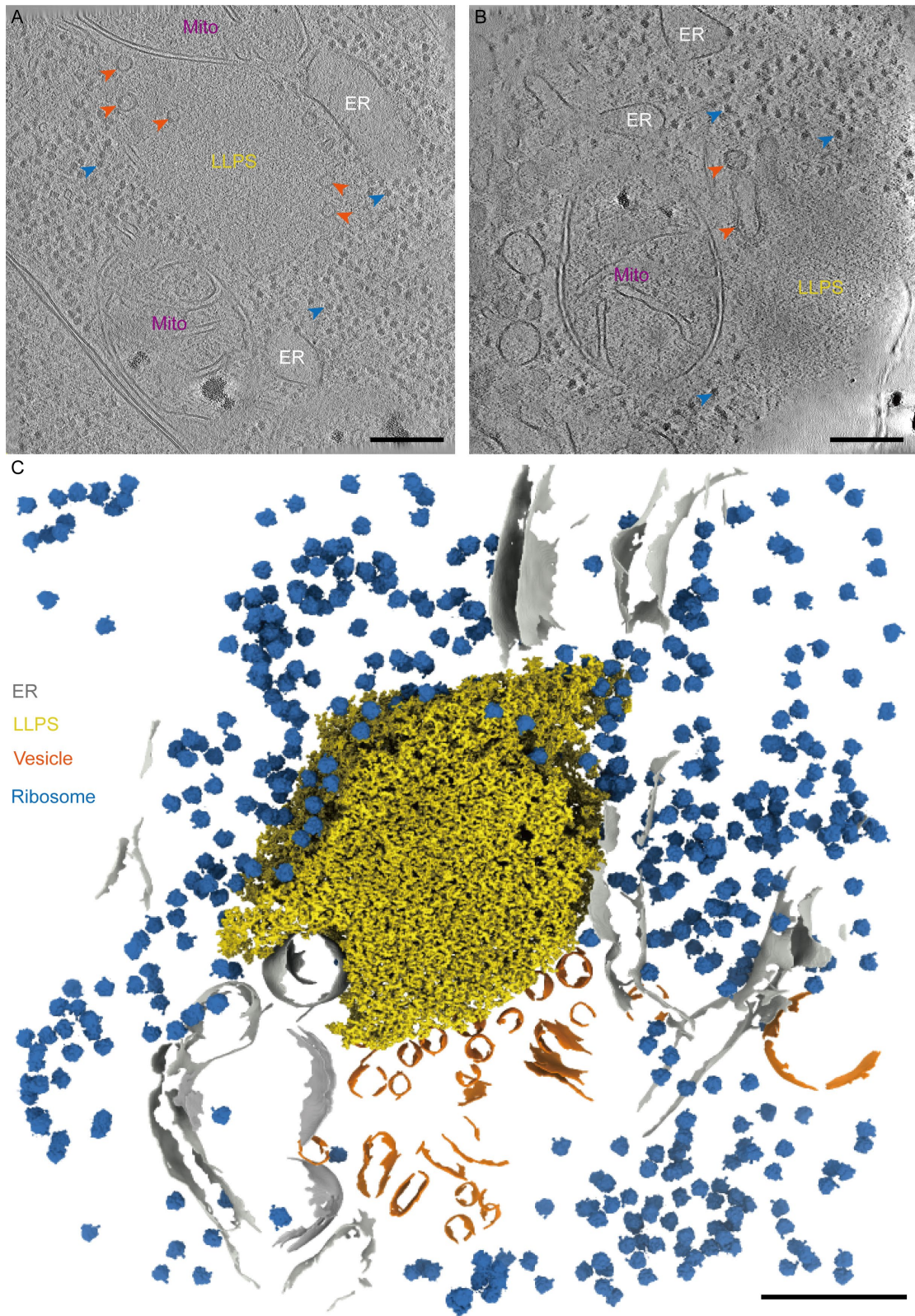


**Figure 46. Reconstructed and segmented tomograms of SLP65-CIN85 LLPS.** (A), (B) Two representative slices of two tomograms of SLP65-CIN85 LLPS. Ribosomes are indicated by blue arrowheads; vesicles are indicated by orange arrowheads. Mitochondrion (Mito). (B) The segmented tomogram of SLP65-CIN85 LLPS. Ribosomes are colored in blue, membrane

structures are illustrated in silver gray, vesicles are in orange, and the LLPS is presented in yellow. The segmentation was performed in AMIRA 6.2 with the aid of Pyseg. Scale bar = 250 nm.

#### 4.2.4 Characterization of LLPS-related Vesicles

Since the formation of SLP65-CIN85 LLPS requires the participation of lipid vesicles, I then analyzed the vesicles next to the LLPS and two major types of vesicles (**Figure 47 A**) were identified. The first type has a smooth membrane and its average size is smaller (diameter < 40 nm), while the second type is larger (diameter > 40 nm), and the inner side of its membrane is coated with densities that are speculated to be proteins.

I then performed a statistical analysis based on their features, and the result suggested a significant difference, indicating the existence of two kinds of vesicles (**Figure 47 B**). Following that, I set out to identify the inner-membrane-coated densities, I conducted STA on those densities along the segmented surface of vesicles. Particles were oversampled to ensure an adequate STA number. After several rounds of classifications and refinement, the results showed that there indeed existed undefined structures along the inner membrane and the size of the structure ranges from 6 nm to 8 nm (**Figure 47 C**). To validate the STA result of vesicle-associated densities, parallel STA was performed on ribosomes from the same tomograms. A ribosome structure was resolved at 30 Å and the final resolution of vesicle-associated densities was 35 Å. However, at this resolution, whether these structures are related to SLP65-CIN85 complexes cannot yet be determined.

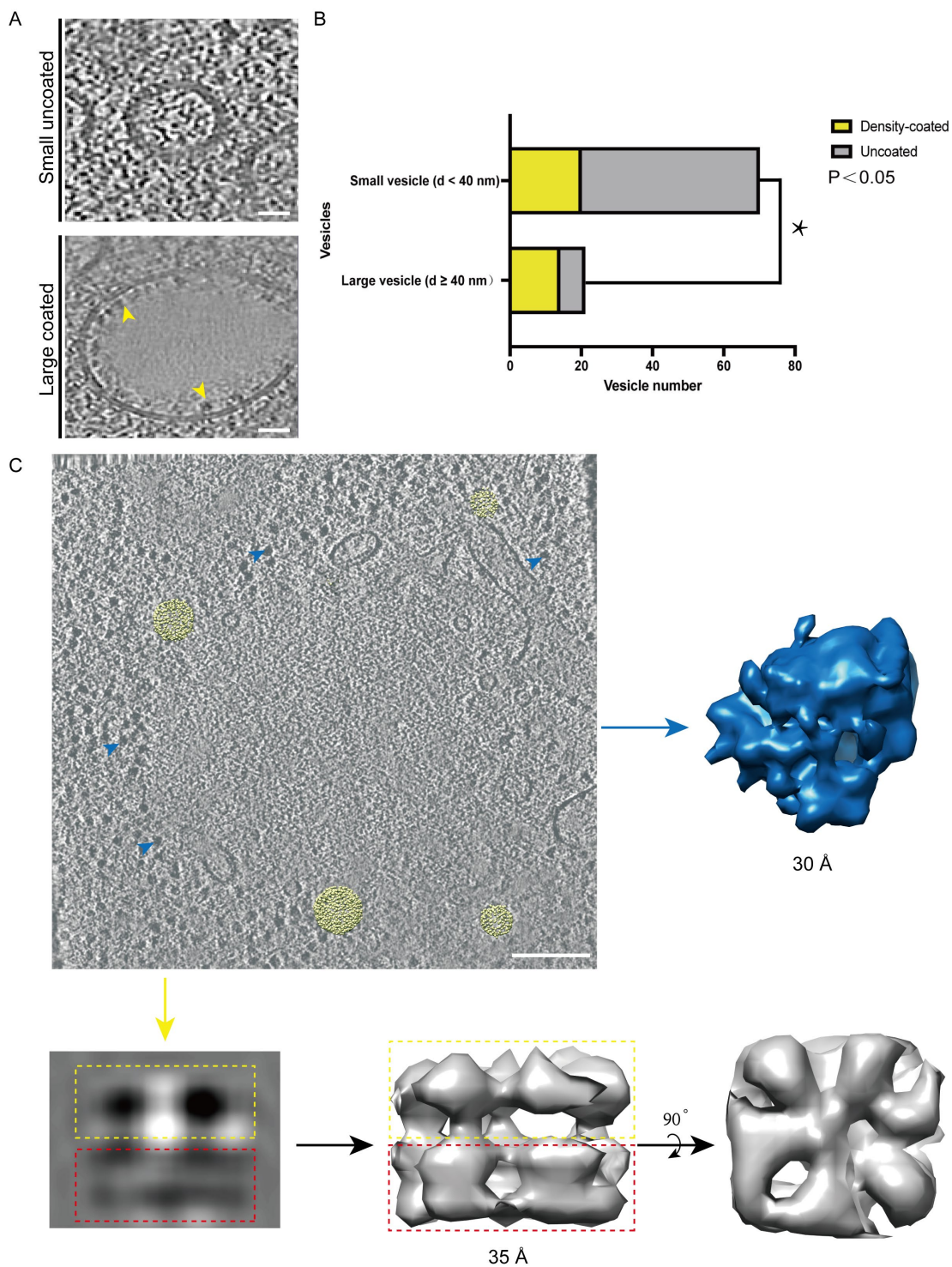


**Figure 47. Characterization of LLPS-related vesicles and vesicle-associated densities.**

(A) Tomogram slices of various vesicles. Vesicle-associated densities are indicated with yellow arrowheads. Scale bar = 5 nm (B) Histogram of comparison between two major types of vesicles. The number of vesicles was counted from 5 tomograms, and the total number of small vesicles is 57 while the total number of large vesicles is 21. Chi-square was conducted. \* Statistical significance. (C) Strategy for STA of the vesicle-associated densities at bin4.

Coordinates of vesicle-associated densities were obtained from the surface of segmented vesicles. Vesicle-associated densities are indicated as small yellow spheres in the tomogram and yellow dotted frames on the *in situ* structure. Ribosomes are indicated by blue arrowheads in the tomogram. The lipid layer is indicated by red dotted frames. Visualization was performed in IMOD and Chimera. Scale bar = 250 nm.

### 4.3 Discussion

In this project, I successfully conducted both *in vitro* and *in situ* analysis on the SLP65-CIN85 LLPS at a high resolution. The tomograms of *in vitro* samples indicate a strong relationship between the SLP65-CIN85 complex and lipid vesicles. Smaller vesicles are preferred in the LLPS.

Separately, the *in situ* visualization of SLP65-CIN85 LLPS areas provides us with unprecedented and unperturbed cellular information of this LLPS. The LLPS is naturally in an amorphous shape and it has a close contact with many cellular components, especially with vesicles. These vesicles are believed to play a pivotal role in the translocation of SLP65 from the LLPS to the plasma membrane since many proteins are transported in vesicle-assisted ways, with examples including the COPI- and COPII-associated proteins that are trafficking between ER and Golgi apparatus. Moreover, the *in situ* data also showed different vesicle populations around the LLPS, suggesting various states of the vesicles depending on their current functions, e.g., loading, unloading, and protein folding, which could hardly be illustrated by conventional biochemistry and FLM. Furthermore, the polarized distribution of vesicles also indicated a highly dynamic model where vesicles were speculated to move towards the LLPS unilaterally from one side for translocating the proteins and ribosomes on the other side of the LLPS are were proposed to synthesize the proteins in a large amount.

Although both *in vitro* data and *in situ* data give us valuable information, the LLPS models suggested by them are quite different (**Figure 48**), reflecting that *in vitro* data cannot perfectly recapitulate what takes place in the cell. In the model suggested by *in vitro* experiments, SLP65-CIN85 LLPS is a promiscuous cellular compartment with heavily condensed vesicles while the *in situ* model depicts a liquid-phase cellular

compartment without any organelles but with a few vesicles surrounding it. Therefore, cryo-ET is a powerful tool for us to improve the understanding of LLPS and their genuine biological relevance.

However, no detailed structural information for the SLP65-CIN85 complex could be determined in my study as the vesicle-associated densities were at low resolution, based on which no convincing structural fitting could be performed. This prevented me from further understanding the function of SLP65-CIN85 LLPS in regulating SLP65 and its translocation during B cell activation.

Apart from that, to understand the hierarchical organization of SLP65 and CIN85 observed in the 3D fluorescence reconstruction, other identifiable structures can be introduced to aid the visualization of distributions of SLP65 and CIN85 in tomograms. For instance, fused structures of SLP65 and CIN85 with GEMs, as described in the subcellular localization in NSD project, may be constructed. In addition, other critical information for the dynamic translocation of SLP65 is still missing as cryo-ET is performed on frozen samples and the dynamics of SLP65-CIN85 LLPS cannot be captured in this case. Therefore, super-resolution fluorescence microscopy and time-resolved cryo-ET may be adopted for the next step to visualize the vesicles-assisted protein translocation.

Taken together, my study on SLP65-CIN85 LLPS corroborates that LLPS is effectively involved, with other cellular compartments, in regulating protein surveillance and translocation. In parallel, this study also demonstrates that cryo-ET is a powerful tool to study LLPS and it provides exclusive information on the detail of the ‘cellular sociology’ of LLPS, largely expanding our understanding of LLPS and their critical functions in multiple life processes.

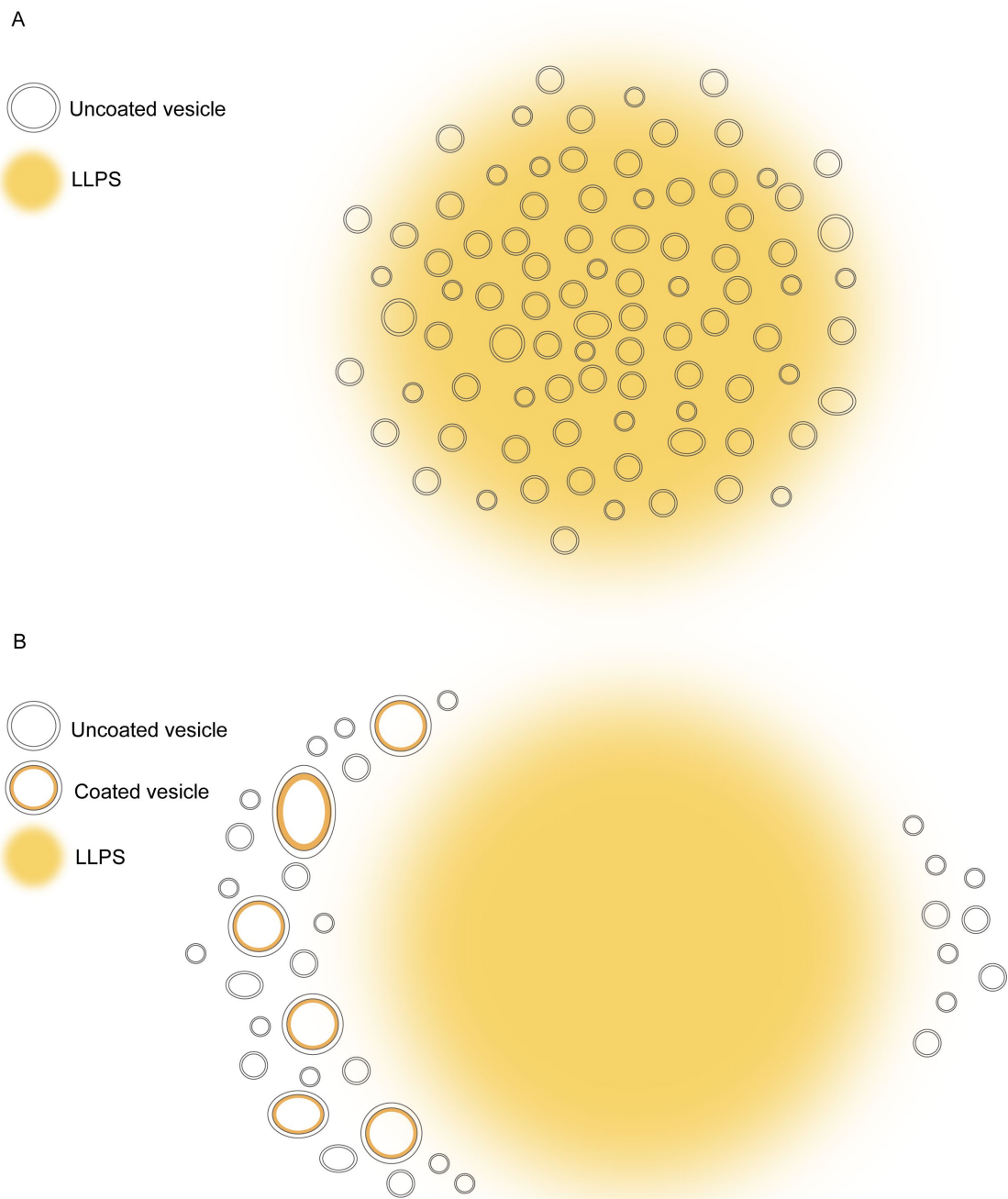


**Figure 48. SLP65-CIN85 LLPS models.** (A) The hypothesized *in vitro* model of SLP65-CIN85 LLPS, in which SLP65 and CIN85 form an unstructured protein network tethering vesicles and vesicles are evenly distributed. (B) The hypothesized *in situ* model of SLP65-CIN85 LLPS featuring two different kinds of vesicles and the polarized distribution of them.

## 5. Methods and Materials

In this chapter, methods for sample preparation of each project are described in detail and materials are listed accordingly. For the data analysis, standard procedures of cryo-EM and cryo-ET are stated.

### 5.1 Yeast Culture and Strains

The yeast used in the ribosome biogenesis study is *Saccharomyces cerevisiae* strain W303 wild type. Yeasts were plated on YPD agar plates supplemented with 2% glucose, and a single colony was picked followed by the inoculation into YPD medium supplemented with 2% glucose for an overnight culture at 30°C. After the overnight culture, yeast cells were diluted to OD<sub>600</sub> = 0.1-0.2 and harvested at OD<sub>600</sub> = 0.6-0.8.

The yeast used in the NSD study was *Saccharomyces cerevisiae* strain W303 with genomic modifications listed below:

Table 1: List of the yeast strains.

Strain name	Original strain	Genomic background	Transformed plasmid(s)
Ski7 <sup>wt</sup>	<i>S. cerevisiae</i> W303	<i>hbs1Δ ski7Δ</i>	p413GPD-Ski7 <sup>wt</sup> p425GAL-Pgk1 <sup>NSD</sup>
Ski7 <sup>C-</sup>	<i>S. cerevisiae</i> W303	<i>hbs1Δ ski7Δ</i>	p413GPD-Ski7 <sup>C-</sup> p425GAL-Pgk1 <sup>NSD</sup>
Ski7 <sup>N-</sup>	<i>S. cerevisiae</i> W303	<i>hbs1Δ ski7Δ</i>	p413GPD-Ski7 <sup>N-</sup> p425GAL-Pgk1 <sup>NSD</sup>
Ski7 <sup>ExoMut-</sup>	<i>S. cerevisiae</i> W303	<i>hbs1Δ ski7Δ</i>	p413GPD-Ski7 <sup>ExoMut-</sup> p425GAL-Pgk1 <sup>NSD</sup>
GEM40-Ski7 <sup>C-</sup>	<i>S. cerevisiae</i> W303	<i>Wild type</i>	pRS415-GEM40-Ski7 <sup>C-</sup>
GEM20-Ski7 <sup>C-</sup>	<i>S. cerevisiae</i> W303	<i>Wild type</i>	pRS415-GEM20-Ski7 <sup>C-</sup>

## Methods and Materials

GEM20-Ski7 <sup>wt</sup>	<i>S. cerevisiae</i> W303	<i>Wild type</i>	pRS415-GEM20-Ski7 <sup>wt</sup>
GEM40-Ski7 <sup>c<sup>-</sup></sup>	<i>S. cerevisiae</i> W303	<i>hbs1Δ ski7Δ</i>	pRS415-GEM40-Ski7 <sup>c<sup>-</sup></sup>
GEM20-Ski7 <sup>c<sup>-</sup></sup>	<i>S. cerevisiae</i> W303	<i>hbs1Δ ski7Δ</i>	pRS415-GEM20-Ski7 <sup>c<sup>-</sup></sup>
GEM20-Ski7 <sup>wt</sup>	<i>S. cerevisiae</i> W303	<i>hbs1Δ ski7Δ</i>	pRS415-GEM20-Ski7 <sup>wt</sup>
GPA1N9-Ski7 <sup>wt</sup>	<i>S. cerevisiae</i> W303	<i>hbs1Δ ski7Δ</i>	pRS415-GPA1N9-Ski7 <sup>wt</sup>
GPA1N9	<i>S. cerevisiae</i> W303	<i>Wild type</i>	pRS415-GPA1N9
GEM40	<i>S. cerevisiae</i> W303	<i>Wild type</i>	pRS415-GEM40
GPA1N9-Rpn5	<i>S. cerevisiae</i> W303	<i>Wild type</i>	pRS415-GPA1N9-Rpn5
GPA1N9-Rrp44	<i>S. cerevisiae</i> W303	<i>Wild type</i>	pRS415-GPA1N9-Rrp44
GPA1N9-Pgk1	<i>S. cerevisiae</i> W303	<i>hbs1Δ ski7Δ</i>	p425GAL-GPA1N9- Pgk1 <sup>NSD</sup>

**For the subcellular localization of NSD**, Pgk1, Ski7, Rrp44, and Rpn5 were fused with GPA1N9 and mApple, and Ski7 was fused with GEM40 and yEGFP. Strep-tag and FLAG-tag were constructed for subsequent biochemical analysis into the sequences as shown in the results.

**For NSD induction**, yeast cells were selected on synthetic minimal (SD)-Leu agar plates supplemented with 2% raffinose, and a single colony was picked and inoculated into the SD-Leu medium supplemented with 2% raffinose for an overnight culture at 30 °C. After the overnight culture, yeast cells were diluted to, yeast cells were diluted to OD<sub>600</sub> = 0.1-0.2 and 2% galactose was induced when the OD<sub>600</sub> reached above 0.6 followed by 2-, 4-, 6-, 8-, 10-, 12-, 14-, and 16-hour incubations for galactose induction. After the galactose induction, yeast cells were measured on OD<sub>600</sub> and collected for successive experiments.

Below are recipes for YPD agar plates, YPD medium, SD-Leu agar plates, and SD-Leu medium:

<b>YPD agar plates/medium</b>	
Bacto agar	10g for plates/0g for medium
Yeast extract	5 g
Bacto peptone	10 g
Water	500 ml

<b>SD-Leu agar plates/medium</b>		<b>100x Tryptophan</b>	
Bacto agar	10g for plates/0g for medium	Tryptophan	0.4 g
Yeast nitrogen base without amino acids	10 g	Water	100 ml
Sigma drop out media (without Leu, His, Trp)	0.73 g		
100x Tryptophan	5 ml	<b>100x Histidine</b>	
100x Histidine	5 ml	Histidine	0.24 g
Water	490 ml	Water	100 ml

## 5.2 DT40 B lymphocytes Cell Culture

DT40<sub>slp65-/-</sub> B lymphocytes expressing GFP-SLP65 and CIN85-RFP were cultured in RPMI1640 (Merck) medium supplemented with 10% fetal calf serum (FCS), 50  $\mu$ M Beta mercaptoethanol, 1 mM sodium pyruvate, 50  $\mu$ g/ml penicillin, and 50  $\mu$ g/ml streptomycin at 37 °C and a CO<sub>2</sub> concentration of 5% for 8 hours and collected with a density ranging from 10<sup>5</sup> to 2x10<sup>6</sup> cells/ml. Before plunging, cells were centrifuged at 1200 rpm for 5 minutes and concentrated with a 2-fold cell density.

## 5.3 Chlamydomonas Culture and Strains

Chlamydomonas reinhardtii strain mat3-4 (CC3994) was used in the ribosome biogenesis study. This strain was acquired from the Chlamydomonas Resource Center, University Minnesota, MN and has a smaller growth phenotype<sup>43</sup>. Unless otherwise stated, cells were agitated at 100 rpm.

From a plate culture, a liquid culture was inoculated in 40 ml of Tris-acetate phosphate (TAP) media (0.02 M Tris base, TAP salts (7.00 mM NH<sub>4</sub>Cl, 0.83 mM, MgSO<sub>4</sub>, 0.45 mM CaCl<sub>2</sub>), Phosphate buffer (1.65 mM K<sub>2</sub>HPO<sub>4</sub>, 1.05 mM KH<sub>2</sub>PO<sub>4</sub>), Hunter trace elements (0.134 mM Na<sub>2</sub>EDTA, 0.136 mM ZnSO<sub>4</sub>, 0.184 mM H<sub>3</sub>BO<sub>4</sub>, 40 μM MnCl<sub>2</sub>, 32.9 μM FeSO<sub>4</sub>, 12.3 μM CoCl<sub>2</sub>, 10.0 μM CuSO<sub>4</sub>, 4.44 μM (NH<sub>4</sub>)<sub>6</sub>MoO<sub>3</sub>, 17.5 mM acetic acid)) and agitated at 100 rpm. Cells were under a constant illumination (~90 μmol photons/m<sup>2</sup>s) in normal atmosphere, and harvested 48–72 hours after the inoculation. To obtain a log phase culture, cells were allowed to continue growing for seven days without any dilution and cells were treated with diazaborine (DAZ, 370 μM, Merck) for 2 h before plunge freezing.

From a log-phase culture (24 h), a sample was taken and transferred to 40 ml of fresh TAP media. Cells were subsequently cultured in an isolated grow box with electrically controlled illumination using a 12 h/12 h day/night cycle. Every 2-3 days, the cell density was adjusted during the day period to ~1000 cells/μl by manually diluting the sample with fresh TAP. This was maintained for three such cycles. Finally, cells were harvested after 4 hours of initiating the dark cycle.

### 5.4 Western Blot

To examine the expression level of PGK1-NSD, GEM40/20-Ski7, GPA1N9-fused proteins, western blot was performed against FLAG-tag and GFP respectively. For each sample, 10 ml of yeast cells were harvested at OD<sub>600</sub> = 0.6-0.8 and centrifuged at 3000 rpm for 2 minutes. And then the pellet was washed with 1 ml of distilled water and centrifuged at 3000 rpm for another 2 minutes. After the washing, cells were resuspended with 0.3 M NaOH and incubated for 10 minutes at room temperature followed by the removal of supernatant. Subsequently, yeast cells were resuspended with 70 μl of SDS and boiled at 95 °C for 3 minutes.

Once the protein was denatured, it was subjected to the SDS-PAGE with the running buffer (25 μM Tris base, 200 μM Glycine, 0.01% SDS), and the gel was then transferred to the nitrocellulose membrane with the blotting buffer (20 μM Tris base, 150 μM

Glycine, 0.01% SDS, 5% Ethanol) for 1 hour at 4 °C. And then, the membrane was incubated with the blocking buffer (PBS buffer with 3% BSA and 0.05% v/v Tween 20) at 4 °C for 1 hour and then washed three times (5 minutes each) with PBS buffer supplemented with 0.1% v/v Tween 20.

The washed membrane was incubated with the primary anti-GFP antibody (1:1000) (Sigma-Aldrich)/primary anti-FLAG antibody (1:5000) (Sigma-Aldrich) overnight and then washed three times with the washing buffer. Subsequently, the membrane was incubated with the secondary antibody HRP-conjugated anti-mouse antibody (1:10000) (Bio-Rad) for 1 hour at room temperature. At last, the membrane was washed three times with the washing buffer and exposed to the peroxidase substrate solution, and images were taken with the ImageQuant LAS4000 imaging system.

### 5.5 Pull-down Assay

Before being milled by the Cryomill machine, yeasts were inoculated into 1 L of YPD/SD-Leu medium followed by an overnight culture at 30 °C under constant shaking at 200 rpm. Yeasts were then filtered and harvested at OD=0.6-0.8; yeast slur was immediately submerged into liquid nitrogen and subjected to the Cryomill machine for grinding. The total yielded yeast powder approximated 2 ml and the yeast powder was then dissolved in the buffer P50 (47 mM K<sub>2</sub>HPO<sub>4</sub>, 3 mM KH<sub>2</sub>PO<sub>4</sub>, 0.1% NP40, pH 8.0) supplemented with the protease inhibitor and Benzonase.

**For anti-Strep pull-down**, M270-StrepTactin beads were used. 50 µl of M270-StrepTactin beads were aliquoted for each sample and washed with 1 ml buffer P50 before being mixed with the lysates. Subsequently, the beads were added to the lysates, and the mixture was incubated at 4 °C on a rotator for 30 minutes. After the incubation, the mixture was put on the magnetic rack and the supernatant was aspirated out and preserved, followed by three times of washing with 1 ml of buffer P50. Ultimately, the beads were incubated with 20 µl of SDS buffer on ice for 15 minutes and then boiled at 95 °C for 5 minutes.

**For anti-GFP pull-down**, firstly, the protein-G beads were equilibrated in which 50  $\mu$ l of protein-G beads were incubated with 1  $\mu$ l of GFP antibody in 500  $\mu$ l of buffer P50 at 4 °C for 20 minutes and washed with 1 ml of buffer P50 for three times. And then, the equilibrated beads were incubated with the cell lysates at 4 °C on a rotator for 30 minutes. After the incubation, the mixture was placed on the magnetic rack and the supernatant was preserved. Subsequently, the beads were washed three times with 1 ml of buffer P50 and then mixed with 20  $\mu$ l of SDS buffer followed by an incubation of 15 minutes. Finally, the mixture was boiled at 95 °C for 5 minutes before being subjected to SDS-PAGE.

**For TCA precipitation**, 200  $\mu$ l of flow through preserved after the initial incubation of cell lysates with beads was incubated with 10% (v/v) of trichloroacetic acid (TCA) on ice for 15 minutes. After that, the sample was spined for 10 minutes at 18000 g at 4 °C followed by a wash with 300  $\mu$ l of ice-cold acetone. Then the washed sample was centrifuged at 18000 for another 2 minutes and dried out at 37 °C. Ultimately, the sample was mixed with 20  $\mu$ l of SDS buffer.

### 5.6 Plunge Freezing

To fix the sample for FIB milling, plunge freezing was performed by the Vitrobot® Mark 4 (Quantifoil). Prior to the plunge, cells were well vortexed for 8 seconds for the homogeneity and fluorescent dynabeads (Thermo Fisher) were added to the cell with a dilution of 1:20 for the later 3D correlation. For each blot, 4  $\mu$ l of cells ( $OD_{600} = 0.6-0.8$  for yeast cells) / ( $2 \times 10^5 - 2 \times 10^6$  cells /ml for DT40 B lymphocytes) was applied onto glow-discharged holey carbon-coated copper (R 2/1, 200 mesh)/silicon oxide grids (R 1/4, 200 mesh) (Quantifoil). After that, the grids were directly blotted with a Teflon sheet on the cell side and a filter paper on the other side. The blotting was performed at 30 °C/37 °C in 90% humidity for 10 seconds with a blot force 10 and a drain time of 1 second. In the end, grids were immediately plunged into the liquid ethane/propane mixture cooled by the liquid nitrogen.

### 5.7 FLM

To check the expression pattern and level of fluorescence-tagged proteins, yeast cells ( $OD_{600}=0.6-0.8$ ) and DT40 B lymphocytes ( $2 \times 10^5-2 \times 10^6$  cells/ml) were checked with the CorrSight system (FEI) at room temperature. 200  $\mu$ l of cells were aliquoted from the cell solution and applied to the imaging dish ( $\mu$ -Dish 35 mm high) (Ibidi) without any fixation. After 2-3 minutes (for sedimentation), cells were exposed in both GFP channel and RFP channel with an exposure time of 500 ms and pictures were taken.

### 5.8 Cryo-CLEM and 3D Correlation

Grids of yeast cells and DT40 B lymphocytes were examined by the CLEM system (FEI) to target the yeast cells with a high expression of NSD reporter and the LLPS in DT40 B lymphocytes. Images were acquired in the cryogenic condition and both 488 nm laser and 556 nm laser were activated for GFP and RFP signals, respectively. Exposure time and pixel size (110 nm on the X and Y axis) were set using the auto-optimization mode. Z stacks were made for DT40 cells for the successive 3D correlation, and the increment of Z was set as 100 nm. In addition, the top and bottom were set manually by adjusting the Z height. Images were later processed with the software Huygens (SVI) for deconvolution.

### 5.9 FIB Milling (Standard and Correlative)

Vitrified cells were further processed by FIB for the preparation of lamellae. To monitor the milling process, a dual-beam FIB microscope FIB Scios (FEI) and FIB Aquilos (FEI) equipped with a complete cryo-system prototyped by FEI and a rotatable cryo-stage cooled by an open nitrogen circuit. Before the FIB milling, grids were fixed in Autogrids (FEI) with C rings clipped into the dent of Autogrids. Autogrids used in all projects were home-modified with a lower cutout on one side of the Autogrid for a larger FIB milling view. And then, the fixed sample was mounted into a shuttle in liquid nitrogen and transferred into the FIB chamber using the cryo-transfer system. Samples were then coated with an organometallic Pt layer using the GIS system on the opposite side of the cutout of the Autogrids. The GIS temperature was heated to 26-28 °C before

the flow was started and the coating time approximated 6-8 seconds.

For the standard milling without correlation, positions were chosen around the center of the grid and no FIB images were taken for the positions before the milling. But for correlative FIB milling, positions were chosen according to the deconvoluted CLEM images and SEM and FIB images were both taken for each position for the 3D correlation performed with a house-invented software 3D Correlation.

To make an evenly milled and thinner lamella, pre-milling was performed at a pre-tilted angle of 18-20°. In this pre-milling process, firstly, the front and back areas of the target were cleaned with 0.3 nA ion beam current, and two parallel trenches were made to ease the bending pressure. But the trenches were not made in the case of correlative FIB milling. And then, the target cell or cell cluster was exposed to the ion beam of 100 pA for the rough milling until the remaining thickness approximated 800 nm. A smaller ion beam current ranging from 30-50 nA was then applied for the fine milling, and the lamellae with a thickness of 100-180 nm were finally polished with the ion beam of 10 pA on the top and bottom. The thickness and homogeneity were monitored using the Everhart-Thornley detector (ETD).

### 5.10 Cryo-EM and Cryo-ET

**For the ribosome biogenesis project, Chlamydomonas grids** containing milled lamellae were firstly transferred into the specimen stage by the autoloader system of a transmission electron microscope Titan Krios (FEG 300kV, FEI) equipped with a direct detection camera (K2 Summit, Gatan). Raw tilt series of tomograms were recorded with a defocus range of -5  $\mu\text{m}$  to -3  $\mu\text{m}$  at the magnification of 42000x where the calibrated pixel size is 3.42 Å. In total, 85 tomograms were collected, 21 of which were acquired with a bi-directional scheme from -50° to 70° with an increment of 2° per tilt, in which the first branch was done from -20° to 70° and the second branch was collected from -22° to -50°, and the rest tomograms were recorded with the dose symmetric scheme in which angular tilts were from 70° and -50° starting at 10° to compensate for the lamella pre-tilt generated in FIB milling (~10-12° based on the previous calibration).

**As for yeast grids**, the first batch of tomograms (15 tomograms) was recorded with a

TEM Polara 2 (FEG 300 kV, FEI), and the transferring process was conducted with a manual loading system consisting of a multi-specimen rod (FEI), cryo-pump (FEI), and an insertion rod (FEI). Polara 2 was also equipped with a direct detection camera (K2 Summit, Gatan). The data collection in Polara was performed using the bi-directional scheme as described for the tomograms of *Chlamydomonas*. The second batch of tomograms (25 tomograms) was collected with Titan Krios using the dose symmetric scheme described above.

**In the SLP65-CIN85 LLPS and NSD projects**, data collection was performed with Titan Krios using the dose symmetric scheme described above. For the SLP65-CIN85 project, 45 tomograms were taken in total, while 64 tomograms were taken for the NSD project.

### 5.11 Tomogram Reconstruction

Recorded movie frames of all tomograms were aligned with an in-house algorithm called motioncorr 2, where the shifts among frames due to stage drift and movement were calculated and corrected. And the contrast transfer function (CTF) was estimated using CTFFIND4. After that, raw stacks were assembled and preprocessed with the Matlab-based script Tomoman before the reconstruction.

Pre-processed tilt series were aligned using the patch tracking function of the IMOD software package and reconstructed by weighted-back projection. In the case of bulk ice contamination on the surface of some slices or low SNR, corresponding slices were removed from the stack. Tomograms were reconstructed in binned form and the binning power applied in all projects for successive template matching was 4. Reconstructed tomograms were then denoised with CryoCare for better visualization.

### 5.12 Template Matching

**For yeast preribosomes**, a published SPA yeast 90s preribosome structure (PDB: 5WYJ) was downloaded from The Electron Microscopy Data Bank (EMDB) and low-pass filtered with a final pixel size of 13.68 Å/pixel. This filtered structure was then used as the initial template for the template matching conducted on tomograms recorded

from Polara 2 using PyTOM.

To achieve a less-bias result, the initial template for the template matching on tomograms recorded from Krios was generated by averaging 500 manually picked nucleolar particles using PyTOM. And top 500 hits were chosen and extracted from each tomogram for alignment and classification.

**For *Chlamydomonas preribosomes***, 300 nucleolar particles were manually picked from 4x binned tomograms and averaged using PyTOM as the initial template, and top 600 hits were extracted from each tomogram.

After the initial classification, truncated SSU and LSU references were generated by masking out part of the whole density for another round of template matching. The template matching was performed individually for SSU and LSU, and 400 hits were extracted from each tomogram.

**For 80S ribosomes of yeasts and DT40 B lymphocytes**, 500 cytoplasmic ribosome-like particles were manually picked from 4x binned tomograms and averaged using PyTOM as the initial template and top 1500 hits were extracted from each tomogram.

### 5.13 STA

**For yeast preribosomes**, the initial classification was carried out in 4x binned form in Relion 2.1 without CTF correction for the tomograms taken in Polara 2. The initial class number was set to 10, and 25 iterations were performed. The following refinement was conducted in Relion 2.1 and in bin4 with 25 iterations.

For tomograms taken in Krios, the initial classification was carried out in 4x binned form to clean out junk particles in Relion 2.1 without CTF correction, and 10 classes were set with 25 iterations. After the cleaning, the remaining particles were re-extracted from unbinned tomograms, and the classification was performed in Relion 2.1 with CTF correction. The class number was set to 10 and 25 iterations were applied, followed by the refinement with 25 iterations and a restricting mask.

**For *Chlamydomonas preribosomes***, the initial classification was performed with unbinned particles and CTF correction was applied. Iteration number was set to 25 and

16 classes were obtained after the classification, of which SSU and LSU were identified as two different classes and refined individually with 25 iterations in Relion 2.1.

After the second round of individual template matching, extracted particles were subjected to an initial classification with 40 classes in 4x binned form. And classes with the regrowth of the truncated density were then chosen, and corresponding particles were re-extracted from unbinned tomograms for another round classification. Subsequently, unbinned particles were averaged and subjected to the sub-classification of 6 classes with CTF correction and 25 iterations in Relion 2.1.

**For NSD 80S ribosomes**, unbinned particles were collectively averaged and subjected to the initial classification with 10 classes and 25 iterations, and CTF was not applied. After cleaning junk particles, the remaining particles were re-extracted from unbinned tomograms and subjected to another round of classification of 10 classes with CTF correction and 25 iterations. The classes with extra densities were selected and averaged with a new particle list with which the sub-classification was performed with 10 classes and 25 iterations and CTF correction. Subsequently, the cleaned particles were subjected to refinement with a restricting mask in Relion 2.1. To perform the focused classification, a mask was created around the area of interest and applied in successive classification and refinement in Relion 2.1. Data were processed with Warp and *M* in parallel.

**As for subtomograms derived from the vesicle-associated density in the SLP65-CIN85 project**, particles coated on the vesicles were extracted from the binned tomograms using STOPGAP-specified functions followed by the alignment of particles in STOPGAP.

### 5.14 Sphere Fitting

To measure the distribution of SSU and LSU precursors relative to the nucleolus of *Chlamydomonas*, tomograms where enough of the “nucleolar ring” was present were selected for the sphere fitting in which spheres were fit to the positions of the nucleolar SSU and LSU precursors using a custom Matlab (MathWorks) script. In brief, a

spherical equation was fit using the least square fit from an initial guess for center and radius, which were calculated as the mean of all positions and mean distance to this center, respectively. Outliers with  $\pm 1$  standard deviation by distance to the calculated center were then removed, and this procedure was repeated until no more changes were observed and the fit which the highest number of points retained was taken.

### 5.15 Density Measurements

To demonstrate that the SSU and LSU precursors are generated from the nucleolus and turn into structured particles from the surface of the nucleolus, the image-based density measurement was performed for *Chlamydomonas* preribosomes. Denoised tomograms were normalized to a mean of zero and a standard deviation of one. Through the measurement of the mass of densities at coordinates that was determined by the template matching, the threshold of binarization was determined by each tomogram. When the mean mass of all subtomograms approximated 4.5 MDa, the threshold was decreased and applied to the entire tomogram for binarization. Binarized volumes were segmented with Matlab's `regionprops3`, and XYZ coordinates and the number of voxels of each object were produced. Densities were colored in Chimera based on the size, and the corresponding mass of each subvolume was calculated according to the voxel size and the protein density ( $1.3 \text{ g/cm}^3$ ). Combining with the sphere fit, the distance to the center of the nucleolus was calculated for each coordinate. The radius of the determined spheres was used to normalize all measured distances. Subsequently, one-dimensional histogram and two-dimensional histogram were generated based on the mass and normalized distance.

### 5.16 Classification Reproducibility

To verify the reproducibility of sub-classification of SSU precursors, multireference alignment implemented in STOPGAP was applied, and the whole procedure was repeated three times. First, subtomograms from Relion were aligned in stopgap with original shifts and angles for two iterations without any improvement in FSC and map quality. After that, the alignment of subtomograms after two iterations was used as the

starting point of multireference alignment. The initial multireference classification was conducted with a global mask, and starting references were generated through a random assignment of subtomograms to 10 classes with an oversampling factor of two. Subsequently, the simulated annealing multireference alignment was carried out against the starting references for 10 iterations with decreasing temperature factors (10 to 0), followed by a continued alignment without the simulated annealing for 30 iterations or until the class convergence (<1% of subtomograms changing class during an iteration) was achieved. In the end, a stochastic hill-climbing search algorithm was applied to score class assignments, and by analyzing the resulting 30 structures, the most variable region was determined across all classes.

Following that, a mask focused on the most variable region was applied in another round of simulated annealing multireference classification that was repeated for six times. Class occupancies after the class convergence for each repeat were observed, and final averages were generated through a consensus subtomogram assignment for each of the three classes obtained in Relion. In addition, cross-effects including orientation, defocus, and lamella thickness were examined.

### **5.17 Data Visualization**

Membranes were automatically segmented using PySeg and generated by Amira (FEI). Using an in-house Matlab script, ribosome particles and preribosome particles were mapped back into the corresponding tomograms. LLPS area was generated by adjusting the thresholding based on the grey value in Amira (FEI). For structural comparison, EM maps were downloaded from the EMDB/PDB and re-scaled to the pixel size used in the project. The illustration of 3D models was then performed with Chimera (UCSF).

## 5.18 Software

Table 2: List of the used applied software.

<b>Name</b>	<b>Source</b>
<b>Amira</b>	Thermo Fisher Scientific
<b>CryoCare</b>	Buchholz et al., 2019
<b>Fiji</b>	Schindelin et al., 2012
<b>Getf</b>	Zhang, 2016
<b>Huygens</b>	Scientific volume imaging
<b>IMOD</b>	Kremer et al., 1996
<b>M</b>	Tegunov et al., 2020
<b>Matlab</b>	MathWorks
<b>MotionCor2</b>	Zheng et al., 2017
<b>Pyto</b>	Lučić et al., 2016
<b>Relion</b>	Zivanov et al., 2018
<b>SerialEM</b>	Mastronarde, 2005
<b>STOPGAP</b>	Wan, William, et al., 2020
<b>TOM software toolbox</b>	Nickell et al., 2005
<b>TomoSegMem TV</b>	Martinez-Sanchez et al., 2014
<b>UCSF Chimera</b>	Pettersen et al., 2004
<b>Warp</b>	Tegunov et al., 2019

## 6. Appendix

### 6.1 Abbreviations

Table 3. List of the abbreviations used in this dissertation.

<b>Abbreviation</b>	<b>Full name</b>
<b>AF</b>	Assembly factor
<b>ACT1</b>	Nuclear factor-kappa-B activator 1
<b>BCR</b>	B cell receptor
<b>BLNK</b>	B cell linker
<b>Cryo-EM</b>	Cryo-electron microscopy
<b>Cryo-ET</b>	Cryo-electron tomography
<b>Cryo-CLEM</b>	Cryo-correlative light and electron microscopy
<b>CTF</b>	Contrast transfer function
<b>DAZ</b>	Diazaborine
<b>DFC</b>	Dense fibrillar component
<b>dsRNA</b>	Double-stranded RNA
<b>eGFP</b>	Enhanced green fluorescent protein
<b>eRF</b>	Eukaryotic peptide chain release factor subunit
<b>eEF</b>	Yeast elongation factor
<b>EM</b>	Electron microscopy
<b>ETS</b>	External transcribed spacer
<b>FC</b>	Fibrillar center
<b>F</b>	Fibrillar stand
<b>FSC</b>	Fourier shell correlation
<b>FLM</b>	Fluorescence microscopy
<b>GFP</b>	Green fluorescent protein

<b>GEM</b>	Genetically encoded multimer
<b>GIS</b>	Gas injection system
<b>GC</b>	Granular component
<b>G</b>	Granule
<b>GTP</b>	Guanosine triphosphate
<b>HRDC</b>	Helicase and RNaseD C-terminal
<b>ITS</b>	Internal transcribed spacer
<b>Ig</b>	Immunoglobulin
<b>ITAMS</b>	Immunoreceptor tyrosine-based activation motifs
<b>LN<sub>2</sub></b>	Liquid nitrogen
<b>LSU</b>	Large subunit
<b>MHC</b>	Major histocompatibility complex
<b>NPC</b>	Nuclear pore complexes
<b>NE</b>	Nuclear envelope
<b>NMD</b>	Nonsense-mediated mRNA decay
<b>NSD</b>	Non-stop mRNA decay
<b>NGD</b>	No-go mRNA decay
<b>OD</b>	Optical density
<b>PoI</b>	Polymerase
<b>Pre-rRNA</b>	Preribosomal RNA
<b>PDF</b>	Probability density function
<b>PIN</b>	PilT N-terminus
<b>PGK1</b>	phosphoglycerate kinase 1
<b>PTK</b>	Protein tyrosine kinase
<b>RQC</b>	Ribosome-associated quality control

<b>RFP</b>	Red fluorescent protein
<b>SNR</b>	Signal-to-noise ratio
<b>SEM</b>	Scanning electron microscopy
<b>SSU</b>	Small subunit
<b>snoRNP</b>	Small nucleolar ribonucleoprotein
<b>Ski</b>	Superkiller protein
<b>TEM</b>	Transmission electron microscopy
<b>TRAMP</b>	TRf4/5-Air1/20-Mtr4 polyadenylation
<b>TPR</b>	Tetratricopeptide repeat
<b>VAMP</b>	Vesicle-associated membrane protein
<b>WD</b>	Tryptophan-aspartic acid
<b>WT</b>	Wild type
<b>yGFP</b>	Yeast green fluorescent protein

## 6.2 References

- Abudula, A., A. Grabbe, M. Brechmann, C. Polaschegg, N. Herrmann, I. Goldbeck, K. Dittmann and J. Wienands (2007). "SLP-65 signal transduction requires Src homology 2 domain-mediated membrane anchoring and a kinase-independent adaptor function of Syk." *J Biol Chem* **282**(39): 29059-29066.
- Allegretti, M., C. E. Zimmerli, V. Rantos, F. Wilfling, P. Ronchi, H. K. H. Fung, C. W. Lee, W. Hagen, B. Turoňová, K. Karius, M. Börmel, X. Zhang, C. W. Müller, Y. Schwab, J. Mahamid, B. Pfander, J. Kosinski and M. Beck (2020). "In-cell architecture of the nuclear pore and snapshots of its turnover." *Nature* **586**(7831): 796-800.
- Allmang, C., J. Kufel, G. Chanfreau, P. Mitchell, E. Petfalski and D. Tollervey (1999). "Functions of the exosome in rRNA, snoRNA and snRNA synthesis." *Embo j* **18**(19): 5399-5410.
- Amat, F., F. Moussavi, L. R. Comolli, G. Elidan, K. H. Downing and M. Horowitz (2008). "Markov random field based automatic image alignment for electron tomography." *J Struct Biol* **161**(3): 260-275.
- Andersen, C. B., T. Becker, M. Blau, M. Anand, M. Halic, B. Balar, T. Mielke, T. Boesen, J. S. Pedersen, C. M. Spahn, T. G. Kinzy, G. R. Andersen and R. Beckmann

- (2006). "Structure of eEF3 and the mechanism of transfer RNA release from the E-site." *Nature* **443**(7112): 663-668.
- Andersen, K. R., T. H. Jensen and D. E. Brodersen (2008). "Take the "A" tail--quality control of ribosomal and transfer RNA." *Biochim Biophys Acta* **1779**(9): 532-537.
- Anderson, J., L. Phan and A. G. Hinnebusch (2000). "The Gcd10p/Gcd14p complex is the essential two-subunit tRNA(1-methyladenosine) methyltransferase of *Saccharomyces cerevisiae*." *Proc Natl Acad Sci U S A* **97**(10): 5173-5178.
- Anderson, J. S. and R. P. Parker (1998). "The 3' to 5' degradation of yeast mRNAs is a general mechanism for mRNA turnover that requires the SKI2 DEVH box protein and 3' to 5' exonucleases of the exosome complex." *Embo j* **17**(5): 1497-1506.
- Araki, Y., S. Takahashi, T. Kobayashi, H. Kajihio, S. Hoshino and T. Katada (2001). "Ski7p G protein interacts with the exosome and the Ski complex for 3'-to-5' mRNA decay in yeast." *Embo j* **20**(17): 4684-4693.
- Arnold, J., J. Mahamid, V. Lucic, A. de Marco, J. J. Fernandez, T. Laugks, T. Mayer, A. A. Hyman, W. Baumeister and J. M. Plitzko (2016). "Site-Specific Cryo-focused Ion Beam Sample Preparation Guided by 3D Correlative Microscopy." *Biophys J* **110**(4): 860-869.
- Asano, S., B. D. Engel and W. Baumeister (2016). "In Situ Cryo-Electron Tomography: A Post-Reductionist Approach to Structural Biology." *J Mol Biol* **428**(2 Pt A): 332-343.
- Banani, S. F., H. O. Lee, A. A. Hyman and M. K. Rosen (2017). "Biomolecular condensates: organizers of cellular biochemistry." *Nat Rev Mol Cell Biol* **18**(5): 285-298.
- Baßler, J. and E. Hurt (2019). "Eukaryotic Ribosome Assembly." *Annu Rev Biochem* **88**: 281-306.
- Baßler, J., H. Paternoga, I. Holdermann, M. Thoms, S. Granneman, C. Barrio-Garcia, A. Nyarko, W. Lee, G. Stier, S. A. Clark, D. Schraivogel, M. Kallas, R. Beckmann, D. Tollervey, E. Barbar, I. Sinning and E. Hurt (2014). "A network of assembly factors is involved in remodeling rRNA elements during preribosome maturation." *J Cell Biol* **207**(4): 481-498.
- Baumeister, W. (2005). "From proteomic inventory to architecture." *FEBS Lett* **579**(4): 933-937.
- Benschop, R. J. and J. C. Cambier (1999). "B cell development: signal transduction by antigen receptors and their surrogates." *Curr Opin Immunol* **11**(2): 143-151.
- Bohnenberger, H., T. Oellerich, M. Engelke, H. H. Hsiao, H. Urlaub and J. Wienands (2011). "Complex phosphorylation dynamics control the composition of the Syk interactome in B cells." *Eur J Immunol* **41**(6): 1550-1562.
- Bonneau, F., J. Basquin, J. Ebert, E. Lorentzen and E. Conti (2009). "The yeast exosome functions as a macromolecular cage to channel RNA substrates for degradation." *Cell* **139**(3): 547-559.
- Briggs, M. W., K. T. Burkard and J. S. Butler (1998). "Rrp6p, the yeast homologue of the human PM-Scl 100-kDa autoantigen, is essential for efficient 5.8 S rRNA 3' end formation." *J Biol Chem* **273**(21): 13255-13263.

- Brilot, A. F., J. Z. Chen, A. Cheng, J. Pan, S. C. Harrison, C. S. Potter, B. Carragher, R. Henderson and N. Grigorieff (2012). "Beam-induced motion of vitrified specimen on holey carbon film." J Struct Biol **177**(3): 630-637.
- Brown, J. T., X. Bai and A. W. Johnson (2000). "The yeast antiviral proteins Ski2p, Ski3p, and Ski8p exist as a complex in vivo." Rna **6**(3): 449-457.
- Buchholz, T.-O., M. Jordan, G. Pigino and F. Jug (2019). Cryo-care: content-aware image restoration for cryo-transmission electron microscopy data. 2019 IEEE 16th International Symposium on Biomedical Imaging (ISBI 2019), IEEE.
- Burger, J. A. and A. Wiestner (2018). "Targeting B cell receptor signalling in cancer: preclinical and clinical advances." Nat Rev Cancer **18**(3): 148-167.
- Butler, J. S. and P. Mitchell (2010). "Rrp6, Rrp47 and cofactors of the nuclear exosome." Adv Exp Med Biol **702**: 91-104.
- Casola, S., K. L. Otipoby, M. Alimzhanov, S. Humme, N. Uyttersprot, J. L. Kutok, M. C. Carroll and K. Rajewsky (2004). "B cell receptor signal strength determines B cell fate." Nat Immunol **5**(3): 317-327.
- Chang, Y. W., S. Chen, E. I. Tocheva, A. Treuner-Lange, S. Löbach, L. Søgaard-Andersen and G. J. Jensen (2014). "Correlated cryogenic photoactivated localization microscopy and cryo-electron tomography." Nat Methods **11**(7): 737-739.
- Chekanova, J. A., B. D. Gregory, S. V. Reverdatto, H. Chen, R. Kumar, T. Hooker, J. Yazaki, P. Li, N. Skiba, Q. Peng, J. Alonso, V. Brukhin, U. Grossniklaus, J. R. Ecker and D. A. Belostotsky (2007). "Genome-wide high-resolution mapping of exosome substrates reveals hidden features in the Arabidopsis transcriptome." Cell **131**(7): 1340-1353.
- Chen, D. and S. Huang (2001). "Nucleolar components involved in ribosome biogenesis cycle between the nucleolus and nucleoplasm in interphase cells." J Cell Biol **153**(1): 169-176.
- Chen, Y. (2015). 3D Image Processing for Structural Analysis of Macromolecules Using Cryo-Electron Tomography, Technische Universität München.
- Chen, Y. and F. Förster (2014). "Iterative reconstruction of cryo-electron tomograms using nonuniform fast Fourier transforms." J Struct Biol **185**(3): 309-316.
- Chen, Y., T. Hrabe, S. Pfeffer, O. Pauly, D. Mateus, N. Navab and F. Förster (2012). Detection and identification of macromolecular complexes in cryo-electron tomograms using support vector machines. 2012 9th IEEE International Symposium on Biomedical Imaging (ISBI), IEEE.
- Cheng, Y. (2015). "Single-Particle Cryo-EM at Crystallographic Resolution." Cell **161**(3): 450-457.
- Cheng, Z., K. Saito, A. V. Pisarev, M. Wada, V. P. Pisareva, T. V. Pestova, M. Gajda, A. Round, C. Kong, M. Lim, Y. Nakamura, D. I. Svergun, K. Ito and H. Song (2009). "Structural insights into eRF3 and stop codon recognition by eRF1." Genes Dev **23**(9): 1106-1118.
- Chiu, W. (1986). "Electron microscopy of frozen, hydrated biological specimens." Annu Rev Biophys Biophys Chem **15**: 237-257.

- Conti, E. and E. Izaurralde (2005). "Nonsense-mediated mRNA decay: molecular insights and mechanistic variations across species." Curr Opin Cell Biol **17**(3): 316-325.
- Cooper, M. D. (2015). "The early history of B cells." Nat Rev Immunol **15**(3): 191-197.
- D'Andrea, L. D. and L. Regan (2003). "TPR proteins: the versatile helix." Trends Biochem Sci **28**(12): 655-662.
- Das, B., Z. Guo, P. Russo, P. Chartrand and F. Sherman (2000). "The role of nuclear cap binding protein Cbc1p of yeast in mRNA termination and degradation." Mol Cell Biol **20**(8): 2827-2838.
- Davison, M. E. (1983). "The Ill-Conditioned Nature of the Limited Angle Tomography Problem." Siam Journal on Applied Mathematics **43**(2): 428-448.
- de la Cruz, J., K. Karbstein and J. L. Woolford, Jr. (2015). "Functions of ribosomal proteins in assembly of eukaryotic ribosomes in vivo." Annu Rev Biochem **84**: 93-129.
- DeFranco, A. L. (1997). "The complexity of signaling pathways activated by the BCR." Curr Opin Immunol **9**(3): 296-308.
- Delarue, M., G. P. Brittingham, S. Pfeffer, I. V. Surovtsev, S. Pinglay, K. J. Kennedy, M. Schaffer, J. I. Gutierrez, D. Sang, G. Poterewicz, J. K. Chung, J. M. Plitzko, J. T. Groves, C. Jacobs-Wagner, B. D. Engel and L. J. Holt (2018). "mTORC1 Controls Phase Separation and the Biophysical Properties of the Cytoplasm by Tuning Crowding." Cell **174**(2): 338-349.e320.
- Derenzini, M., F. Farabegoli and D. Trerè (1993). "Localization of DNA in the fibrillar components of the nucleolus: a cytochemical and morphometric study." J Histochem Cytochem **41**(6): 829-836.
- Doma, M. K. and R. Parker (2006). "Endonucleolytic cleavage of eukaryotic mRNAs with stalls in translation elongation." Nature **440**(7083): 561-564.
- Drazkowska, K., R. Tomecki, K. Stodus, K. Kowalska, M. Czarnocki-Cieciura and A. Dziembowski (2013). "The RNA exosome complex central channel controls both exonuclease and endonuclease Dis3 activities in vivo and in vitro." Nucleic Acids Res **41**(6): 3845-3858.
- Dubochet, J., M. Adrian, J. J. Chang, J. C. Homo, J. Lepault, A. W. McDowell and P. Schultz (1988). "Cryo-electron microscopy of vitrified specimens." Q Rev Biophys **21**(2): 129-228.
- Dziembowski, A., E. Lorentzen, E. Conti and B. Séraphin (2007). "A single subunit, Dis3, is essentially responsible for yeast exosome core activity." Nat Struct Mol Biol **14**(1): 15-22.
- Engel, B. D., M. Schaffer, L. Kuhn Cuellar, E. Villa, J. M. Plitzko and W. Baumeister (2015). "Native architecture of the Chlamydomonas chloroplast revealed by in situ cryo-electron tomography." Elife **4**.
- Engelke, M., S. Pirkuliyeva, J. Kühn, L. Wong, J. Boyken, N. Herrmann, S. Becker, C. Griesinger and J. Wienands (2014). "Macromolecular assembly of the adaptor SLP-65 at intracellular vesicles in resting B cells." Sci Signal **7**(339): ra79.

- Erdmann, P. S., Z. Hou, S. Klumpe, S. Khavnekar, F. Beck, F. Wilfling, J. M. Plitzko and W. Baumeister (2021). "In situ cryo-electron tomography reveals gradient organization of ribosome biogenesis in intact nucleoli." Nat Commun **12**(1): 5364.
- Erdmann, P. S., J. M. Plitzko and W. Baumeister (2018). "Addressing cellular compartmentalization by in situ cryo-electron tomography." Current Opinion in Colloid & Interface Science **34**: 89-99.
- Faruqi, A. R. and R. Henderson (2007). "Electronic detectors for electron microscopy." Curr Opin Struct Biol **17**(5): 549-555.
- Feng, Z., B. Jia and M. Zhang (2021). "Liquid-Liquid Phase Separation in Biology: Specific Stoichiometric Molecular Interactions vs Promiscuous Interactions Mediated by Disordered Sequences." Biochemistry **60**(31): 2397-2406.
- Feric, M., N. Vaidya, T. S. Harmon, D. M. Mitrea, L. Zhu, T. M. Richardson, R. W. Kriwacki, R. V. Pappu and C. P. Brangwynne (2016). "Coexisting Liquid Phases Underlie Nucleolar Subcompartments." Cell **165**(7): 1686-1697.
- Fernández-Pevida, A., D. Kressler and J. de la Cruz (2015). "Processing of preribosomal RNA in *Saccharomyces cerevisiae*." Wiley Interdiscip Rev RNA **6**(2): 191-209.
- Förster, F., B.-G. Han and M. Beck (2010). "Visual proteomics." Methods in enzymology **483**: 215-243.
- Förster, F., S. Pruggnaller, A. Seybert and A. S. Frangakis (2008). "Classification of cryo-electron sub-tomograms using constrained correlation." Journal of structural biology **161**(3): 276-286.
- Frangakis, A. S., J. Böhm, F. Förster, S. Nickell, D. Nicastro, D. Typke, R. Hegerl and W. Baumeister (2002). "Identification of macromolecular complexes in cryoelectron tomograms of phantom cells." Proceedings of the National Academy of Sciences **99**(22): 14153-14158.
- Frank, J. (2002). "Single-particle imaging of macromolecules by cryo-electron microscopy." Annual review of biophysics and biomolecular structure **31**(1): 303-319.
- Frank, J. (2006). Three-dimensional electron microscopy of macromolecular assemblies: visualization of biological molecules in their native state, Oxford university press.
- Frischmeyer, P. A., A. van Hoof, K. O'Donnell, A. L. Guerrierio, R. Parker and H. C. Dietz (2002). "An mRNA surveillance mechanism that eliminates transcripts lacking termination codons." Science **295**(5563): 2258-2261.
- Frolova, L., X. Le Goff, G. Zhouravleva, E. Davydova, M. Philippe and L. Kisselev (1996). "Eukaryotic polypeptide chain release factor eRF3 is an eRF1- and ribosome-dependent guanosine triphosphatase." Rna **2**(4): 334-341.
- Fu, C., C. W. Turck, T. Kurosaki and A. C. Chan (1998). "BLNK: a central linker protein in B cell activation." Immunity **9**(1): 93-103.
- Fuchs, J. and J. Loidl (2004). "Behaviour of nucleolus organizing regions (NORs) and nucleoli during mitotic and meiotic divisions in budding yeast." Chromosome Res **12**(5): 427-438.
- Gierasch, L. M. and A. Gershenson (2009). "Post-reductionist protein science, or putting Humpty Dumpty back together again." Nat Chem Biol **5**(11): 774-777.

- Gillen, K. M., M. Pausch and H. G. Dohlman (1998). "N-terminal domain of Gpa1 (G protein alpha) subunit) is sufficient for plasma membrane targeting in yeast *Saccharomyces cerevisiae*." J Cell Sci **111** ( Pt 21): 3235-3244.
- Girke, P. and W. Seufert (2019). "Compositional reorganization of the nucleolus in budding yeast mitosis." Mol Biol Cell **30**(5): 591-606.
- Gudipati, R. K., Z. Xu, A. Lebreton, B. Séraphin, L. M. Steinmetz, A. Jacquier and D. Libri (2012). "Extensive degradation of RNA precursors by the exosome in wild-type cells." Mol Cell **48**(3): 409-421.
- Gupta, S. and R. Santoro (2020). "Regulation and Roles of the Nucleolus in Embryonic Stem Cells: From Ribosome Biogenesis to Genome Organization." Stem Cell Reports **15**(6): 1206-1219.
- Hagen, W. J. H., W. Wan and J. A. G. Briggs (2017). "Implementation of a cryo-electron tomography tilt-scheme optimized for high resolution subtomogram averaging." J Struct Biol **197**(2): 191-198.
- Halbach, F., P. Reichelt, M. Rode and E. Conti (2013). "The yeast ski complex: crystal structure and RNA channeling to the exosome complex." Cell **154**(4): 814-826.
- Halbach, F., M. Rode and E. Conti (2012). "The crystal structure of *S. cerevisiae* Ski2, a DEXH helicase associated with the cytoplasmic functions of the exosome." Rna **18**(1): 124-134.
- Harapin, J., M. Börmel, K. T. Sapra, D. Brunner, A. Kaech and O. Medalia (2015). "Structural analysis of multicellular organisms with cryo-electron tomography." Nat Methods **12**(7): 634-636.
- Henderson, R. and R. M. Glaeser (1985). "Quantitative-Analysis of Image-Contrast in Electron-Micrographs of Beam-Sensitive Crystals." Ultramicroscopy **16**(2): 139-150.
- Hernandez-Verdun, D. (2011). "Assembly and disassembly of the nucleolus during the cell cycle." Nucleus **2**(3): 189-194.
- Hernandez-Verdun, D., P. Roussel, M. Thiry, V. Sirri and D. L. Lafontaine (2010). "The nucleolus: structure/function relationship in RNA metabolism." Wiley Interdiscip Rev RNA **1**(3): 415-431.
- Herrick, D. (1989). "Structural determinants of mRNA turnover in yeast: a thesis."
- Ho, B., A. Baryshnikova and G. W. Brown (2018). "Unification of Protein Abundance Datasets Yields a Quantitative *Saccharomyces cerevisiae* Proteome." Cell Syst **6**(2): 192-205.e193.
- Houseley, J. and D. Tollervey (2009). "The many pathways of RNA degradation." Cell **136**(4): 763-776.
- Hrabe, T., Y. Chen, S. Pfeffer, L. K. Cuellar, A.-V. Mangold and F. Förster (2012). "PyTom: a python-based toolbox for localization of macromolecules in cryo-electron tomograms and subtomogram analysis." Journal of structural biology **178**(2): 177-188.
- Hubstenberger, A., S. L. Noble, C. Cameron and T. C. Evans (2013). "Translation repressors, an RNA helicase, and developmental cues control RNP phase transitions during early development." Dev Cell **27**(2): 161-173.

- Hunziker, M., J. Barandun, E. Petfalski, D. Tan, C. Delan-Forino, K. R. Molloy, K. H. Kim, H. Dunn-Davies, Y. Shi, M. Chaker-Margot, B. T. Chait, T. Walz, D. Tollervey and S. Klinge (2016). "UtpA and UtpB chaperone nascent pre-ribosomal RNA and U3 snoRNA to initiate eukaryotic ribosome assembly." Nat Commun **7**: 12090.
- Hyman, A. A., C. A. Weber and F. Julicher (2014). "Liquid-liquid phase separation in biology." Annu Rev Cell Dev Biol **30**: 39-58.
- Iancu, C. V., W. F. Tivol, J. B. Schooler, D. P. Dias, G. P. Henderson, G. E. Murphy, E. R. Wright, Z. Li, Z. Yu, A. Briegel, L. Gan, Y. He and G. J. Jensen (2006). "Electron cryotomography sample preparation using the Vitrobot." Nat Protoc **1**(6): 2813-2819.
- Ikeuchi, K., P. Tesina, Y. Matsuo, T. Sugiyama, J. Cheng, Y. Saeki, K. Tanaka, T. Becker, R. Beckmann and T. Inada (2019). "Collided ribosomes form a unique structural interface to induce Hel2-driven quality control pathways." Embo j **38**(5).
- Ikonomova, R., T. Sommer and F. Képès (1997). "The Srp40 protein plays a dose-sensitive role in preribosome assembly or transport and depends on its carboxy-terminal domain for proper localization to the yeast nucleoskeleton." DNA Cell Biol **16**(10): 1161-1173.
- Ishiai, M., M. Kurosaki, R. Pappu, K. Okawa, I. Ronko, C. Fu, M. Shibata, A. Iwamatsu, A. C. Chan and T. Kurosaki (1999). "BLNK required for coupling Syk to PLC gamma 2 and Rac1-JNK in B cells." Immunity **10**(1): 117-125.
- Jenner, L., S. Melnikov, N. Garreau de Loubresse, A. Ben-Shem, M. Iskakova, A. Urzhumtsev, A. Meskauskas, J. Dinman, G. Yusupova and M. Yusupov (2012). "Crystal structure of the 80S yeast ribosome." Curr Opin Struct Biol **22**(6): 759-767.
- Johnson, A. W. and R. D. Kolodner (1995). "Synthetic lethality of sep1 (xrn1) ski2 and sep1 (xrn1) ski3 mutants of *Saccharomyces cerevisiae* is independent of killer virus and suggests a general role for these genes in translation control." Mol Cell Biol **15**(5): 2719-2727.
- Jumaa, H., B. Wollscheid, M. Mitterer, J. Wienands, M. Reth and P. J. Nielsen (1999). "Abnormal development and function of B lymphocytes in mice deficient for the signaling adaptor protein SLP-65." Immunity **11**(5): 547-554.
- Jurewicz, M. M. and L. J. Stern (2019). "Class II MHC antigen processing in immune tolerance and inflammation." Immunogenetics **71**(3): 171-187.
- Juszkiewicz, S., V. Chandrasekaran, Z. Lin, S. Kraatz, V. Ramakrishnan and R. S. Hegde (2018). "ZNF598 Is a Quality Control Sensor of Collided Ribosomes." Mol Cell **72**(3): 469-481.e467.
- Kadaba, S., A. Krueger, T. Trice, A. M. Krecic, A. G. Hinnebusch and J. Anderson (2004). "Nuclear surveillance and degradation of hypomodified initiator tRNAMet in *S. cerevisiae*." Genes Dev **18**(11): 1227-1240.
- Karbstein, K. (2013). "Quality control mechanisms during ribosome maturation." Trends Cell Biol **23**(5): 242-250.
- Kater, L., M. Thoms, C. Barrio-Garcia, J. Cheng, S. Ismail, Y. L. Ahmed, G. Bange, D. Kressler, O. Berninghausen, I. Sinning, E. Hurt and R. Beckmann (2017). "Visualizing the Assembly Pathway of Nucleolar Pre-60S Ribosomes." Cell **171**(7): 1599-1610.e1514.

- Klinge, S., F. Voigts-Hoffmann, M. Leibundgut and N. Ban (2012). "Atomic structures of the eukaryotic ribosome." Trends Biochem Sci **37**(5): 189-198.
- Köhler, F., B. Storch, Y. Kulathu, S. Herzog, S. Kuppig, M. Reth and H. Jumaa (2005). "A leucine zipper in the N terminus confers membrane association to SLP-65." Nat Immunol **6**(2): 204-210.
- Konikkat, S. and J. L. Woolford, Jr. (2017). "Principles of 60S ribosomal subunit assembly emerging from recent studies in yeast." Biochem J **474**(2): 195-214.
- Koning, R. I., A. J. Koster and T. H. Sharp (2018). "Advances in cryo-electron tomography for biology and medicine." Ann Anat **217**: 82-96.
- Kornprobst, M., M. Turk, N. Kellner, J. Cheng, D. Flemming, I. Koš-Braun, M. Koš, M. Thoms, O. Berninghausen, R. Beckmann and E. Hurt (2016). "Architecture of the 90S Pre-ribosome: A Structural View on the Birth of the Eukaryotic Ribosome." Cell **166**(2): 380-393.
- Kowalinski, E., A. Kögel, J. Ebert, P. Reichelt, E. Stegmann, B. Habermann and E. Conti (2016). "Structure of a Cytoplasmic 11-Subunit RNA Exosome Complex." Mol Cell **63**(1): 125-134.
- Kressler, D., E. Hurt and J. Bassler (2010). "Driving ribosome assembly." Biochim Biophys Acta **1803**(6): 673-683.
- Kressler, D., P. Linder and J. de La Cruz (1999). "Protein trans-acting factors involved in ribosome biogenesis in *Saccharomyces cerevisiae*." Mol Cell Biol **19**(12): 7897-7912.
- Krivanek, O. L., S. L. Friedman, A. J. Gubbens and B. Kraus (1995). "An imaging filter for biological applications." Ultramicroscopy **59**(1-4): 267-282.
- Kühn, J., L. E. Wong, S. Pirkuliyeva, K. Schulz, C. Schwiegk, K. G. Fünfgeld, S. Keppler, F. D. Batista, H. Urlaub, M. Habeck, S. Becker, C. Griesinger and J. Wienands (2016). "The adaptor protein CIN85 assembles intracellular signaling clusters for B cell activation." Sci Signal **9**(434): ra66.
- Kunz, M. and A. S. Frangakis (2014). "Super-sampling SART with ordered subsets." J Struct Biol **188**(2): 107-115.
- Kunz, M. and A. S. Frangakis (2017). "Three-dimensional CTF correction improves the resolution of electron tomograms." J Struct Biol **197**(2): 114-122.
- Kurosaki, T. and S. Tsukada (2000). "BLNK: connecting Syk and Btk to calcium signals." Immunity **12**(1): 1-5.
- Kwak, K., M. Akkaya and S. K. Pierce (2019). "B cell signaling in context." Nat Immunol **20**(8): 963-969.
- LaCava, J., J. Houseley, C. Saveanu, E. Petfalski, E. Thompson, A. Jacquier and D. Tollervey (2005). "RNA degradation by the exosome is promoted by a nuclear polyadenylation complex." Cell **121**(5): 713-724.
- Lam, Y. W. and L. Trinkle-Mulcahy (2015). "New insights into nucleolar structure and function." F1000Prime Rep **7**: 48.
- Lamond, A. I. and J. E. Sleeman (2003). "Nuclear substructure and dynamics." Curr Biol **13**(21): R825-828.

- Léger-Silvestre, I., S. Trumtel, J. Noaillac-Depeyre and N. Gas (1999). "Functional compartmentalization of the nucleus in the budding yeast *Saccharomyces cerevisiae*." Chromosoma **108**(2): 103-113.
- Li, P., S. Banjade, H. C. Cheng, S. Kim, B. Chen, L. Guo, M. Llaguno, J. V. Hollingsworth, D. S. King, S. F. Banani, P. S. Russo, Q. X. Jiang, B. T. Nixon and M. K. Rosen (2012). "Phase transitions in the assembly of multivalent signalling proteins." Nature **483**(7389): 336-340.
- Li, X., P. Mooney, S. Zheng, C. R. Booth, M. B. Braunfeld, S. Gubbens, D. A. Agard and Y. Cheng (2013). "Electron counting and beam-induced motion correction enable near-atomic-resolution single-particle cryo-EM." Nat Methods **10**(6): 584-590.
- Liu, B., Y. Xue, W. Zhao, Y. Chen, C. Fan, L. Gu, Y. Zhang, X. Zhang, L. Sun, X. Huang, W. Ding, F. Sun, W. Ji and T. Xu (2015). "Three-dimensional super-resolution protein localization correlated with vitrified cellular context." Sci Rep **5**: 13017.
- Liu, J. J., M. A. Bratkowski, X. Liu, C. Y. Niu, A. Ke and H. W. Wang (2014). "Visualization of distinct substrate-recruitment pathways in the yeast exosome by EM." Nat Struct Mol Biol **21**(1): 95-102.
- Liu, J. J., C. Y. Niu, Y. Wu, D. Tan, Y. Wang, M. D. Ye, Y. Liu, W. Zhao, K. Zhou, Q. S. Liu, J. Dai, X. Yang, M. Q. Dong, N. Huang and H. W. Wang (2016). "CryoEM structure of yeast cytoplasmic exosome complex." Cell Res **26**(7): 822-837.
- Liu, Q., J. C. Greimann and C. D. Lima (2006). "Reconstitution, activities, and structure of the eukaryotic RNA exosome." Cell **127**(6): 1223-1237.
- Loder, F., B. Mutschler, R. J. Ray, C. J. Paige, P. Sideras, R. Torres, M. C. Lamers and R. Carsetti (1999). "B cell development in the spleen takes place in discrete steps and is determined by the quality of B cell receptor-derived signals." J Exp Med **190**(1): 75-89.
- Lorentzen, E., A. Dziembowski, D. Lindner, B. Seraphin and E. Conti (2007). "RNA channelling by the archaeal exosome." EMBO Rep **8**(5): 470-476.
- Lubas, M., M. S. Christensen, M. S. Kristiansen, M. Domanski, L. G. Falkenby, S. Lykke-Andersen, J. S. Andersen, A. Dziembowski and T. H. Jensen (2011). "Interaction profiling identifies the human nuclear exosome targeting complex." Mol Cell **43**(4): 624-637.
- Lucić, V., F. Förster and W. Baumeister (2005). "Structural studies by electron tomography: from cells to molecules." Annu Rev Biochem **74**: 833-865.
- Lučić, V., A. Rigort and W. Baumeister (2013). "Cryo-electron tomography: the challenge of doing structural biology in situ." J Cell Biol **202**(3): 407-419.
- Ma, C., S. Wu, N. Li, Y. Chen, K. Yan, Z. Li, L. Zheng, J. Lei, J. L. Woolford, Jr. and N. Gao (2017). "Structural snapshot of cytoplasmic pre-60S ribosomal particles bound by Nmd3, Lsg1, Tif6 and Reh1." Nat Struct Mol Biol **24**(3): 214-220.
- Makino, D. L., B. Schuch, E. Stegmann, M. Baumgärtner, C. Basquin and E. Conti (2015). "RNA degradation paths in a 12-subunit nuclear exosome complex." Nature **524**(7563): 54-58.

- Malyutin, A. G., S. Musalgaonkar, S. Patchett, J. Frank and A. W. Johnson (2017). "Nmd3 is a structural mimic of eIF5A, and activates the cpGTPase Lsg1 during 60S ribosome biogenesis." *Embo j* **36**(7): 854-868.
- Maniatis, T. and R. Reed (2002). "An extensive network of coupling among gene expression machines." *Nature* **416**(6880): 499-506.
- Marabini, R., G. T. Herman and J. M. Carazo (1998). "3D reconstruction in electron microscopy using ART with smooth spherically symmetric volume elements (blobs)." *Ultramicroscopy* **72**(1-2): 53-65.
- Marko, M., C. Hsieh, R. Schalek, J. Frank and C. Mannella (2007). "Focused-ion-beam thinning of frozen-hydrated biological specimens for cryo-electron microscopy." *Nat Methods* **4**(3): 215-217.
- Martinez-Sanchez, A., Z. Kochovski, U. Laugks, J. Meyer Zum Alten Borgloh, S. Chakraborty, S. Pfeffer, W. Baumeister and V. Lučić (2020). "Template-free detection and classification of membrane-bound complexes in cryo-electron tomograms." *Nat Methods* **17**(2): 209-216.
- Mastronarde, D. N. and S. R. Held (2017). "Automated tilt series alignment and tomographic reconstruction in IMOD." *J Struct Biol* **197**(2): 102-113.
- Matos-Perdomo, E. and F. Machín (2019). "Nucleolar and Ribosomal DNA Structure under Stress: Yeast Lessons for Aging and Cancer." *Cells* **8**(8).
- Matsuo, Y., S. Granneman, M. Thoms, R. G. Manikas, D. Tollervey and E. Hurt (2014). "Coupled GTPase and remodelling ATPase activities form a checkpoint for ribosome export." *Nature* **505**(7481): 112-116.
- Matsuo, Y., K. Ikeuchi, Y. Saeki, S. Iwasaki, C. Schmidt, T. Udagawa, F. Sato, H. Tsuchiya, T. Becker, K. Tanaka, N. T. Ingolia, R. Beckmann and T. Inada (2017). "Ubiquitination of stalled ribosome triggers ribosome-associated quality control." *Nat Commun* **8**(1): 159.
- Mayr, S., S. Finizio, J. Reuteler, S. Stutz, C. Dubs, M. Weigand, A. Hrabec, J. Raabe and S. Wintz (2021). "Xenon Plasma Focused Ion Beam Milling for Obtaining Soft X-ray Transparent Samples." *Crystals* **11**(5).
- McEwen, B. F., K. H. Downing and R. M. Glaeser (1995). "The relevance of dose-fractionation in tomography of radiation-sensitive specimens." *Ultramicroscopy* **60**(3): 357-373.
- Meaux, S. and A. Van Hoof (2006). "Yeast transcripts cleaved by an internal ribozyme provide new insight into the role of the cap and poly(A) tail in translation and mRNA decay." *Rna* **12**(7): 1323-1337.
- Melnikov, S., A. Ben-Shem, N. Garreau de Loubresse, L. Jenner, G. Yusupova and M. Yusupov (2012). "One core, two shells: bacterial and eukaryotic ribosomes." *Nat Struct Mol Biol* **19**(6): 560-567.
- Miller, O. L., Jr. and B. R. Beatty (1969). "Visualization of nucleolar genes." *Science* **164**(3882): 955-957.
- Mitchell, P., E. Petfalski, A. Shevchenko, M. Mann and D. Tollervey (1997). "The exosome: a conserved eukaryotic RNA processing complex containing multiple 3'->5' exoribonucleases." *Cell* **91**(4): 457-466.

- Montanaro, L., D. Treré and M. Derenzini (2008). "Nucleolus, ribosomes, and cancer." *Am J Pathol* **173**(2): 301-310.
- Mukherjee, K., J. Gardin, B. Futcher and J. Leatherwood (2016). "Relative contributions of the structural and catalytic roles of Rrp6 in exosomal degradation of individual mRNAs." *Rna* **22**(9): 1311-1319.
- Nakhoul, H., J. Ke, X. Zhou, W. Liao, S. X. Zeng and H. Lu (2014). "Ribosomopathies: mechanisms of disease." *Clin Med Insights Blood Disord* **7**: 7-16.
- Natterer, F. (2001). *The mathematics of computerized tomography*, SIAM.
- Nicastro, D., C. Schwartz, J. Pierson, R. Gaudette, M. E. Porter and J. R. McIntosh (2006). "The molecular architecture of axonemes revealed by cryoelectron tomography." *Science* **313**(5789): 944-948.
- Noble, A. J. and S. M. Stagg (2015). "Automated batch fiducial-less tilt-series alignment in Appion using Protomo." *J Struct Biol* **192**(2): 270-278.
- Ochs, R. L. (1998). "Methods used to study structure and function of the nucleolus." *Methods Cell Biol* **53**: 303-321.
- Oellerich, T., V. Bremes, K. Neumann, H. Bohnenberger, K. Dittmann, H. H. Hsiao, M. Engelke, T. Schnyder, F. D. Batista, H. Urlaub and J. Wienands (2011). "The B-cell antigen receptor signals through a preformed transducer module of SLP65 and CIN85." *Embo j* **30**(17): 3620-3634.
- Pal Singh, S., F. Dammeijer and R. W. Hendriks (2018). "Role of Bruton's tyrosine kinase in B cells and malignancies." *Mol Cancer* **17**(1): 57.
- Penczek, P., M. Marko, K. Buttle and J. Frank (1995). "Double-tilt electron tomography." *Ultramicroscopy* **60**(3): 393-410.
- Pérez-Fernández, J., A. Román, J. De Las Rivas, X. R. Bustelo and M. Dosil (2007). "The 90S preribosome is a multimodular structure that is assembled through a hierarchical mechanism." *Mol Cell Biol* **27**(15): 5414-5429.
- Phipps, K. R., J. Charette and S. J. Baserga (2011). "The small subunit processome in ribosome biogenesis—progress and prospects." *Wiley Interdiscip Rev RNA* **2**(1): 1-21.
- Prats, C., T. E. Graham and J. Shearer (2018). "The dynamic life of the glycogen granule." *J Biol Chem* **293**(19): 7089-7098.
- Qiu, H., J. Eifert, L. Wacheul, M. Thiry, A. C. Berger, J. Jakovljevic, J. L. Woolford, Jr., A. H. Corbett, D. L. Lafontaine, R. M. Terns and M. P. Terns (2008). "Identification of genes that function in the biogenesis and localization of small nucleolar RNAs in *Saccharomyces cerevisiae*." *Mol Cell Biol* **28**(11): 3686-3699.
- Radermacher, M. (2007). *Weighted back-projection methods. Electron tomography*, Springer: 245-273.
- Ramachandran, G. N. and A. V. Lakshminarayanan (1971). "Three-dimensional reconstruction from radiographs and electron micrographs: application of convolutions instead of Fourier transforms." *Proc Natl Acad Sci U S A* **68**(9): 2236-2240.
- Ranjan, N., A. A. Pochopien, C. Chih-Chien Wu, B. Beckert, S. Blanchet, R. Green, V. R. M and D. N. Wilson (2021). "Yeast translation elongation factor eEF3 promotes late stages of tRNA translocation." *Embo j* **40**(6): e106449.

- Reth, M. (1989). "Antigen receptor tail clue." *Nature* **338**(6214): 383-384.
- Reth, M. and J. Wienands (1997). "Initiation and processing of signals from the B cell antigen receptor." *Annu Rev Immunol* **15**: 453-479.
- Ridley, S. P., S. S. Sommer and R. B. Wickner (1984). "Superkiller mutations in *Saccharomyces cerevisiae* suppress exclusion of M2 double-stranded RNA by L-A-HN and confer cold sensitivity in the presence of M and L-A-HN." *Mol Cell Biol* **4**(4): 761-770.
- Rigort, A., F. J. Bäuerlein, E. Villa, M. Eibauer, T. Laugks, W. Baumeister and J. M. Plitzko (2012). "Focused ion beam micromachining of eukaryotic cells for cryoelectron tomography." *Proc Natl Acad Sci U S A* **109**(12): 4449-4454.
- Rigort, A., E. Villa, F. J. Bäuerlein, B. D. Engel and J. M. Plitzko (2012). "Integrative approaches for cellular cryo-electron tomography: correlative imaging and focused ion beam micromachining." *Methods Cell Biol* **111**: 259-281.
- Robinson, C. V., A. Sali and W. Baumeister (2007). "The molecular sociology of the cell." *Nature* **450**(7172): 973-982.
- Roussel, P., C. André, L. Comai and D. Hernandez-Verdun (1996). "The rDNA transcription machinery is assembled during mitosis in active NORs and absent in inactive NORs." *J Cell Biol* **133**(2): 235-246.
- Rudd, C. E. (1999). "Adaptors and molecular scaffolds in immune cell signaling." *Cell* **96**(1): 5-8.
- Saito, S., N. Hosoda and S. Hoshino (2013). "The Hbs1-Dom34 protein complex functions in non-stop mRNA decay in mammalian cells." *J Biol Chem* **288**(24): 17832-17843.
- Salas-Marco, J. and D. M. Bedwell (2004). "GTP hydrolysis by eRF3 facilitates stop codon decoding during eukaryotic translation termination." *Mol Cell Biol* **24**(17): 7769-7778.
- Saxton, W. O. and W. Baumeister (1982). "The correlation averaging of a regularly arranged bacterial cell envelope protein." *J Microsc* **127**(Pt 2): 127-138.
- Schäfer, T., D. Strauss, E. Petfalski, D. Tollervy and E. Hurt (2003). "The path from nucleolar 90S to cytoplasmic 40S pre-ribosomes." *Embo j* **22**(6): 1370-1380.
- Schaffer, M., B. D. Engel, T. Laugks, J. Mahamid, J. M. Plitzko and W. Baumeister (2015). "Cryo-focused Ion Beam Sample Preparation for Imaging Vitreous Cells by Cryo-electron Tomography." *Bio Protoc* **5**(17).
- Schaffer, M., J. Mahamid, B. D. Engel, T. Laugks, W. Baumeister and J. M. Plitzko (2017). "Optimized cryo-focused ion beam sample preparation aimed at in situ structural studies of membrane proteins." *J Struct Biol* **197**(2): 73-82.
- Schaffer, M., S. Pfeffer, J. Mahamid, S. Kleindiek, T. Laugks, S. Albert, B. D. Engel, A. Rummel, A. J. Smith, W. Baumeister and J. M. Plitzko (2019). "A cryo-FIB lift-out technique enables molecular-resolution cryo-ET within native *Caenorhabditis elegans* tissue." *Nat Methods* **16**(8): 757-762.
- Schamel, W. W. and M. Reth (2000). "Monomeric and oligomeric complexes of the B cell antigen receptor." *Immunity* **13**(1): 5-14.

- Scheres, S. H., R. Melero, M. Valle and J.-M. Carazo (2009). "Averaging of electron subtomograms and random conical tilt reconstructions through likelihood optimization." Structure **17**(12): 1563-1572.
- Scherrer, K., H. Latham and J. E. Darnell (1963). "Demonstration of an unstable RNA and of a precursor to ribosomal RNA in HeLa cells." Proc Natl Acad Sci U S A **49**(2): 240-248.
- Schilders, G., E. van Dijk and G. J. Pruijn (2007). "C1D and hMtr4p associate with the human exosome subunit PM/Scf100 and are involved in pre-rRNA processing." Nucleic Acids Res **35**(8): 2564-2572.
- Schmidt, C., E. Kowalinski, V. Shanmuganathan, Q. Defenouillère, K. Braunger, A. Heuer, M. Pech, A. Namane, O. Berninghausen, M. Fromont-Racine, A. Jacquier, E. Conti, T. Becker and R. Beckmann (2016). "The cryo-EM structure of a ribosome-Ski2-Ski3-Ski8 helicase complex." Science **354**(6318): 1431-1433.
- Schuch, B., M. Feigenbutz, D. L. Makino, S. Falk, C. Basquin, P. Mitchell and E. Conti (2014). "The exosome-binding factors Rrp6 and Rrp47 form a composite surface for recruiting the Mtr4 helicase." Embo j **33**(23): 2829-2846.
- Schuller, J. M., S. Falk, L. Fromm, E. Hurt and E. Conti (2018). "Structure of the nuclear exosome captured on a maturing preribosome." Science **360**(6385): 219-222.
- Shannon, C. E. (1949). "Communication in the presence of noise." Proceedings of the IRE **37**(1): 10-21.
- Shaw, P. J. and E. G. Jordan (1995). "The nucleolus." Annu Rev Cell Dev Biol **11**: 93-121.
- Shoemaker, C. J., D. E. Eyler and R. Green (2010). "Dom34:Hbs1 promotes subunit dissociation and peptidyl-tRNA drop-off to initiate no-go decay." Science **330**(6002): 369-372.
- Shore, D., S. Zencir and B. Albert (2021). "Transcriptional control of ribosome biogenesis in yeast: links to growth and stress signals." Biochem Soc Trans **49**(4): 1589-1599.
- Singh, P., U. Saha, S. Paira and B. Das (2018). "Nuclear mRNA Surveillance Mechanisms: Function and Links to Human Disease." J Mol Biol **430**(14): 1993-2013.
- Slavov, N., S. Semrau, E. Airoidi, B. Budnik and A. van Oudenaarden (2015). "Differential Stoichiometry among Core Ribosomal Proteins." Cell Rep **13**(5): 865-873.
- Stevens, A. and M. K. Maupin (1987). "A 5'----3' exoribonuclease of *Saccharomyces cerevisiae*: size and novel substrate specificity." Arch Biochem Biophys **252**(2): 339-347.
- Stirnemann, C. U., E. Petsalaki, R. B. Russell and C. W. Müller (2010). "WD40 proteins propel cellular networks." Trends Biochem Sci **35**(10): 565-574.
- Studer, D., B. M. Humbel and M. Chiquet (2008). "Electron microscopy of high pressure frozen samples: bridging the gap between cellular ultrastructure and atomic resolution." Histochem Cell Biol **130**(5): 877-889.

- Su, Y. W., Y. Zhang, J. Schweikert, G. A. Koretzky, M. Reth and J. Wienands (1999). "Interaction of SLP adaptors with the SH2 domain of Tec family kinases." Eur J Immunol **29**(11): 3702-3711.
- Synowsky, S. A. and A. J. Heck (2008). "The yeast Ski complex is a hetero-tetramer." Protein Sci **17**(1): 119-125.
- Tacke, S., P. Erdmann, Z. Wang, S. Klumpe, M. Grange, J. Plitzko and S. Raunser (2021). "A streamlined workflow for automated cryo focused ion beam milling." J Struct Biol **213**(3): 107743.
- Thiry, M. and D. L. Lafontaine (2005). "Birth of a nucleolus: the evolution of nucleolar compartments." Trends Cell Biol **15**(4): 194-199.
- Toh, E. A., P. Guerry and R. B. Wickner (1978). "Chromosomal superkiller mutants of *Saccharomyces cerevisiae*." J Bacteriol **136**(3): 1002-1007.
- Toh, E. A. and R. B. Wickner (1980). "'Superkiller' mutations suppress chromosomal mutations affecting double-stranded RNA killer plasmid replication in *saccharomyces cerevisiae*." Proc Natl Acad Sci U S A **77**(1): 527-530.
- Treanor, B. (2012). "B-cell receptor: from resting state to activate." Immunology **136**(1): 21-27.
- Trumtel, S., I. Léger-Silvestre, P. E. Gleizes, F. Teulières and N. Gas (2000). "Assembly and functional organization of the nucleolus: ultrastructural analysis of *Saccharomyces cerevisiae* mutants." Mol Biol Cell **11**(6): 2175-2189.
- Turin, G. (1960). "An introduction to matched filters." IRE transactions on Information theory **6**(3): 311-329.
- Turk, M. and W. Baumeister (2020). "The promise and the challenges of cryo-electron tomography." FEBS Lett **594**(20): 3243-3261.
- Turoňová, B., L. Marsalek, T. Davidovič and P. Slusallek (2015). "Progressive Stochastic Reconstruction Technique (PSRT) for cryo electron tomography." J Struct Biol **189**(3): 195-206.
- Turowski, T. W. and D. Tollervey (2015). "Cotranscriptional events in eukaryotic ribosome synthesis." Wiley Interdiscip Rev RNA **6**(1): 129-139.
- van Heel, M., B. Gowen, R. Matadeen, E. V. Orlova, R. Finn, T. Pape, D. Cohen, H. Stark, R. Schmidt, M. Schatz and A. Patwardhan (2000). "Single-particle electron cryo-microscopy: towards atomic resolution." Q Rev Biophys **33**(4): 307-369.
- van Hoof, A., P. A. Frischmeyer, H. C. Dietz and R. Parker (2002). "Exosome-mediated recognition and degradation of mRNAs lacking a termination codon." Science **295**(5563): 2262-2264.
- van Hoof, A., R. R. Staples, R. E. Baker and R. Parker (2000). "Function of the ski4p (Csl4p) and Ski7p proteins in 3'-to-5' degradation of mRNA." Mol Cell Biol **20**(21): 8230-8243.
- van Hoof, A. and E. J. Wagner (2011). "A brief survey of mRNA surveillance." Trends Biochem Sci **36**(11): 585-592.
- Vasiljeva, L., M. Kim, H. Mutschler, S. Buratowski and A. Meinhart (2008). "The Nrd1-Nab3-Sen1 termination complex interacts with the Ser5-phosphorylated RNA polymerase II C-terminal domain." Nat Struct Mol Biol **15**(8): 795-804.

- Vasudevan, S., S. W. Peltz and C. J. Wilusz (2002). "Non-stop decay--a new mRNA surveillance pathway." Bioessays **24**(9): 785-788.
- Verheggen, C., J. Mouaikel, M. Thiry, J. M. Blanchard, D. Tollervey, R. Bordonné, D. L. Lafontaine and E. Bertrand (2001). "Box C/D small nucleolar RNA trafficking involves small nucleolar RNP proteins, nucleolar factors and a novel nuclear domain." Embo j **20**(19): 5480-5490.
- Wan, W. and J. A. Briggs (2016). "Cryo-electron tomography and subtomogram averaging." Methods in enzymology **579**: 329-367.
- Wang, L., M. S. Lewis and A. W. Johnson (2005). "Domain interactions within the Ski2/3/8 complex and between the Ski complex and Ski7p." Rna **11**(8): 1291-1302.
- Warner, J. R. and R. Soeiro (1967). "Nascent ribosomes from HeLa cells." Proc Natl Acad Sci U S A **58**(5): 1984-1990.
- Wasmuth, E. V., K. Januszyk and C. D. Lima (2014). "Structure of an Rrp6-RNA exosome complex bound to poly(A) RNA." Nature **511**(7510): 435-439.
- Wienands, J., J. Schweikert, B. Wollscheid, H. Jumaa, P. J. Nielsen and M. Reth (1998). "SLP-65: a new signaling component in B lymphocytes which requires expression of the antigen receptor for phosphorylation." J Exp Med **188**(4): 791-795.
- Wilson, W. A., P. J. Roach, M. Montero, E. Baroja-Fernández, F. J. Muñoz, G. Eydallin, A. M. Viale and J. Pozueta-Romero (2010). "Regulation of glycogen metabolism in yeast and bacteria." FEMS Microbiol Rev **34**(6): 952-985.
- Winding, P. and M. W. Berchtold (2001). "The chicken B cell line DT40: a novel tool for gene disruption experiments." J Immunol Methods **249**(1-2): 1-16.
- Wong, L. E., J. Maier, J. Wienands, S. Becker and C. Griesinger (2018). "Sensitivity-Enhanced Four-Dimensional Amide-Amide Correlation NMR Experiments for Sequential Assignment of Proline-Rich Disordered Proteins." J Am Chem Soc **140**(10): 3518-3522.
- Woolford, J. L., Jr. and S. J. Baserga (2013). "Ribosome biogenesis in the yeast *Saccharomyces cerevisiae*." Genetics **195**(3): 643-681.
- Wu, S., B. Tutuncuoglu, K. Yan, H. Brown, Y. Zhang, D. Tan, M. Gamalinda, Y. Yuan, Z. Li, J. Jakovljevic, C. Ma, J. Lei, M. Q. Dong, J. L. Woolford, Jr. and N. Gao (2016). "Diverse roles of assembly factors revealed by structures of late nuclear pre-60S ribosomes." Nature **534**(7605): 133-137.
- Yu, Z. and A. S. Frangakis (2011). "Classification of electron sub-tomograms with neural networks and its application to template-matching." Journal of structural biology **174**(3): 494-504.
- Yu, Z. and A. S. Frangakis (2014). "M-free: Scoring the reference bias in sub-tomogram averaging and template matching." Journal of structural biology **187**(1): 10-19.
- Zhang, E., V. Khanna, E. Dacheux, A. Namane, A. Doyen, M. Gomard, B. Turcotte, A. Jacquier and M. Fromont-Racine (2019). "A specialised SKI complex assists the cytoplasmic RNA exosome in the absence of direct association with ribosomes." Embo j **38**(14): e100640.
- Zhang, J., X. Zheng, X. Yang and K. Liao (2009). "CIN85 associates with endosomal membrane and binds phosphatidic acid." Cell Res **19**(6): 733-746.

Zinoviev, A., R. K. Ayupov, I. S. Abaeva, C. U. T. Hellen and T. V. Pestova (2020). "Extraction of mRNA from Stalled Ribosomes by the Ski Complex." Mol Cell **77**(6): 1340-1349.e1346.